Universidade do Porto

Doctoral Thesis

Computational Generation and Homogenization of Random Close Packed Materials

Author:
H. David Miranda

Supervisor:
Fancisco A. Pires
Antonio T. Marques

A thesis submitted in fulfilment of the requirements
for the degree of Mechanical Engineering

at the

Department of Mechanical Engineering, Faculty of Engineering
University of Porto

December 2015

"All the variety, all the charm, all the beauty of life is made up of light and shadow."

Leo Tolstoy

Abstract

The increasing use of special tailored materials by the industry, such as the reinforced composites with stiff and strong phase inclusions of very diverse sources, continuously motivates the development and improvement of constitutive models with a design purpose by the scientific community. Furthermore, some natural materials such as bones and other biological tissues are known to exhibit important variations in their microstructures. Many of those materials, natural or tailored composites, share in common a micro-structure geometrically defined by a 'close random packed' distribution of circular or spherical inclusions (or voids) that is known to be very important to their constitutive behavior. The goals of this work are the development of tools for the generation of those material's models and the homogenization of their properties. Additionally, the stochastic nature of the overall homogenized properties is investigated, regarding their random micro-structure.

In order to attain such goal, this thesis starts with a general review on *Continuum Mechanics* and *Finite Elements Method* in Chapter 2. This allows introducing a review of the fundamental theory on *Computational Homogenization of First Order* in Chapter 3. In Chapter 4, it is described a flexible computational code that can be used for the mechanical description of two and three dimensional *Representative Volume Elements* (RVEs) discretized with a relatively large and non-periodic mesh. Chapter 5, presents a new algorithm for the generation of random packed RVEs based on an innovative geometrical concept: the so called *Free Volume*. The developed concept enables efficient generation of statistically random models that are not 'protocol dependent'. In Chapter 6, the homogenization framework was used within commercial software to obtain elastic effective properties in RVEs composed by random disk inclusions. In this context, the elastic properties were evaluated for a large set of random generated RVEs. Then, employing a hypothesis test, the following assumption was determined as being highly improbable: "the stochastic variable associated with the elasticity modulus follows a Gaussian distribution". It was confirmed that the empirical parameter of the *Halpin-Tsai* model, used to obtain homogenized properties, is determined by the geometry of the RVE. Furthermore, this parameter can be determined using computational homogenization.

Chapter 7, addresses the possibility of describing the constitutive behavior of an RVE subjected to internal damage process. A fair capability to qualitatively reproduce the internal damage patterns of the RVE was found. However, it was found a certain tendency for the damage to localize in the borders of the RVE when the size increases. Finally, in Chapter 8, a synthetizes of conclusions and final remarks are provided.

Resumo

A crescente aplicação de materiais avançados e adaptáveis a finalidades específicas pela indústria, como os compósitos reforçados por fases de inclusões rígidas e resistentes de origens muito diversas, motiva continuamente a comunidade científica a desenvolver e melhorar os modelos constitutivos dos materiais para o seu correcto dimensionamento e projecto. Além disso, alguns materiais naturais como os ossos e outros tecidos biológicos são conhecidos por exibir importantes variações ao nível da microestrutura. Muitos desses materiais, naturais ou compósitos desenvolvidos para uma determinada finalidade, partilham em comum uma microestrutura geometricamente definida pela distribuição 'compacta e aleatória' de inclusões (ou vazios) circulares ou esféricas, que se reconhece ser muito importante para o seu comportamento constitutivo. O objectivo deste trabalho prendem-se com o desenvolvimento de ferramentas, para a geração eficaz de modelos para estes materiais e a respectiva homogeneização das suas propriedades mecânicas. Adicionalmente, a natureza estocástica das propriedades globais homogeneizadas é investigada tendo em conta a sua microestrutura aleatória.

De maneira a atingir os objectivos gerais, a tese começa por efectuar uma revisão geral da *Mecânica dos Meios Contínuos* e do *Método dos Elementos Finitos* no Capítulo 2. Este capítulo permite por sua vez, introduzir uma revisão dos fundamentos teóricos para *Homogeneização Computacional de Primeira Ordem* no Capítulo 3. No Capítulo 4, é descrito um código computacional flexível para caracterizar o funcionamento mecânico de *Elementos Representativos de Volume* (ERVs) em duas e três dimensões, descretizados por malhas não periódicas e relativamente grandes. O Capítulo 5, apresenta um novo algoritmo para a geração de ERVs aleatórios e compactos, que se baseia num conceito geométrico inovador designado por: *Free Volume* (Volume Livre). O conceito desenvolvido permite gerar eficientemente modelos estatisticamente aleatórios independentes do 'protocolo de geração' em si mesmo. No Capítulo 6, combinou-se a estrutura de trabalho para homogeneização como a utilização de software comercial, para obter propriedades elásticas efectivas em ERVs compostos por inclusões circulares aleatoriamente distribuídas. Nesse contexto, as propriedades elásticas foram calculadas para um conjunto alargado de ERVs gerados aleatoriamente. Seguidamente, empregando um teste de hipóteses, determinou-se como sendo extremamente improvável a seguinte hipótese: "a variável aleatória associada ao módulo de elasticidade segue uma distribuição Gaussiana". Foi também confirmado, que o parâmetro empírico do modelo *Halpin-Tsai*, utilizado para obter propriedades homogeneizadas, é determinado pela geometria do ERV. Além disso, verificou-se que este parâmetro pode ser determinado utilizando homogeneização computacional. O Capítulo 7, debruça-se sobre a possibilidade de descrever o comportamento constitutivo de um ERV sujeito a processos internos de dano.

Tendo-se obtido uma capacidade aceitável para reproduzir os padrões de dano interno do EVR. Contudo, verificou-se uma certa tendência para a localização do dano nos bordos quando o tamanho do EVR aumenta. Finalmente, no Capítulo 8, apresenta-se uma síntese de conclusões e considerações finais.

Contents

List of Figures

List of Tables

List of Symbols

Chapter 2

$\mathbf{B}$	Left Cauchy-Green deformation tensor
$\mathbf{b}$	Body force per unit of volume acting in a point in the deformed configuration
$\mathbf{C}$	Right Cauchy-Green deformation tensor
$\mathbf{E}$	Lagrangian of Green strain tensor
$\mathbf{e}$	Eulerian or Almansi strain tensor
$\mathbf{e_1}, \mathbf{e_2}, \mathbf{e_3}$	Unitary vectors indicating the directions of a Cartesian reference system
$\mathbf{F}$	Deformation gradient
$\mathbf{F}_{iso}$	Isochoric component of the deformation gradient
$\mathbf{F}_v$	Volumetric component of the deformation gradient
J	Jacobian of the transformation of coordinates $\boldsymbol{\phi}$
N_I	Shape function associated to a node I
$\mathbf{n}$	Vector normal to a surface
$\mathbf{P}$	First Piolla-Kirchhoff stress tensor
$\mathbf{r}$	Residual force per unit of volume
$\mathbf{T}$	Traction vector in the reference configuration
$\mathbf{t}$	Traction vector in the deformed configuration
t	Time
u	Displacement
$\mathbf{X}$	Coordinates of a generic point in the reference configuration
$\mathbf{x}$	Coordinates of a generic point in the deformed configuration
δw	Virtual work
$\boldsymbol{\mathcal{E}}$	Third-order alternating tensor
$\boldsymbol{\eta}$	Virtual velocity vector
$\boldsymbol{\xi}$	Coordinates of a generic point in the local coordinate system of a finite element
ρ	Material density in the deformed configuration
ρ_0	Material density in the reference configuration
$\boldsymbol{\sigma}$	Cauchy stress tensor
σ_{ij}	Component i,j of the Cauchy stress tensor
$\boldsymbol{\phi}$	Transformation of coordinates from the reference to the deformed configuration

Chapter 3

$\mathbb{A}$	Material tangent modulus
$\bar{\mathbf{B}}$	Macro scale body forces per unit of volume
$\mathbf{B}_\mu$	Micro scale body forces per unit of volume
$\bar{\mathbf{F}}$	Macro scale deformation gradient
$\mathbf{F}_\mu$	Micro scale deformation gradient
$\mathbf{G}^g$	Discrete material gradient operator
$\mathbf{K}$	Global stiffness matrix
$\mathbf{N}$	Micro scale vector normal to the boundary
$\bar{\mathbf{P}}$	Macro scale first Piolla-Kirchhof stress tensor
$\mathbf{P}_\mu$	Micro scale first Piolla-Kirchhof stress tensor
$\mathbf{T}_\mu$	Micro scale traction per unit reference area
$\tilde{\mathbf{u}}$	Micro scale displacement fluctuations
V_μ	RVE volume
$\mathbf{X}$	Coordinates of a point in the macro scale
$\mathbf{Y}$	Coordinates of a point in the micro scale
$\delta\tilde{\mathbf{u}}$	Vector with the discretized fluctuations of displacements
$\boldsymbol{\eta}$	Virtual displacement field

Chapter 4

$\mathbf{A}$	General matrix with the coefficients of an algebraic equation system
a_{ij}	Interpolation coefficient
E	Elasticity modulus
$\mathbf{F}$	Deformation gradient
$\mathbf{K}$	Key value to identify an entry of an hash table
N_I	Shape function associated to a node I
$\mathbf{P}$	First Piolla-Kirchhoff stress tensor
u_i	Degree of freedom of the the node i
$\mathbf{V}$	Sparse storage vector
$\bar{\mathbf{V}}$	Compact storage vector
v_i	Degree of freedom of the virtual node i
ν	Poison ratio
$\boldsymbol{\xi}$	Coordinates of a generic point in the local coordinate system of a finite element
σ_{y0}	Yielding stress
ψ	Hash function

Chapter 5

$\mathbb{A}$	Admissible region
a	Edge length of an RVE
$\mathbf{C}$	Constitutive matrix
$\mathbb{D}$	Domain where the inclusions intend to be distributed
d_i	Subdomain of the RVE obtained after decomposition
F_v	Free volume
f	Free volume function
G	Shear modulus
g	Transformation function of the free volume variable
$i_1, i_2, i_3, ...$	Array of index used to denote the successive domain decompositions
k	Number of order associated to a decomposition of the RVE domain
R	Inclusion radius
V_{av}	Free volume
W_f	Free volume modified
μ	Mean value
ρ_A	Coefficient of variation of the areas
ρ_D	Coefficient of variation of the distances
σ	Stress tensor or Standard deviation
ϕ_c	Volume fraction of an RVE

Chapter 6

E	Elasticity modulus
G	Shear modulus
X,Y	Random variables
ν	Poison ratio
ξ	Reinforcement parameter of the Halpin-Tsai model

Chapter 7

$\mathbf{C}$	Consistent tangent operator
$\mathbf{D}$	Damage tensor
D	Scalar damage parameter
f_t	Tensile strength
G_f	Fracture energy
K	Undamaged stiffness of the cohesive model
K_n	Undamaged stiffness in the normal direction
K_t	Undamaged stiffness in the tangential
l^e	Characteristic element length
S	Tangential component of the traction force
$\mathbf{Y}$	Energy release rate
$\boldsymbol{\alpha}$	State variables
δ	Separation distance
δ_n	Normal component of the separation vector
δ_s	Tangential component of the separation vector
$\bar{\delta}$	Effective displacement
$\bar{\delta}^{\max}$	Maximum effective displacement
$\bar{\delta}^0$	Minimum displacement for damage initiation
$\bar{\delta}^f$	Maximum displacement for complete material failure
$\boldsymbol{\varepsilon}$	Strain tensor
ε_f	Failure strain
ε_{f2}	Regularization parameter
$\tilde{\varepsilon}$	Equivalent strain
κ	Maximum equivalent strain
κ_0	Initial damage threshold
λ	Material parameter corresponding to the length of the damage zone
$\boldsymbol{\sigma}$	Cauchy stress tensor
$\boldsymbol{\sigma}_0$	Effective stress tensor
$\boldsymbol{\sigma}^p$	Tensor containing the principal components of the effective stress
$\boldsymbol{\Phi}$	Damage threshold surface
Ψ	Free energy function or specific fracture energy

List of Abbreviations

ABAQUS	Commercial FEM Software
B.C.	Boundary Condition
CDM	Continuum Damage Mechanics
CG	Conjugate Gradient
CRM	Collective rearrangement models
DEM	Discrete Element Method
FEM	Finite Element Method
FRC	Fibre Reinforced Composite
FREE_V	Free Volume Method
GMRES	Generalized Minimal Residual Method
ITZ	Interface Transition Zone
MATLAB	Commercial Software for Numerical Computing
MCM	Monte Carlo Method
PCG	Pre-conditionated Conjugate Gradient
PDF	Probability Distribution Function
RAND_uSTRU_GEN	Random Micro Structure Generation Method
RSA	Random sequential addition
RVE	Representative Volume Element
SOR	Successive Over-relaxation
VWP	Virtual Work Principle
2D	2-Dimensional
3D	3-Dimensional

À memória do meu Avô

Chapter 1

Introduction

A large amount of scientific fields rely on the study of physical bodies and their constitutive behavior when subjected to loads. In special, the development, exploration and optimization of engineering structures and materials, depend on the existent material constitutive theories.

In the literature, two main groups of approaches were followed in order to develop the constitutive models: the phenomenological and the micro mechanical. The phenomenological approach, is related with the characterization of the material in terms of its mechanical response, considering for this an homogeneous and continuous scale. While the micromechanical approach, consists in the determination of continuum counterparts from the micromechanical description.

The phenomenological, approach allowed the development of relatively accurate models for some classes of materials. However, the attempts of using this type of strategy with brittle, fragile materials and others, did not prove to be as successful.

Besides, the development of reinforced composites with stiff and strong phase inclusions of glass, graphite, boron or aluminum oxide combined with epoxy resin, steel, titanium or aluminum(Figure 1.1), in a wide range of possibilities to enhance strength, thermal expansion and wear resistance, demands a different approach. Specifically, a more flexible way that allows accessing the macroscopic properties directly based in the knowledge of their microscopic structure. This relation can be used as a design tool, since it allows the optimization of the materials characteristics regarding specific applications. Therefore, experiential campaigns aimed to determine material properties of a large amount of samples can be shortened or even avoided, with consequent economic and project duration benefits.

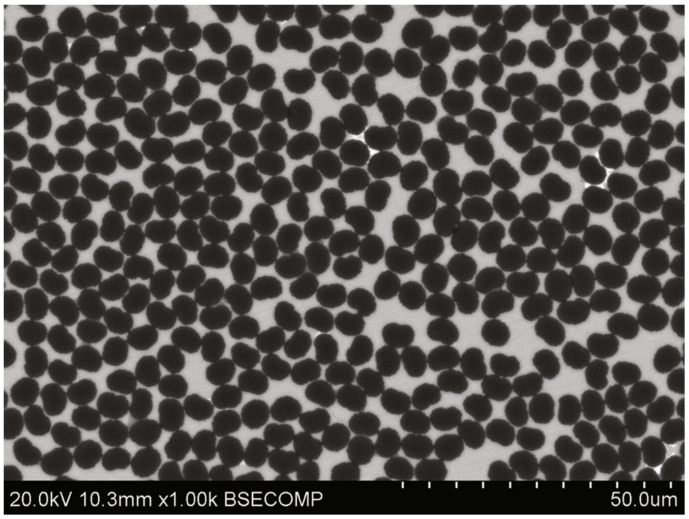

FIGURE 1.1: Microstructure of a carbon fiber reinforced aluminum composite[2].

Furthermore, the access to overall macroscopic properties of heterogeneous distributions of materials is a very important issue for engineering and scientific applications. In fact, the heterogeneity determines the mechanical behavior of a large variety of materials, such as: polymers, ceramics (Figure 1.3), and composites(Figure 1.1), alloys containing pores, bones(Figure 1.2) and biological material(Figure 1.4).

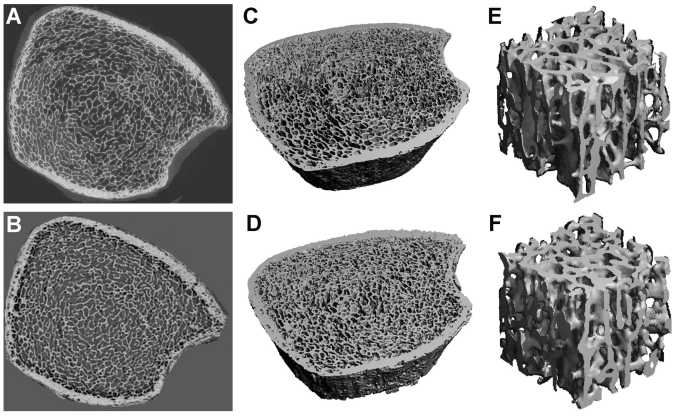

FIGURE 1.2: Microstructure from human tibia bone[1].

The predictive capability of the micromechanical approach relies on two key factors: the homogenization strategy and the description of the microstructure with appropriate definition of different phases. One of the commonly employed strategies to obtain microstructural descriptions is the post-processing of laboratorial images. This strategy provides realistic geometries for the models, however requires the existence of the material itself and in some cases is difficult implement in the practice. Therefore, computational generation of the micro-structures can be an alternative. Another important aspect regarding the micromechanical description is that a large amount of materials are composed by inclusions or cavities distributed in a compact manner in the bulk

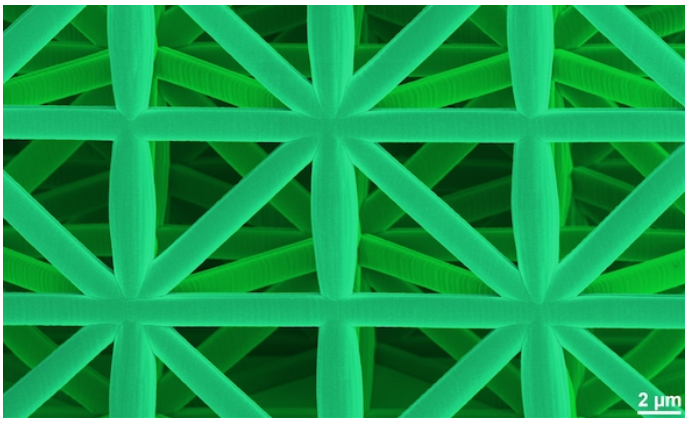

FIGURE 1.3: Nanoscale micro-truss structures built using 3 dimentional laser lithography[3].

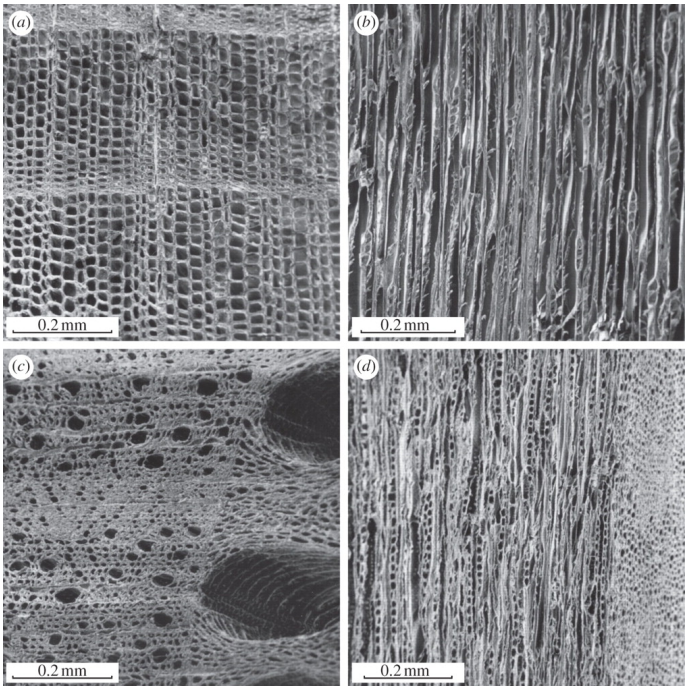

FIGURE 1.4: Microstructure of woods (scanning electron micrographs)[4].

material. The geometrical description of those models can be interpreted as a "random close packing".

1.1 Homogenization

The consideration of different scales for constitutive modeling of solids, has reached more and more importance over recent years. This importance is motivated by the expectation of obtaining accurate models for special applications. Those applications, may involve complex deformation paths, which most of the classical phenomenological non-elastic models have difficulties to address. Furthermore, the comprehension of how the internal

structure affects the overall mechanical properties, allows the design of specific tailored materials.

Analytic homogenization

The first attempts to model the behavior of composites and tailored materials were analytical. A very simple analytic procedure to obtain overall properties is known as *rule of mixtures*. The *rule of mixtures* is an weighted average, involving mechanical properties(e.g. Elastic Modulus, Poison's ratio) and amounts(e.g. volume, mass) of the material constituent phases. This approach however, completely disregards the geometrical distribution of the constituents in the microstructure. An idea known as *Effective Medium Approach* was suggested by Eshelby [5] in 1957, in order to obtain overall properties in materials with microstructure defined by a repetitive pattern. Based on that idea, Hill in 1965, proposes the concept of *self-consistence approach* [6]. In spite of these concepts providing reasonable results, the materials that can be addressed with that strategy are very simple.

The *mathematical asymptotic homogenization theory* is described by Bensoussan [7] and Sanchez-Palencia [8]. This approach is developed under the mathematical asymptotic expansion of the displacement and stress fields.

A detailed review on the advances of the analytical periodical homogenization can be found in Markov [9] and Böohm [10].

Computational homogenization

The computational homogenization relies on the concept of Representative Volume Element (RVE). The RVE is defined to be sufficiently large compared with the microstructural size in order to describe it statistically; and simultaneously, small enough so that the hypothesis of homogeneity remains valid at the structural level. Then a numerical RVE model with appropriate boundary conditions is used to compute the relation stress-strain. This approach can address general geometries and non-linear problems. Some of the many works that develop this formulation are [11] and [12]. Despite the homogenization contributed to enhancement of the models for heterogeneous materials, important differences between those models and the empirical evidence persist, especially out of the linear domain.

1.2 Close Random Packing

Studies [13] [14] conclude than an important factor for accurate determination of the constitutive response is the use of geometrically accurate RVE. Therefore, oversimplifications can introduce inaccurate representation of phenomena, important to the overall response. On the other hand, a wide set of materials micro-structure, can be described by a compact array of inclusions or cavities within a matrix. For instance: unidirectional fiber reinforced composites, bones, and soils, concrete and other grain materials fall into this category. Because of this reason, RVE models based on a compact random distribution of particles are very common in the literature, where they are also mentioned as *Random Close Packing*(RCP).

Nevertheless, many other applications exist for RCP, ranging from fruit packing, adsorption on surfaces and other statistical mechanics problems. This wide range of RCP applications motivated many different studies. Some authors [15] argue that, the RCP condition is "ill-defined" and requires clarification. The reason that demands clarification of RCP concept, is the tradeoff between "random" and "close packing", since "organization" leads to a better packing. Consequently, the packing state of the models tends to be "protocol dependent".

1.3 Objectives

Therefore, the objective of this thesis is to focus the attention on the development of tools for generation and homogenization of materials described by random close packed inclusions. This objective encompasses a varied array of issues that range: from the developments on the homogenization algorithms, the generation of RVEs, the statistical characterization of RVEs and the homogenized properties themselves, the establishment of relations with existent analytic models and, lastly, the study of internal damage process.

1.4 Outline

This thesis was structured so that each chapter describes a different topic.

In Chapter 2, a brief description of the fundamental principles on continuum mechanics and finite elements method is presented.

This provides a basis for the subject introduced in Chapter 3, where the methods for analytical and computational homogenization are introduced. Those principles are then

used in a computational code for the homogenization of three-dimensional representative volume elements (RVE). The algorithm used for the computational implementation is described in the end of Chapter 3.

In the following Chapter 4, an improved version of the algorithm described in Chapter 3, is described. This improved version is obtained by a combination of computational and numerical strategies for the prescription of boundary conditions in arbitrary meshes and the handling of problems with a large amount of degrees of freedom.

In Chapter 5, an algorithm for RVEs of random packed disk inclusions, based on sequential addition, is proposed. The algorithm presents a new geometric concept used to introduce inclusions without conflicting with existing ones and obtain, at same time perfectly random RVEs that are not 'protocol dependent'. Then, the representativeness is verified with statistical methodologies. In the end of the chapter a modification to the algorithm that reduces the 'randomness' in order to generate RVEs with higher fraction of inclusions is described.

Chapter 6, describes a set of numerical experiments to access the relations between the microstructure of the materials and its macroscopic elastic properties. Firstly, the general framework, to generate RVE and access to their overall properties is described and validated against analytical models existing in the literature. Then, a statistical characterization of the overall elastic properties, considering a large amount of RVEs, is conducted. The influence of the relations between stiffness of the phases in the homogenized properties is explored, and comparisons with the semi-empirical Halpin-Tsai model are conducted. Furthermore, the effect of a thin interface layer between inclusions and the matrix material is investigated. Comparisons of results between three dimensional RVE models with spherical inclusions and two dimensional models with disk inclusions are described in the end of the chapter.

Chapter 7, address the study of the internal damage in random packed materials, using the homogenization framework described in the previous chapters. However, common damage models and cohesive models are employed to describe the degradation of the phases. This allows accessing to to the damage patterns, and stress-strain curves under different strain conditions. Finally, some remarks on the problems and limitations of the methodology employed are pointed out.

In Chapter 8, a synthesis of conclusions, remarks and suggestions for future works is provided.

Chapter 2

Continuum Mechanics and Finite Element Method

This chapter briefly presents the basic principles and fundamentals of continuum mechanics and the finite element method which are important in the development of this work. However, there is no intention of being exhaustive and for a more detailed description refer for example to [16] and [17].

2.1 Kinematics of deformation

2.1.1 The motion

Figure 2.1 shows the motion of a generic deformable body.

At the initial time, $t = 0$, each particle of the body occupies a position defined by the coordinates $\mathbf{X}$. The same particle after the deformation at the time $t \geq 0$, occupies the position $\mathbf{x}$. This motion can be described by a function $\boldsymbol{\phi}$ as follows.

$$\mathbf{x} = \boldsymbol{\phi}(\mathbf{X}, t) \tag{2.1}$$

2.1.2 Material and spatial descriptions

There are many quantities that depend on the deformation of the body, such as length, area, volume and density. The quantities at the initial time $t = 0$ are called the *material* or *Lagrangian* quantities. The quantities at a latter time than initial $t > 0$ are called

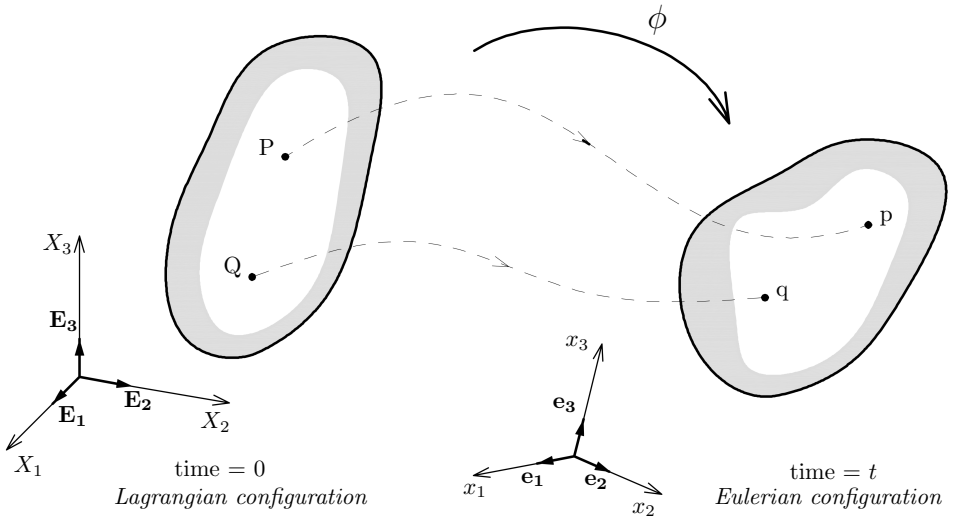

FIGURE 2.1: General motion of a deformable body.

spatial or *Eulerian* quantities. A material description refers to the behavior of a material particle, whereas a spatial description refers to the behavior at a spatial position[16].

Consider as example a scalar quantity as the material density ρ:

- *Material description*: the value of ρ is defined as a function of the position in the initial coordinates $\mathbf{X}$ at the time $t = 0$ as follows.

$$\rho_0 = \rho_0(\mathbf{X}). \tag{2.2}$$

- *Spatial description*: the value of ρ is defined as a function of the position $\mathbf{x}$ that the particle occupies in the space at a given time t.

$$\rho = \rho(\mathbf{x}, t). \tag{2.3}$$

2.1.3 Deformation gradient

The *deformation gradient* $\mathbf{F}$ is a very important quantity involved in many equations and relates the transformation of coordinates before and after the deformation. The *deformation gradient tensor* $\mathbf{F}$ is defined as follows.

$$\mathbf{F} = \frac{\partial \boldsymbol{\phi}}{\partial \mathbf{X}} = \nabla \boldsymbol{\phi}. \tag{2.4}$$

2.1.4 Strain

There are some relations established from the definition of the deformation gradient in the material and spatial configuration:

- *right Cauchy-Green deformation tensor*

$$\mathbf{C} = \mathbf{F}^T\mathbf{F} \tag{2.5}$$

- *left Cauchy-Green or Finger tensor*

$$\mathbf{B} = \mathbf{F}\mathbf{F}^T \tag{2.6}$$

The following tensors can be used to define strain measures in the material and spatial configuration:

- *Lagrangian* or *Green strain tensor*

$$\mathbf{E} = \frac{1}{2}(\mathbf{C} - \mathbf{I}) \tag{2.7}$$

- *Eulerian or Almansi strain tensor*

$$\mathbf{e} = \frac{1}{2}(\mathbf{I} - \mathbf{B}^{-1}) \tag{2.8}$$

2.1.5 Volume change

If we consider an infinitesimal volume element in the material configuration, with edges parallel to the Cartesian axes given by the vectors $\mathbf{dX_1}$, $\mathbf{dX_2}$ and $\mathbf{dX_3}$, the material volume dV is then given by:

$$dV = |\mathbf{dX_1}||\mathbf{dX_2}||\mathbf{dX_3}|. \tag{2.9}$$

To obtain the deformed volume, in the spatial configuration dv, it is useful to consider the following expressions:

$$\mathbf{dx_1} = \mathbf{F}\mathbf{dX_1} = \frac{\partial \phi}{\partial X_1} dX_1; \tag{2.10}$$

$$\mathbf{dx_2} = \mathbf{F}\mathbf{dX_2} = \frac{\partial \boldsymbol{\phi}}{\partial X_2} dX_2; \tag{2.11}$$

$$\mathbf{dx_3} = \mathbf{F}\mathbf{dX_3} = \frac{\partial \boldsymbol{\phi}}{\partial X_3} dX_3. \tag{2.12}$$

The triple product of the elementary vectors $\mathbf{dx_1}$, $\mathbf{dx_2}$ and $\mathbf{dx_3}$ is equal to the deformed volume dv, as follows:

$$dv = \mathbf{dx_1} \cdot (\mathbf{dx_2} \times \mathbf{dx_3}) = \frac{\partial \boldsymbol{\phi}}{\partial \mathbf{X_1}} \cdot \left(\frac{\partial \boldsymbol{\phi}}{\partial \mathbf{X_2}} \times \frac{\partial \boldsymbol{\phi}}{\partial \mathbf{X_3}} \right) dX_1 dX_2 dX_3 \tag{2.13}$$

The previous expression can be written as,

$$dv = JdV; \quad J = det\, \mathbf{F}. \tag{2.14}$$

2.1.6 Distortional component of the deformation gradient

The deformation gradient can be decomposed in a distortional component (or *isochoric*) and a pure *volumetric* component, as follows:

$$\mathbf{F} = \mathbf{F}_{iso}\mathbf{F}_v, \tag{2.15}$$

where $\mathbf{F}_{iso}$ is the isochoric component and $\mathbf{F}_v$ is the volumetric component, given by:

$$\mathbf{F}_v = (det\, \mathbf{F})^{\frac{1}{3}}\mathbf{I} \tag{2.16}$$

$$\mathbf{F}_{iso} = (det\, \mathbf{F})^{-\frac{1}{3}}\mathbf{F}. \tag{2.17}$$

This decomposition is very useful for both incompressible and nearly incompressible materials.

2.2 Stress measures

2.2.1 Cauchy stress tensor

Consider a body in the deformed configuration as shown in Figure 2.2.

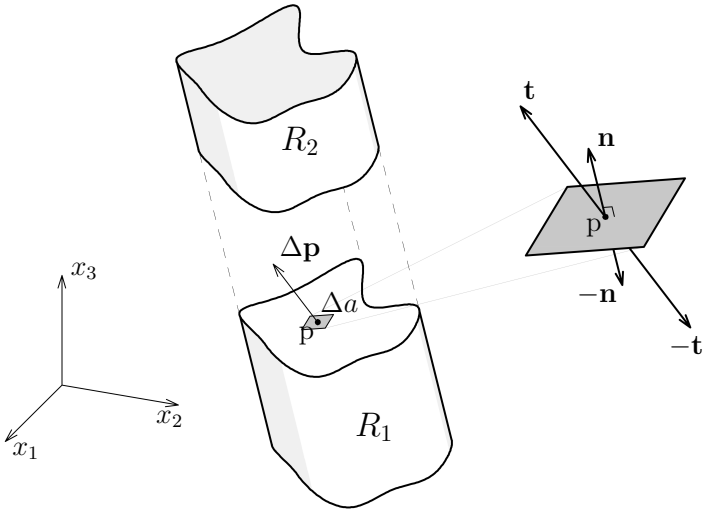

FIGURE 2.2: Traction vector.

Let us consider an element of area Δa with a normal vector $\mathbf{n}$ in the neighborhood of a spatial point $\mathbf{p}$. If the resultant force on this area is $\Delta\mathbf{p}$, then the traction vector $\mathbf{t}$ is defined as follows:

$$\mathbf{t}(\mathbf{n}) = \lim_{\Delta a \to 0} \frac{\Delta \mathbf{p}}{\Delta a}. \tag{2.18}$$

The three components of the traction vector with the Cartesian directions $\mathbf{e_1}$, $\mathbf{e_2}$, $\mathbf{e_3}$ expressed in a component form are given by:

$$\mathbf{t}(\mathbf{e_1}) = \sigma_{11}\mathbf{e_1} + \sigma_{21}\mathbf{e_2} + \sigma_{31}\mathbf{e_3}; \tag{2.19}$$

$$\mathbf{t}(\mathbf{e_2}) = \sigma_{12}\mathbf{e_1} + \sigma_{22}\mathbf{e_2} + \sigma_{32}\mathbf{e_3}; \tag{2.20}$$

$$\mathbf{t}(\mathbf{e_3}) = \sigma_{13}\mathbf{e_1} + \sigma_{23}\mathbf{e_2} + \sigma_{33}\mathbf{e_3}. \tag{2.21}$$

The traction vector for the normal direction $\mathbf{e_2}$ is represented on the Figure 2.3.

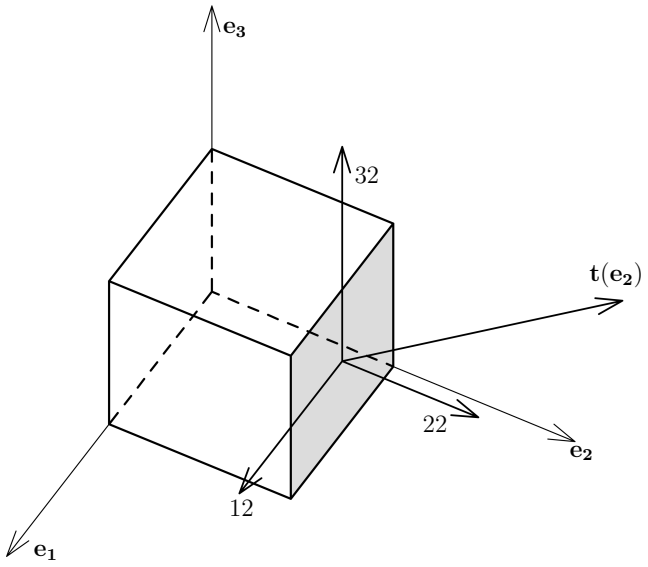

FIGURE 2.3: Stress components.

Consider an infinitesimal tetrahedron around the point $\mathbf{p}$ of the deformed body (represented on the Figure 2.4) and let $\mathbf{b}$ be the body force per unit volume acting on the body around the point $\mathbf{p}$.

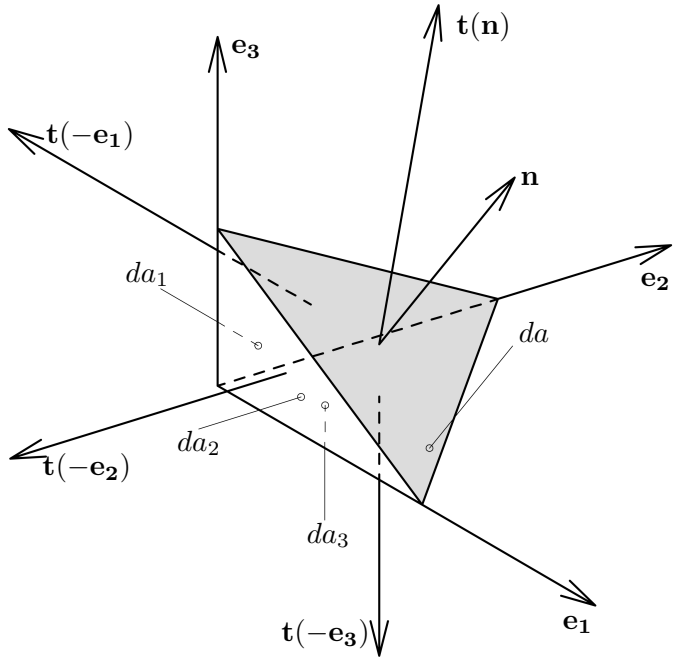

FIGURE 2.4: Elemental tetrahedron.

The equilibrium of the tetrahedron is given by the following condition:

$$\mathbf{t}(\mathbf{n})\, da + \sum_{i=1}^{3} \mathbf{t}(-\mathbf{e_i}) da_i + \mathbf{b}\, dv = \mathbf{0} \tag{2.22}$$

where dv is the volume of the deformed infinitesimal tetrahedron, while da_i and da are the deformed infinitesimal areas of the boundary faces of the tetrahedron. Considering that dv is an infinitesimal quantity of higher order ($dv/da \to 0$), then the body forces become negligible, so that:

$$\mathbf{t}(\mathbf{n}) = \sum_{j=1}^{3} \sigma_{ij} (\mathbf{e_j} \cdot \mathbf{n}) \mathbf{e_i}. \tag{2.23}$$

Since $(\mathbf{e_j} \cdot \mathbf{n})\, \mathbf{e_i}$ can be expressed using the tensorial product $(\mathbf{e_i} \otimes \mathbf{e_j})\, \mathbf{n}$, the previous expression can be rewritten as follows:

$$\mathbf{t}(\mathbf{n}) = \left[\sum_{i,j=1}^{3} \sigma_{ij} (\mathbf{e_i} \otimes \mathbf{e_j}) \right] \mathbf{n}. \tag{2.24}$$

Defining the *Cauchy stress tensor* $\boldsymbol{\sigma}$ such as:

$$\boldsymbol{t}(\boldsymbol{n}) = \boldsymbol{\sigma} \boldsymbol{n} \tag{2.25}$$

then $\boldsymbol{\sigma}$ is defined by:

$$\boldsymbol{\sigma} = \sum_{i,j=1}^{3} \sigma_{ij} (\mathbf{e_i} \otimes \mathbf{e_j}) \tag{2.26}$$

2.2.2 First Piola-Kirchhoff stress tensor

To define the Cauchy stress tensor $\boldsymbol{\sigma}$ deformed (spatial) quantities have been considered. If we wish to refer the stress state to the initial (material) configuration then the First Piolla-Kirchhoff stress $\mathbf{P}$ can be employed. This stress tensor, defined in the initial configuration, can be related with the Cauchy stress, according to the expression (2.27).

$$\mathbf{P} = J\, \boldsymbol{\sigma} \mathbf{F}^{-T} \tag{2.27}$$

2.3 Fundamental principles

2.3.1 Translational equilibrium

The translational equilibrium of a general deformable body defined by a volume v with boundary area ∂v, ignoring inertia forces, on the deformed configuration implies that:

$$\int_{\partial v} \mathbf{t}\, da + \int_{v} \mathbf{b}\, dv = \mathbf{0}. \tag{2.28}$$

The use of equation (2.25) for the traction vector allows the previous equation to be rewritten as follows:

$$\int_{\partial v} \boldsymbol{\sigma}\mathbf{n}\, da + \int_{v} \mathbf{b}\, dv = \mathbf{0}. \tag{2.29}$$

Applying the Gauss theorem to the first term, the expression can be transformed in to:

$$\int_{v} \left(div\, \boldsymbol{\sigma} + \mathbf{b}\right)\, dv = \mathbf{0}. \tag{2.30}$$

Since the above equation must be applicable to any closed volume v of the body, the following condition is enough and necessary to verify the translational equilibrium:

$$div\, \boldsymbol{\sigma} + \mathbf{b} = \mathbf{0}. \tag{2.31}$$

Note that in the expression (2.31) $\boldsymbol{\sigma}$, $\mathbf{b}$ and the divergence operator (div) refer to the deformed (spatial) configuration. This expression can also be written in the initial (material) configuration using the equivalent counterparts, i.e. the First Piola-Kirchhoff stress $\mathbf{P}$, the body forces in the initial configuration $\mathbf{B}$ and the material divergence operator $div_{\mathbf{p}}$, using the expression (2.32).

$$div_{\mathbf{p}}\, \boldsymbol{P} + \mathbf{B} = \mathbf{0} \tag{2.32}$$

2.3.2 Rotational equilibrium

The rotational equilibrium of any deformable body defined by a volume v with boundary area ∂v on the deformed configuration is given by the following condition:

$$\int_{\partial v} \mathbf{x} \times \mathbf{t}\, da + \int_{v} \mathbf{x} \times \mathbf{b}\, dv = \mathbf{0}. \tag{2.33}$$

Using equation (2.25) for the traction vector, enables the above equation to be written as follows:

$$\int_{\partial v} \mathbf{x} \times (\boldsymbol{\sigma}\mathbf{n}) da + \int_{v} \mathbf{x} \times \mathbf{b}\, dv = \mathbf{0}. \tag{2.34}$$

Considering the Gauss theorem and performing some algebraic operations it is possible to obtain the following condition:

$$\int_{v} \mathbf{x} \times (div\, \boldsymbol{\sigma})\, dv + \int_{v} \boldsymbol{\mathcal{E}} : \boldsymbol{\sigma}^T dv + \int_{v} \mathbf{x} \times \mathbf{b}\, dv = \mathbf{0} \tag{2.35}$$

where $\boldsymbol{\mathcal{E}}$ is the third-order alternating tensor ($\mathcal{E}_{ijk} = 1$ if the permutation i, j, k is even, -1 if it is odd, and zero if any indices are repeated)

Rearranging the equation (2.35) and taking into account the translational equilibrium (2.31) results that the following condition must prevail for any enclosed region:

$$\boldsymbol{\mathcal{E}} : \boldsymbol{\sigma}^T = \begin{bmatrix} \sigma_{32} - \sigma_{23} \\ \sigma_{13} - \sigma_{31} \\ \sigma_{21} - \sigma_{12} \end{bmatrix} = \mathbf{0}. \tag{2.36}$$

This last equation implies the symmetry of the Cauchy stress tensor $\boldsymbol{\sigma}$.

2.3.3 Principle of Virtual Work

The out-of-balance or residual force per unit of volume $\mathbf{r}$, obtained from Equation (2.31) when equilibrium is not satisfied, is given by:

$$\mathbf{r} = div\, \boldsymbol{\sigma} + \mathbf{b}. \tag{2.37}$$

The virtual work equation can be expressed by:

$$\delta w = \mathbf{r} \cdot \boldsymbol{\eta} = 0, \tag{2.38}$$

for any arbitrary vector $\boldsymbol{\eta}$. In this equation $\boldsymbol{\eta}$ denotes the virtual velocity vector, while δw denotes the virtual work, done by the residual force $\mathbf{r}$ during a virtual motion per unit volume and time. Introducing equation (2.31) and integrating over a volume v of the deformed body with boundary ∂v, the following expression can be derived:

$$\delta W = \int_v (div\boldsymbol{\sigma} + \mathbf{b}) \cdot \boldsymbol{\eta} dv = 0. \tag{2.39}$$

The above expression (2.39) is known as the *weak statement of the static equilibrium of the body*. However, a more common formulation can be derived. Considering the following mathematical identity:

$$div(\boldsymbol{\sigma}\boldsymbol{\eta}) = (div\boldsymbol{\sigma}) \cdot \boldsymbol{\eta} + \boldsymbol{\sigma} : \nabla\boldsymbol{\eta}, \tag{2.40}$$

and employing the Gauss theorem, the equation (2.39), can be rewritten as follows:

$$\int_{\partial v} \mathbf{n} \cdot \boldsymbol{\sigma}\boldsymbol{\eta}\, da - \int_v \boldsymbol{\sigma} : \nabla\boldsymbol{\eta}\, dv + \int_v \mathbf{b} \cdot \boldsymbol{\eta}\, dv = 0. \tag{2.41}$$

The gradient of $\boldsymbol{\eta}$ is defined as the virtual velocity gradient $\delta\mathbf{l}$. Consequently, it is possible to combine the Equations (2.31) and (2.41) to obtain:

$$\int_v \boldsymbol{\sigma} : \delta\mathbf{l}\, dv = \int_v \mathbf{b} \cdot \boldsymbol{\eta} dv + \int_{\partial v} \mathbf{t} \cdot \boldsymbol{\eta}\, da. \tag{2.42}$$

Furthermore, from (2.42) it is possible to obtain the *spatial virtual work equation* (2.43) considering that:

- the virtual velocity gradient $\delta\mathbf{l}$ can be expressed by the symmetric virtual rate of the deformation $\delta\mathbf{d}$;
- the virtual spin tensor is antisymmetric;
- the tensor $\boldsymbol{\sigma}$ is symmetric.

$$\delta W = \int_v \boldsymbol{\sigma} : \delta\mathbf{d}\, dv - \int_v \mathbf{b} \cdot \boldsymbol{\eta}\, dv - \int_{\partial v} \mathbf{t} \cdot \boldsymbol{\eta}\, da = 0. \tag{2.43}$$

The correspondent material version of the *Virtual Work Principle (VWP)* equation (2.43) is given in expression (2.44).

$$\delta W = \int_V \mathbf{P} : \nabla_{\mathbf{P}} \boldsymbol{\eta} \, dV - \int_V \mathbf{B} \cdot \boldsymbol{\eta} \, dV - \int_{\partial V} \mathbf{T} \cdot \boldsymbol{\eta} \, dA = 0 \tag{2.44}$$

On expression (2.44), V and ∂V represent the initial volume of the body (material configuration) and his boundary respectively, and $\nabla_{\mathbf{P}}$ the gradient operator in the initial configuration. In that expression, all the variables refer to the initial configuration and $\mathbf{P}$, $\mathbf{B}$ and $\mathbf{T}$ represent the stress, body forces and surface traction respectively.

2.4 Finite Element Method

In this section, a general Finite Element Method (FEM) formulation is briefly described. More details about the FEM can be found in [18],[19],[16] and [20]. The FEM is a numerical method to solve systems of differential equations and, in this work, it will be employed for the solution of the equilibrium equations of continuum solid mechanics.

The Finite Element Method is based on two major numerical approximations: a time and a spatial discretization. With the introduction of those approximations, the original initial boundary value problem is reduced to a set of incremental algebraic equations to be solved at each time interval of discretization. The more common numerical scheme used to solve those equations is the Newton-Raphson algorithm.

2.4.1 Time Discretization

Time discretization is provided by a numerical integration scheme which allows the transformation of the original time-continuum constitutive equation problem in an incremental (or time-discrete) problem, according to Figure 2.5.

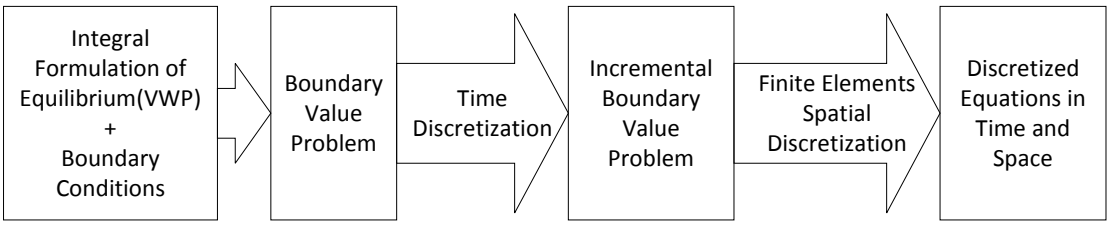

FIGURE 2.5: Numerical approximations the equilibrium boundary value problem.

2.4.2 Spatial Discretization

The spatial discretization of the continuum problem into finite elements allows the division of complex domains into simple standard domains (see Figure 2.6), providing a simple way of performing numerical integration of the field variables.

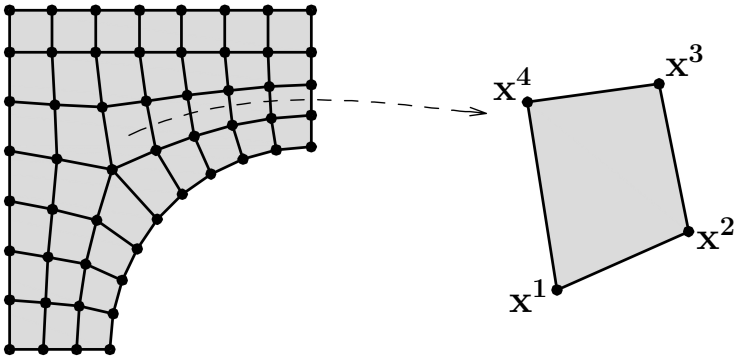

FIGURE 2.6: Discretization of a plane domain with quadrilateral finite elements

The discretization is established in the initial configuration, and the coordinates of the initial geometry are obtained in terms of standard element by interpolation. For that propose, the coordinates in the initial configuration are given by:

$$\mathbf{x}(\boldsymbol{\xi}) = \sum_{I=1}^{n_{node}} N_I(\boldsymbol{\xi})\mathbf{x}^I \tag{2.45}$$

where $\boldsymbol{\xi}$ are the coordinates of a standard element type in the local coordinate system. $N_I(\boldsymbol{\xi})$ is the shape function associated to each node I of the element. The variable $\mathbf{x}^I$ represents the coordinates of node I of the element.

The shape functions N_I are usually polynomial functions that assume the value of one at the node with coordinates of I ($N_I(\boldsymbol{\xi}^I) = 1$) and zero at the coordinates of the other nodes.

The association of coordinates for a standard quadrilateral element is represented in Figure 2.7.

This type of approximation is also used to interpolate any other variable $\mathbf{u}$ for which the values, $\mathbf{u}^I$, at each node I are known.

$$\mathbf{u}(\boldsymbol{\xi}) = \sum_{I=1}^{n_{node}} N_I(\boldsymbol{\xi})\mathbf{u}^I \tag{2.46}$$

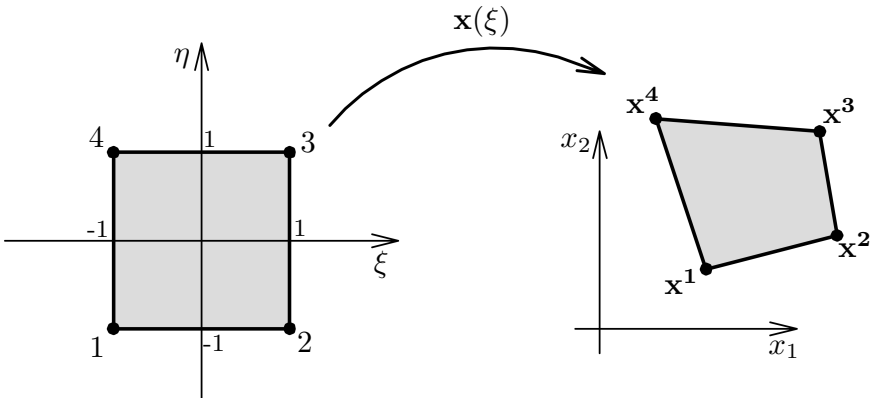

FIGURE 2.7: Association between element coordinates of a standard quadrilateral element from the local to global coordinates.

2.4.3 Linearization of the virtual work equation

The derivation of the virtual work equation was presented on section 2.3.3.

A common procedure to solve the initial boundary value problem employees the linearized form of the virtual work equation. The stress tensor is a function of the strain, which is also a function of the displacement field as follows:

$$\boldsymbol{\sigma} = \boldsymbol{\sigma}(\boldsymbol{\varepsilon}(\mathbf{u})) = \boldsymbol{\sigma}(\nabla^s \mathbf{u}). \tag{2.47}$$

Recalling at this point the virtual work equation.

$$\delta W(\boldsymbol{\phi}, \boldsymbol{\eta}) = \int_v \boldsymbol{\sigma} : \delta \mathbf{d}\, dv - \int_v \mathbf{b} \cdot \boldsymbol{\eta}\, dv - \int_{\partial v} \mathbf{t} \cdot \boldsymbol{\eta}\, da = 0 \tag{2.48}$$

where $\boldsymbol{\phi}$ is a kinematic admissible displacement field, $\boldsymbol{\eta}$ is the virtual velocity vector, $\boldsymbol{\sigma}$ is the strain tensor, $\mathbf{b}$ represents the body forces and $\mathbf{t}$ are the surface tractions.

The previous equation can be linearized in the direction of an increment $\mathbf{u}$ relatively to a fixed position field $\boldsymbol{\phi}_0$ as,

$$\delta W(\boldsymbol{\phi}_0, \boldsymbol{\eta}) + D\delta W(\boldsymbol{\phi}_0, \boldsymbol{\eta})[\mathbf{u}] = 0. \tag{2.49}$$

To the compute the derivative $D\delta W(\boldsymbol{\phi}_0, \boldsymbol{\eta})$ it is useful to perform the following decomposition:

$$D\delta W(\boldsymbol{\phi}, \boldsymbol{\eta})[\mathbf{u}] = D\delta W_{int}(\boldsymbol{\phi}, \boldsymbol{\eta})[\mathbf{u}] - D\delta W_{ext}(\boldsymbol{\phi}, \boldsymbol{\eta})[\mathbf{u}]. \tag{2.50}$$

$$\delta W_{int}(\boldsymbol{\phi}, \boldsymbol{\eta})[\mathbf{u}] = \int_v \boldsymbol{\sigma} : \delta \mathbf{d} \, dv \tag{2.51}$$

$$\delta W_{ext}(\boldsymbol{\phi}, \boldsymbol{\eta})[\mathbf{u}] = \int_v \mathbf{b} \cdot \boldsymbol{\eta} \, dv + \int_{\partial v} \mathbf{t} \cdot \boldsymbol{\eta} \, da \tag{2.52}$$

In the previous expressions, the function $D\delta W_{int}(\boldsymbol{\phi}, \boldsymbol{\eta})$ represents the derivative of the virtual work due to internal components, while the function $D\delta W_{ext}(\boldsymbol{\phi}, \boldsymbol{\eta})$ represents the derivative of the virtual work due to external components.

2.4.4 Newton-Raphson Method

The Newton-Rapson method is a numerical scheme for solving non linear systems of equations. The underlying idea of the method is briefly explained bellow.

Consider the following generic system of equations

$$\mathbf{F}(\mathbf{x}) = \mathbf{0}. \tag{2.53}$$

Where $\mathbf{x}$ is a generic vector defined in $\mathbb{R}^n$ and $\mathbf{F}(\mathbf{x})$ is a vector valued function that performs a transformation of the type $\mathbb{R}^n \rightarrow \mathbb{R}^n$. The linearization of the function $\mathbf{F}(\mathbf{x})$ in turn of a fixed point $\mathbf{x}_0$ (considering Taylor's formula) provides the following approximation:

$$\mathbf{F}(\mathbf{x}_0) + \left.\frac{\partial \mathbf{F}}{\partial \mathbf{x}}\right|_{\mathbf{x}_0} (\mathbf{x} - \mathbf{x}_0) = \mathbf{0} \tag{2.54}$$

Generally (if the conditions of convergence of the method are meet) the solution of Equation (2.54) provides a more approximate solution to (2.53) than $\mathbf{x}_0$. For that reason, the application of the previous expression several times (updating $\mathbf{x}_0$ with the most approximate solution), leads to a succession of values that converges to the exact solution.

The employment of the Newton-Raphson method to solve the equilibrium equations, which is suggested by many authors, is described by the following.

Recalling the principle of virtual work, which was described in the previous sections,

$$\delta W(\boldsymbol{\phi}, \boldsymbol{\eta}) \quad = \quad 0. \tag{2.55}$$

Due to the spatial discretization of the continuum equations is possible to write

$$\delta W(\boldsymbol{\phi}, \boldsymbol{\eta}) \quad = \quad \boldsymbol{\eta}^T \mathbf{R}(\boldsymbol{\phi}), \tag{2.56}$$

where $\boldsymbol{\eta}$ and $\mathbf{R}$ are vectors containing the virtual velocities and the unbalance of forces in the discretization points.

The derivatives can be expressed as follows:

$$\frac{\partial \delta W}{\partial \boldsymbol{\phi}}(\boldsymbol{\phi}_k, \boldsymbol{\eta}) \quad = \quad \boldsymbol{\eta}^T \mathbf{K} \tag{2.57}$$

where $\mathbf{K}$ is tangent matrix defined as:

$$\mathbf{K} = \left. \frac{\partial \mathbf{R}}{\partial \boldsymbol{\phi}} \right|_{\boldsymbol{\phi}=\boldsymbol{\phi}_k}. \tag{2.58}$$

The linearization of δW in turn of $\boldsymbol{\phi}_k$ becomes:

$$\delta W(\mathbf{u}, \boldsymbol{\eta}) \quad = \quad \boldsymbol{\eta}^T \mathbf{K}\mathbf{u} + \delta W(\mathbf{u}, \boldsymbol{\phi}_k) \quad \text{with} \quad \mathbf{u} = \boldsymbol{\phi}_{k+1} - \boldsymbol{\phi}_k \tag{2.59}$$

and the equation (2.55) in the linearized form becomes:

$$\boldsymbol{\eta}^T \mathbf{K}\mathbf{u} + \boldsymbol{\eta}^T \mathbf{R}(\boldsymbol{\phi}_k) \quad = \quad 0 \tag{2.60}$$

The previous expression, should be valid for any $\boldsymbol{\eta}$ and therefore can vanish from that expression, giving rise to the following iterative formula:

$$\mathbf{K}\mathbf{u} \quad = \quad -\mathbf{R}(\boldsymbol{\phi}_k); \quad \boldsymbol{\phi}_{k+1} = \boldsymbol{\phi}_k + \mathbf{u} \tag{2.61}$$

where $\boldsymbol{\phi}_k$ is the displacement vector in the current iteration (k) and $\boldsymbol{\phi}_{k+1}$ is the updated displacement vector for the next iteration $(k+1)$.

2.4.5 Overall Algorithm

The Newton-Raphson algorithm for the solution of the incremental Finite Element Method [17] is summarized on Table 2.1.

TABLE 2.1: Newton-Raphson algorithm for solution of the equilibrium problem.

(1) Compute the initial values.
$\boldsymbol{\phi}_{n+1}^{0} \leftarrow \boldsymbol{\phi}_n$ (initial displacements)
$\mathbf{r} \leftarrow \mathbf{f}_{n+1}^{int}(\boldsymbol{\phi}_n) - \lambda_{n+1}\mathbf{f}^{ext}$ (λ_{n+1} is the loading factor of the loading increment $n+1$)
$k \leftarrow 0$ (counter)

(2) Increment the counter.
$k \leftarrow k+1$

(3) Compute stiffness matrix.
$\mathbf{K}_T \leftarrow \partial\mathbf{r}/\partial\boldsymbol{\phi}_{n+1}^{k}$

(4) Compute displacement increment. Solve for $\mathbf{u}^k$:
$\mathbf{K}_T\,\mathbf{u}^k = -\mathbf{r}^{k-1}$

(5) Update global displacements.
$\boldsymbol{\phi}_{n+1}^{k} \leftarrow \boldsymbol{\phi}_{n+1}^{k-1} + \mathbf{u}^k$

(6) Update deformations.
$\boldsymbol{\varepsilon}_{n+1}^{k} \leftarrow \mathbf{B}\boldsymbol{\phi}_{n+1}^{k}$

(7) Update stress tensor and internal variables
$\boldsymbol{\sigma}_{n+1}^{k} \leftarrow \boldsymbol{\sigma}(\boldsymbol{\alpha}_n, \boldsymbol{\varepsilon}_{n+1}^{k})$
$\boldsymbol{\alpha}_{n+1}^{k} \leftarrow \boldsymbol{\alpha}(\boldsymbol{\alpha}_n, \boldsymbol{\varepsilon}_{n+1}^{k})$

(8) Compute internal forces.
$\mathbf{f}^{int} \leftarrow Assem(\mathbf{f}_e^{int})$

(9) Compute the residual.
$\mathbf{r} \leftarrow \mathbf{f}(\boldsymbol{\phi}_{n+1}^{k}) - \lambda_{n+1}\mathbf{f}^{ext}$

(10) Check convergence criterion (using the residual $\mathbf{r}$)
if Convergence criterion is meet **then**
  Finish.
else
  Continue from item 2.
end if

Chapter 3

Analytical and Computational Homogenization

3.1 Introduction

In conventional simulation models it is usual to assume that the materials are homogeneous at the microscale. The homogeneity assumption is very convenient because it allows the characterization of those domains not only in terms of state variables (stress, strain, temperature, etc.), but also in terms of functionality (constitutive behavior) on a continuous fashion. This continuous description allows the formulation of the problems with continuous functions and also enabling the application of infinitesimal calculus theories and the associated numerical techniques. Many times, however, structures are composed by heterogeneous materials as in the case of composite structures, for example. One way to overcome this problem is to split the structure on several domains such that in each domain the material could be considered homogeneous. Nonetheless, this strategy could lead to very complex problems that demand a significant amount of computational power, time and memory. For that reason, a multiscale model can provide a more efficient approximation.

3.2 Multiscale models

As previously stated, materials in general are not homogeneous and different scales of detail can be considered in order to describe them, namely structural-scale, meso-scale, micro-scale, among others. When using a multi-scale strategy to describe the constitutive behavior of a material, different material scales are assumed and a strategy

to connect them is employed. To attain simplicity, only two scales are assumed along this work: the macro scale and the micro scale.

3.2.1 Micro scale and macro scale

On the micro scale, the material is modeled with high detail and many of its phenomena and characteristics are taken under consideration. On the macro scale, the material is studied with less detail than in the micro scale; besides the phenomena and the state of the material are described as simplifications of micro scale analysis, e.g. using overall average or continuum counterparts of a discontinuous medium. Those simplifications are, for example, the consideration that at the macroscale the stress is a continuous field obtained as the average of the stress at the microscale. Therefore, to each of the scales it is possible to set a different model that has its own variables and algorithms to simulate what happens at that scale. However, the two scales must respect some relations between them in order to satisfy the governing principles of continuum mechanics. These relations are critical to the success of the overall theory and have been developed within the so-called homogenization theory. To distinguish the same type of quantities on the different scales, some conventions are employed: variables with the μ index ($\mathbf{F}_\mu$ for example) refer to the micro scale models while variables with the a bar ($\bar{\mathbf{F}}$ for example) refer to the macro scale. Furthermore, variables in upper case ($\mathbf{X}$ or $\mathbf{Y}$ for example) refer to the undeformed or initial configuration, while variables in lowercase ($\mathbf{x}$ or $\mathbf{y}$ for example) refer to the deformed or final configuration.

3.2.2 Representative volume element

The study of the material at the macroscale is linked to the behavior of the material at the microscale in each macroscopic point. The domain of study of the micro scale phenomena it is called Representative Volume Element (RVE). In Figure 3.1, it is schematically represented a generic RVE and its correspondence to the material point at the structural level.

3.2.3 Average quantities

An important relationship between the variables at both micro and macro scale is the average of the micro scale variables on the RVE. The average of one variable at the micro scale, in the domain of the RVE, is defined by the following expression:

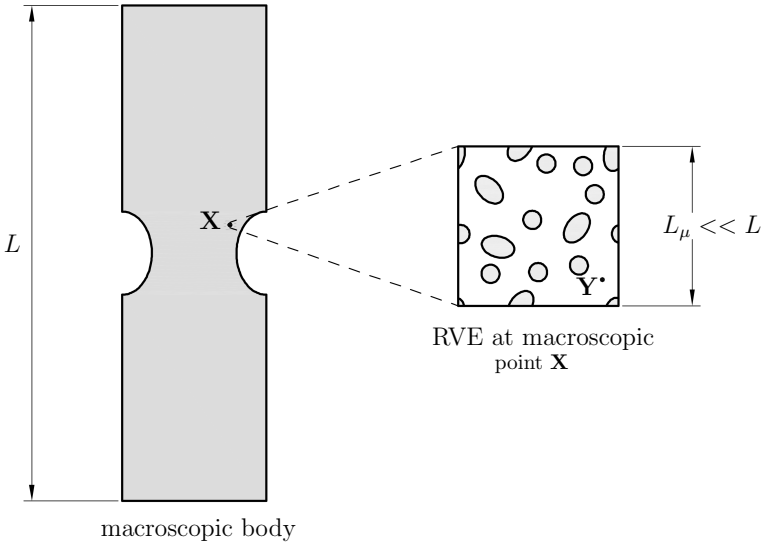

FIGURE 3.1: Schematic representation of an RVE at micro scale associated to a generic macro scale point.

$$\langle \bullet \rangle_0 = \frac{1}{V_\mu} \int_{\mathbb{V}} \bullet \, dV. \tag{3.1}$$

On the previous expression, V_μ is the volume of the RVE and $\mathbb{V}$ is the domain of integration of the RVE.

3.2.4 Hill-Mandel Principle

The principle of Hill-Mandel, also called homogenization principle, is based on the energy conservation. Hill-Mandel principle states that the power of the deformation processes at the macro scale should be the same as the average of the power of deformation processes at the micro scale on the RVE, according to the following expression:

$$\bar{\mathbf{P}} : \dot{\bar{\mathbf{F}}} \;=\; \frac{1}{|\mathbb{V}|} \int_{\mathbb{V}} \mathbf{P}_\mu : \dot{\mathbf{F}}_\mu \, dV \tag{3.2}$$

where $\bar{\mathbf{P}}$ is the macroscale first Piolla-Kirchhoff stress tensor and $\mathbf{P}_\mu$ is the first Piolla-Kirchhoff stress tensor at the microscale.

3.2.5 Connection between scales

In general, at the macroscopic level where the structures are modeled (using for instance FEM) the materials are considered continuous and locally homogeneous. This continuity and homogeneity is considered in the constitutive model defined for the materials. Additionally, a micro scale model and the corresponding RVE are employed to describe the behavior of the material.

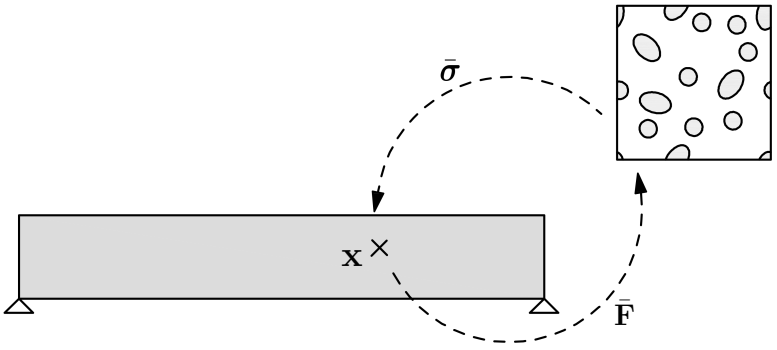

FIGURE 3.2: Linkage between macro scale and micro scale

The linkage between the two scales could be done by a strain approximation (Figure 3.2). On this type of approximation, the macro scale model outputs the deformation state of the material and expects to access the correspondent stress state. The micro scale model receives the deformation state as input and returns the correspondent stress state. However, the variables from the macro scale must be converted to use in the micro scale; similarly variables from the micro scale require conversion to the macro scale. In resume, there are four components of the overall model:

1. Macro Scale Model;
2. Micro Scale Model;
3. Conversion procedure between macro data and micro data;
4. Conversion procedure between micro data and macro data.

For the micro and macro scale models, standard methods such as Finite Element Method or Discrete Element Method, among others, could be used. The deformation gradient $\mathbf{F}(\mathbf{X}, t)$ can be passed from the macro scale to define the deformation state. In the micro scale model, a particle at the position $\mathbf{Y}$ on the RVE around the point $\mathbf{X}$ could be expressed as:

$$\mathbf{y}(\mathbf{Y},t) \quad = \quad \bar{\mathbf{F}}(\mathbf{X},t)Y + \tilde{\mathbf{u}}(\mathbf{Y},t) \tag{3.3}$$

where $\bar{\mathbf{F}}(\mathbf{X},t)$ is the deformation gradient around the point $\mathbf{X}$ at the macroscale. So $\bar{\mathbf{F}}(\mathbf{X},t)\mathbf{Y}$ represents the homogeneous component of the deformations and $\tilde{\mathbf{u}}(\mathbf{Y},t)$ represents the *displacement fluctuations* at the micro scale.

3.2.6 Equilibrium equations

The translation equilibrium condition of a general body was described in Chapter 2, on the expression (2.32) for the initial configuration. Recalling that equation, and now considering the domain of the RVE expressed in the strong form it is possible to write:

$$div_Y \mathbf{P}_\mu + \mathbf{B}_\mu \quad = \quad \mathbf{0} \tag{3.4}$$

$$\mathbf{P}_\mu \mathbf{N} + \mathbf{T}_\mu \quad = \quad \mathbf{0} \tag{3.5}$$

where div_Y represents the divergence with respect to the reference position $\mathbf{Y}$, $\mathbf{B}_\mu$ is the body force per unit reference volume, $\mathbf{T}_\mu$ is the traction per unit reference area on the boundary surface having normal $\mathbf{N}$.

An equivalent statement of the equilibrium of the RVE in the weak form can be written using the Virtual Work Principle mentioned on section 2.3.3. The expression (3.6) describes this principle considering the domain of the RVE.

$$\int_{\mathbb{V}} \mathbf{P}_\mu : \nabla_Y \boldsymbol{\eta}\, dV - \int_{\mathbb{V}} \mathbf{B}_\mu \cdot \boldsymbol{\eta}\, dV - \int_{\partial\mathbb{V}} \mathbf{T}_\mu \cdot \boldsymbol{\eta}\, dA = 0 \tag{3.6}$$

where $\boldsymbol{\eta}$ is any virtual admissible displacement field.

3.2.7 Boundary conditions

The boundary conditions at the RVE must respect the Hill-Mandel principle and the equilibrium principles. Four classical types of boundary constraints are:

1. Taylor assumption;
2. Linear displacements on the boundary;
3. Periodic displacements on the boundary;
4. Uniform traction on the boundary.

The following decomposition of the displacement field $\mathbf{u}(\mathbf{y})$ is usual considered:

$$\mathbf{u}(\mathbf{y}) = \mathbf{y}(\mathbf{Y}) - \mathbf{Y} = [\bar{\mathbf{F}}(\mathbf{x}) - \mathbf{I}]\mathbf{Y} + \tilde{\mathbf{u}}(y) \tag{3.7}$$

the component $[\bar{\mathbf{F}} - \mathbf{I}]\mathbf{Y}$ is called *Taylor displacement*. The refereed decomposition allows to rewrite the Hill-Mandel principle as follows:

$$\langle \mathbf{P}_\mu : \dot{\mathbf{F}}_\mu \rangle_0 \quad = \quad \langle \mathbf{P}_\mu \rangle_0 : \langle \dot{\mathbf{F}}_\mu \rangle_0 \tag{3.8}$$

$$\langle \mathbf{P}_\mu : (\dot{\mathbf{F}} + \nabla_Y \dot{\tilde{\mathbf{u}}}_\mu) \rangle_0 \quad = \quad \langle \mathbf{P}_\mu \rangle_0 : \langle \dot{\mathbf{F}}_\mu \rangle_0 \tag{3.9}$$

$$\Leftrightarrow \quad \langle \mathbf{P}_\mu : \dot{\mathbf{F}} \rangle_0 + \frac{1}{V_\mu} \int_{\mathbb{V}} \mathbf{P}_\mu : \nabla_Y \dot{\tilde{\mathbf{u}}}_\mu dV = \langle \mathbf{P}_\mu \rangle_0 : \langle \dot{\mathbf{F}}_\mu \rangle_0 \tag{3.10}$$

$$\Leftrightarrow \quad \langle \mathbf{P}_\mu \rangle_0 : \langle \dot{\mathbf{F}}_\mu \rangle_0 + \frac{1}{V_\mu} \int_{\mathbb{V}} \mathbf{P}_\mu : \nabla_Y \dot{\tilde{\mathbf{u}}}_\mu dV = \langle \mathbf{P}_\mu \rangle_0 : \langle \dot{\mathbf{F}}_\mu \rangle_0 \tag{3.11}$$

$$\Leftrightarrow \quad \frac{1}{V_\mu} \int_{\mathbb{V}} \mathbf{P}_\mu : \nabla_Y \dot{\tilde{\mathbf{u}}}_\mu dV = 0. \tag{3.12}$$

Integrating the previous equation by parts leads to:

$$\int_{\partial \mathbb{V}} (\mathbf{P}_\mu \mathbf{N}) . \dot{\tilde{\mathbf{u}}} dA - \int_{\mathbb{V}} (div_Y \mathbf{P}_\mu) . \dot{\tilde{\mathbf{u}}} dV = 0. \tag{3.13}$$

Taking into account the equilibrium equations of the RVE in the strong form (3.4) and (3.5).

$$\frac{1}{\mathbb{V}}\int_{\mathbb{V}} \mathbf{B}_\mu : \dot{\tilde{\mathbf{u}}} dV - \frac{1}{\mathbb{V}}\int_{\partial\mathbb{V}} \mathbf{T}_\mu . \dot{\tilde{\mathbf{u}}} dA = 0. \tag{3.14}$$

Note that the expression (3.14) only depends on the displacement fluctuations. Considering this expression, some classical assumptions can be derived.

3.2.7.1 Taylor assumption

Regarding, the Taylor assumption boundary conditions, it is considered that the displacement field is uniform, which means there are no displacement fluctuations.

$$\tilde{\mathbf{u}}(\mathbf{y}) = \mathbf{0} \quad \mathbf{y} \in \mathbb{V} \tag{3.15}$$

The displacements are given by:

$$\mathbf{u}(\mathbf{y}) = [\bar{\mathbf{F}}(\mathbf{x}) - \mathbf{I}]\mathbf{Y}. \tag{3.16}$$

3.2.7.2 Linear displacements on the RVE boundary

It is also possible to assume linear displacements only on the boundary of the RVE, accordingly the expression that follows:

$$\tilde{\mathbf{u}}(\mathbf{y}) = \mathbf{0} \quad \mathbf{y} \in \partial\mathbb{V} \tag{3.17}$$

The displacements are given by:

$$\begin{aligned} \mathbf{u}(\mathbf{y}) &= [\bar{\mathbf{F}}(\mathbf{x}) - \mathbf{I}]Y & \mathbf{y} \in \partial\mathbb{V} \\ \mathbf{u}(\mathbf{y}) &= [\bar{\mathbf{F}}(\mathbf{x}) - \mathbf{I}]\mathbf{Y} + \tilde{\mathbf{u}}(\mathbf{y}) & \mathbf{y} \notin \partial\mathbb{V} \end{aligned} \tag{3.18}$$

Note that this second condition only satisfies the Hill-Mandel principle (equation (3.14)) if the body forces are negligible.

$$\frac{1}{\mathbb{V}}\int_{\mathbb{V}} \mathbf{B}_\mu : \dot{\tilde{\mathbf{u}}} dV - \frac{1}{\mathbb{V}}\int_{\partial\mathbb{V}} \mathbf{T}_\mu . \dot{\tilde{\mathbf{u}}} dA \approx \frac{1}{\mathbb{V}}\int_{\partial\mathbb{V}} \mathbf{T}_\mu . \dot{\tilde{\mathbf{u}}} dA = 0 \tag{3.19}$$

3.2.7.3 Periodic displacements on the RVE boundary

As far as this approximation is concerned, the body force is also not taken into account, and the boundary of the RVE is split in two symmetric parts $\partial\mathbb{V}^+$ and $\partial\mathbb{V}^-$ as in Figure 3.3.

$$\partial\mathbb{V} = \partial\mathbb{V}^+ \cup \partial\mathbb{V}^- \tag{3.20}$$

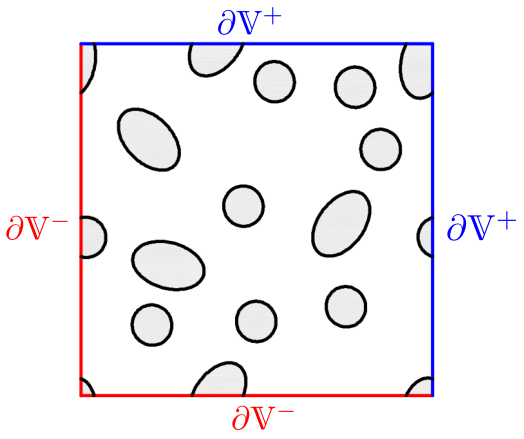

FIGURE 3.3: Decomposition of the domain in two symmetric parts.

Considering $\mathbf{Y}^+$ and $\mathbf{Y}^-$ to be a pair of opposite points on $\partial\mathbb{V}^+$ and $\partial\mathbb{V}^-$ as in expressions (3.21) and (3.22).

$$\mathbf{Y}^+ = \mathbf{Y} \in \partial\mathbb{V}^+ \tag{3.21}$$

$$\mathbf{Y}^- = \mathbf{Y} \in \partial\mathbb{V}^- \tag{3.22}$$

The displacement fluctuation field $\tilde{\mathbf{u}}$ in the RVE boundary, can be defined as periodic, accordingly the following (expression(3.23)).

$$\tilde{\mathbf{u}}(\mathbf{Y}^+) = \tilde{\mathbf{u}}(\mathbf{Y}^-) \tag{3.23}$$

Hence, the normal vectors $\mathbf{n}$ to the RVE boundary in those two counterpart points are symmetric (expression(3.24)).

$$\mathbf{n}(\mathbf{Y}^+) = -\mathbf{n}(\mathbf{Y}^-) \tag{3.24}$$

Accordingly, the deformation fluctuations in the boundary is symmetric and the traction in the boundary is anti-symmetric. This condition allows equation (3.19) to be

satisfied. The periodic boundary condition can be used on materials with repetitive microstructure, such as the crystals, for example.

3.2.7.4 Uniform traction on the RVE boundary

When neglecting the body forces $\mathbf{B}_\mu = \mathbf{0}$ the condition (3.14) can be written as follows:

$$\int_{\partial \mathbb{V}} \mathbf{T}_\mu \cdot \dot{\tilde{\mathbf{u}}} dA = 0 \tag{3.25}$$

Considering same averaged gradient field between scales (equation (3.26)).

$$\langle \, \mathbf{F}_\mu \, \rangle_0 = \bar{\mathbf{F}} \tag{3.26}$$

It is possible to derive the following expression (3.27):

$$\Leftrightarrow \quad \langle \, \bar{\mathbf{F}} + \nabla_{\mathbf{Y}} \tilde{\mathbf{u}} \, \rangle_0 = \bar{\mathbf{F}} \quad \Leftrightarrow \quad \langle \, \nabla_{\mathbf{Y}} \tilde{\mathbf{u}} \, \rangle_0 = \mathbf{0} \quad \Leftrightarrow \quad \int_{\mathbb{V}} \nabla_{\mathbf{Y}} \tilde{\mathbf{u}} dV = \mathbf{0} \quad \Leftrightarrow$$

$$\int_{\partial \mathbb{V}} \tilde{\mathbf{u}} \otimes \mathbf{N} dA = \mathbf{0} \tag{3.27}$$

Furthermore, it is possible to demonstrate that the previous equations (3.25) and (3.27) led to the condition (3.28) (see [21] for a demonstration).

$$\mathbf{P}_\mu(\mathbf{Y}) \, \mathbf{N}(\mathbf{Y}) = \bar{\mathbf{P}}(\mathbf{X}) \, \mathbf{N}(\mathbf{Y}) \qquad \forall \mathbf{Y} \in \partial \mathbb{V} \tag{3.28}$$

The condition (3.28) it is also known as *uniform traction boundary condition*.

3.3 Spatial discretization of the microscopic problem

The equilibrium of the RVE is governed by the virtual work principle (equation (3.6)). Neglecting the body forces ($\mathbf{B}_\mu = \mathbf{0}$) and the traction per unit reference area on the boundary ($\mathbf{T}_\mu = \mathbf{0}$) the following equation is obtained:

$$\int_{\mathbb{V}} \mathbf{P}_\mu : \nabla_Y \boldsymbol{\eta} dV \quad = \quad 0. \tag{3.29}$$

The discretized form of the previous equation can be written as follow:

$$\int_{\mathbb{V}} (\mathbf{G}^g)^T \mathbf{P}(\mathbf{y}) dV = \mathbf{0} \tag{3.30}$$

In (3.30), $\mathbf{G}^g$ is the so called discrete material gradient operator, which is a discretized version of the gradient operator ∇_Y in the initial configuration. The previous equation can be solved with the Finite Element Method. Since the previous equation is nonlinear, the Newton-Raphson method can be used to solve it. In order to apply that method, the following linearization is required:

$$\mathbf{f}_{int} + \mathbf{K}(\mathbf{y}) \delta \tilde{\mathbf{u}} = \mathbf{0}, \tag{3.31}$$

where $\delta \tilde{\mathbf{u}}$ is a vector with the discretized fluctuations of displacements, $\mathbf{f}_{int}$ is the internal force vector and $\mathbf{K}$ is the global stiffness matrix. The internal force vector is defined as follows:

$$\mathbf{f}_{int} = \mathbf{Assem} \int_{\mathbb{V}} \mathbf{G}^T \mathbf{P}(\mathbf{y}) dV. \tag{3.32}$$

While, the global stiffness matrix is defined by:

$$\mathbf{K} = \mathbf{Assem} \int_{\mathbb{V}} \mathbf{G}^T \mathbb{A} \mathbf{G} dV. \tag{3.33}$$

In the previous equation, $\mathbb{A}$ is a forth-order tensor called the material tangent modulus

$$\mathbb{A} = \frac{\partial \mathbf{P}(\mathbf{y})}{\partial \mathbf{F}(\mathbf{y})} \tag{3.34}$$

Equation (3.30) does not take into account the boundary conditions, that should be introduced by adding some constrains depending on the chosen type.

3.3.1 Linear displacements on the RVE boundary

Recalling the linear boundary condition of the body as

$$\tilde{\mathbf{u}}(\mathbf{Y}) = \mathbf{0} \quad \mathbf{Y} \in \partial \mathbb{V} \tag{3.35}$$

This could be fulfilled by choosing the following decomposition for the fluctuation displacement vector

$$\tilde{\mathbf{u}}(\mathbf{Y}) = \left\{ \begin{array}{c} \tilde{u}_i \\ \tilde{u}_b \end{array} \right\} \tag{3.36}$$

where $\tilde{u}_i$ corresponds to fluctuations on the degrees of freedom of the internal nodes and $\tilde{u}_b$ corresponds to the degrees of freedom of the nodes on the boundary. This allow the equation (3.31) to be rewritten as:

$$\left\{ \begin{array}{c} f_i \\ f_b \end{array} \right\} + \left[\begin{array}{cc} k_{ii} & k_{ib} \\ k_{bi} & k_{bb} \end{array} \right] \left\{ \begin{array}{c} \delta\tilde{u}_i \\ \delta\tilde{u}_b \end{array} \right\} = \left\{ \begin{array}{c} 0 \\ 0 \end{array} \right\} \tag{3.37}$$

Since we impose that $\tilde{\mathbf{u}}_b$ is null, then is possible to write:

$$\left\{ -f_i \right\} = \left[k_{ii} \right] \left\{ \delta\tilde{u}_i \right\}. \tag{3.38}$$

3.3.2 Periodic displacements on the RVE boundary

Under the periodic boundary condition, displacement fluctuations at the boundary of the RVE are enforced to be the same at opposite points of the boundary, as follows:

$$\mathbf{Y}^+ = \mathbf{Y} \in \partial\mathbb{V}^+ \tag{3.39}$$

$$\mathbf{Y}^- = \mathbf{Y} \in \partial\mathbb{V}^- \tag{3.40}$$

$$\mathbf{n}(\mathbf{Y}^+) = \mathbf{n}(\mathbf{Y}^-) \tag{3.41}$$

$$\tilde{\mathbf{u}}(\mathbf{Y}^+) = \tilde{\mathbf{u}}(\mathbf{Y}^-) \tag{3.42}$$

This allows discrete equation (3.31) to be expressed as:

$$\left\{ \begin{array}{c} f_i \\ f_+ \\ f_- \end{array} \right\} + \left[\begin{array}{ccc} k_{ii} & k_{i+} & k_{i-} \\ k_{+i} & k_{++} & k_{+-} \\ k_{-i} & k_{-+} & k_{--} \end{array} \right] \left\{ \begin{array}{c} \delta\tilde{u}_i \\ \delta\tilde{u}_+ \\ \delta\tilde{u}_- \end{array} \right\} = \mathbf{0}. \tag{3.43}$$

The previous system can be rearranged as follows:

$$-\left\{\begin{array}{c} f_i \\ f_+ + f_- \end{array}\right\} = \left[\begin{array}{cc} k_{ii} & k_{i+} + k_{i-} \\ k_{+i} + k_{-i} & k_{++} + k_{-+} + k_{+-} + k_{--} \end{array}\right] \left\{\begin{array}{c} \delta\tilde{u}_- \\ \delta\tilde{u}_+ \end{array}\right\}. \tag{3.44}$$

To avoid rigid body displacements, or rotations of the RVE, some artificial constrains need to be included. Usually, a minimum of two degrees of freedom are constrained in 2D problems and three in the 3D problems, using prescribed displacements. These artificial constraints must preserve the basic hypothesis of periodic boundary fluctuation of displacements.

3.4 Algorithm to solve the micro scale problem in three dimensions RVEs

With the aim of predicting the macroscopic behavior of the materials due to microscale effects on a tri-dimensional RVEs, a computer program was developed. The presented algorithm, corresponds to an extension of an original algorithm, initially, proposed by Reis [22] for the solution of bi-dimentional problems and based on an academic FEM code described in [17].

Overview of the algorithm It is important to mention that the code has a modular structure and supports any constitutive model for the constituents (i.e. elasticity, plasticity, hyperelasticity, damage). An overview of the developed algorithm is provided in Table 3.1.

TABLE 3.1: Micro scale algorithm for 3D RVEs.

(1) Initialization of the RVE data:

- Mesh;
- Constitutive models and material properties;
- Number of increments (N_{inc});
- Boundary conditions;
- Macroscopic deformation gradient.

(2) Identify the groups of the nodes of the mesh according its position:

- Interior, Vertex, Edge;
- Face normal to X axis, with higher and lower x coordinate;
- Face normal to Y axis, with higher and lower y coordinate;
- Face normal to Z axis, with higher and lower z coordinate.

(3) Compute the incremental linear displacement vector:
$\Delta\mathbf{u}^*(\mathbf{y}) \leftarrow (\bar{\mathbf{F}}(\mathbf{x}) - \mathbf{I})\mathbf{Y}/N_{inc}$.

(4) Set the fluctuation displacement vector to zero:
$\tilde{\mathbf{u}}(\mathbf{y}) \leftarrow \mathbf{0}$.

(5) Update the total displacement vector:
$\mathbf{u}(\mathbf{y}) \leftarrow \Delta\mathbf{u}^*(\mathbf{y}) + \tilde{\mathbf{u}}(\mathbf{y})$.

(6) Compute the global internal force vector.

(7) Check convergence:
if CONV < TOL **then**
  Compute the macroscopic stress tensor.
  if N = N_{inc} **then**
    Exit.
  else
    $N \leftarrow N + 1$
    Go to 5.
  end if
end if

(8) Assemble and solve the systems of equations:

- Linear boundary condition (equation 3.38);
- Periodic boundary condition (equation 3.44)

(9) Update displacements:
$\tilde{\mathbf{u}}(\mathbf{y}) = \tilde{\mathbf{u}}(\mathbf{y}) + \delta\tilde{\mathbf{u}}(\mathbf{y})$.
(10) Go to 5.

Chapter 4

Development of an improved multi-scale algorithm

4.1 Introduction

In the previous chapters, the analytical and numerical concepts for homogenization have been described. However, when dealing with practical problems, that consider a large number of degrees of freedom, a high demand of computational resources arise, see for instance [23] and [24]. Futhermore, computational efficiency is especially important when the macroscopic solution strictly depends on the microscopic deformation history [24]. Therefore, in this chapter an improved homogenization framework is described. Additionally, in the implementation it was considered that the nodes of the mesh between opposite edges (or faces) of the RVE may not match when projected normally to the edges (or faces); moreover interpolation between nodes was used to enforce the boundary conditions as it will be explained forward. To develop this framework, two computational techniques are employed in order to improve efficiency and reduce of physical memory required. Firstly, a data structure named *hash table* was used in order to handle the sparse stiffness matrix, allowing to impose arbitrary boundary conditions with a reduced consumption of memory. Secondly, a numerical method *Generalized Minimum Residual* (GMRES), that allows the solution of very large systems of equations in an iterative manner was chosen. As it will be shown, the use of *hash tables* is very convenient to the enforcement of arbitrary boundary conditions and to the use of interpolation when enforcing that b.c.

4.2 Enforcement of boundary conditions on arbitrary meshes

As described in Chapter 3 about homogenization, certain types of boundary conditions relate points that are directly opposed on the RVE boundary. The periodic boundary condition, described on expression (3.23), is an important example of this. If the mesh is defined in such a way that the nodes from opposite edges (or faces) of the boundary match when projected in the normal direction, then we can call it *periodic mesh*. Using a *periodic mesh*, the degrees of freedom (d.o.f.) of the nodes from opposite boundaries of RVE can be directly related. The periodic boundary conditions (b.c.) for instance can be directly enforced using the expressions (3.44) already mentioned. However, for arbitrary meshes, it is not possible to relate directly the degrees of freedom between opposite edges (or faces) of the boundary, using the expressions (3.44). When the size of the RVE is large, in order to be representative, it is naturally difficult to generate a *periodic mesh*. Some mesh generation libraries (see for instance MAdLib [25] or Yams [26]) allow the generation of *periodic meshes*, but usually some expertise is required, since those libraries are often based on heuristic rules, especially in the 3D case, that does not guarantee a successful meshing in all the situations. Moreover, the requirement of have a *periodic mesh* is clearly a limitation for practical applications. To overcome this limitation, some solutions have been proposed, for instance the works [27], [28] and [29] use a strategy of interpolation to relate the d.o.f. of opposite boundaries whose nodes do not match. A mortar based approach to enforce the periodic boundary conditions was also proposed on [30]. The mortar method is designed to enforce constraints over a interacting non-conform domains and is based in the Lagrange method. In this work, the interpolation method was used to enforce the boundary conditions and the periodic b.c. in particular, because of its simplicity of formulation and implementation, not disregarding the fact that it does not affect adversely the computation speed and operating memory required.

4.2.1 Enforcement of boundary conditions using interpolation

Regarding this strategy, one of the two matching boundary domains is considered master and the other the slave. The master and slave edges (or faces) oppose each other. When a restriction is established, the nodes in the master domain are considered with their values, and related with coordinates of *virtual matching nodes* on the slave domain. The *virtual nodes* result from the projection of the nodes from the master domain to the slave one and are used as a numerical artifice. The value corresponding to each d.o.f of a *virtual node* is determined as a function of values of the d.o.f. of the nodes in the slave domain, as presented in the following expression.

$$v_i = f_i(u_1, u_2, \ldots, u_n) \tag{4.1}$$

Where v_i is the value for a d.o.f. of a *virtual node*, $u_1, u_2, \ldots, u_n$ are values for d.o.f. of node in the slave domain, and f_i is a general interpolation function. The equation (4.1) can be combined with (3.44) to define the periodic b.c. in a general mesh. However, it is certainly convenient to maintain the periodic b.c. linear. Therefore, the equation (4.1) should assume the form:

$$v_i = \sum_j a_{ij}.u_j. \tag{4.2}$$

In this last linear expression, a_{ij} are weighting values, and u_j are the values corresponding to nodes in the surroundings of the virtual node. This expression requires the determination of the surrounding nodes of the virtual node and the evaluation of the interpolation coefficients a_{ij}. Note that this procedure is executed only one time, when the boundary conditions are imposed. We describe two possibilities to determine those nodes and the corresponding coefficients:

- use the FEM interpolation framework;
- generate an auxiliary mesh and interpolation functions.

These two possibilities are explained forward.

Use the FEM interpolation framework

In order to use the FEM mesh for interpolation, it is required to find the element (or the face of the element in the 3D case) in which the polygon encloses the virtual node to interpolate. The coordinates of the nodes and shape functions from this element are used to determine the interpolation coefficients a_{ij}.

Recalling Figure 2.7, let us assume that on the right it is represented the element enclosing the virtual node with the coordinates $\mathbf{x} = (x, y)$. Additionally, in the same figure, on the left, the correspondent standard element with coordinates $\boldsymbol{\xi} = (\eta, \xi)$ it is represented.

The relation between those coordinates, equation (2.45) is also recalled for convenience:

$$\mathbf{x}(\boldsymbol{\xi}) = \sum_{I=1}^{n_{node}} N_I(\boldsymbol{\xi})\mathbf{x}^I, \tag{4.3}$$

where $\mathbf{x}^I$ are the coordinates of node I. The function $\mathbf{x}(\boldsymbol{\xi})$ from the expression (4.3), relates local coordinates $\boldsymbol{\xi}$ with general coordinates $\mathbf{x}$.

Once the (4.3) is inverted, the local coordinates of the projected virtual node can be computed with $\boldsymbol{\xi_i^v} = \mathbf{x}^{-1}(x_i^v)$. This calculation can be performed analytically, in case of simple shape functions, or numerically, using for instance the Newton-Raphson method. Once the local coordinates of the virtual node are known, the expression (4.4) , can be employed to determine the interpolated d.o.f.

$$v_i = \mathbf{u}(\boldsymbol{\xi_i^v}) = \sum_{j=1}^{n_{node}} N_j(\boldsymbol{\xi_i^v}) u_j \tag{4.4}$$

From this expression results that the weighting coefficients from the expression (4.2) are given by:

$$a_{ij} = N_j(\boldsymbol{\xi_i^v}) \tag{4.5}$$

In summary, for each node on the slave surface, determine their projection (virtual node) and repeat the following steps:

- find the face (3D RVE) or the edge (2D RVE) of the element in the mesh which encloses that virtual node;
- find the face (3D RVE) or the edge (2D RVE) of the element in the mesh which encloses that virtual node;
- for that element face (or edge), determine the nodes and the shape functions associated to that geometry feature;
- compute $\boldsymbol{\xi_i^v}$ solving the system (4.3) to $\boldsymbol{\xi}$;
- compute a_{ij} using (4.5);
- in the b.c. ((3.23) for instance) replace the d.o.f v_i of the virtual node by the linear combination (4.2).

Generate an auxiliary mesh

Another possibility to determine the interpolation weights a_{ij} of the expression (4.2) is using a simple mesh. The Delaunay triangulation, for instance, allows the decomposition of the plane into a mesh of non-coincident triangles (see [31] for details).

After the decomposition, a field u into each triangle can be described by a plane with the equation:

$$u(x, y) = Ax + By + C. \tag{4.6}$$

Where A, B and C, are constants of interpolation. Alternatively, the relation can take the form of:

$$u = \mathbf{x}^{*T}\mathbf{c}^{*}. \tag{4.7}$$

With $\mathbf{x}^{*} = [x, y, 1]^{T}$ and $\mathbf{c}^{*} = [A, B, C]^{T}$. Since the interpolated values on the nodes should return the value of the nodes, it must be possible to write:

$$\begin{bmatrix} u_1 \\ u_2 \\ u_3 \end{bmatrix} = \begin{bmatrix} x_1 & y_1 & 1 \\ x_2 & y_2 & 1 \\ x_3 & y_3 & 1 \end{bmatrix} \begin{bmatrix} A \\ B \\ C \end{bmatrix} \tag{4.8}$$

If $\mathbf{u}^{*} = [u_1, u_2, u_3]^{T}$ and

$$\mathbf{M} = \begin{bmatrix} x_1 & y_1 & 1 \\ x_2 & y_2 & 1 \\ x_3 & y_3 & 1 \end{bmatrix}. \tag{4.9}$$

It is possible to (4.8) write in a more compact form as follows:

$$\mathbf{u}^{*} = \mathbf{M}.\mathbf{c}^{*}. \tag{4.10}$$

That it is equivalent to:

$$\mathbf{c}^{*} = \mathbf{M}^{-1}.\mathbf{u}^{*}. \tag{4.11}$$

Now, substituting $\mathbf{c}^{*}$ from (4.11) in (4.7) it is possible to write the following expression:

$$u = \mathbf{x}^{*T}.(\mathbf{M}^{-1}.\mathbf{u}^{*}). \tag{4.12}$$

The previous expression can be rearranged, so that u can be expressed as a linear combination on $\mathbf{u}^{*}$, as follows:

$$u = \mathbf{u}^{*T}.(\mathbf{M}^{-T}.\mathbf{x}^{*}). \tag{4.13}$$

This expression can be related with (4.2), if $u = v_i$ the interpolated value of the virtual node, and $\mathbf{u}^{*T}$ is a vector with the components equal to the nodal values u_i. Then a_{ij} is given by:

$$\mathbf{a^{i}} = \mathbf{M}^{-T}.\mathbf{x}^{*}_{\mathbf{i}}, \tag{4.14}$$

$$a_{ij} = \mathbf{a^i}_j. \tag{4.15}$$

With

$$\mathbf{x_i^*} = [x_i, y_i, 1]^T. \tag{4.16}$$

Where x_i, y_i are the projected coordinates of the virtual node i.

In summary, this procedure can be described as follows:

- use Delaunay triangulation to generate a mesh of triangles in the slave surface;
- project each node on the master surface to determine a virtual node in the slave surface;
- for each virtual node i determine the matching triangular element in the generated mesh and:

  compute $\mathbf{x}^*$, and $\mathbf{M}$ using (4.16) and (4.9);

  compute $\mathbf{a^i}$ and a_{ij} using (4.14) and (4.15);

  in the b.c. ((3.23) for instance) replace the d.o.f v_i of the virtual node by the linear combination (4.2).

4.3 Data structures for matrix storage

Due to its complex morphology, some materials require relatively detailed meshes for an accurate description. Besides, to guarantee that the behavior of the RVE statistically corresponds to the real material (with negligible fluctuations), it is necessary to choose an appropriate size for the RVE (according to the works [32] and [13]) on the RVE size). Hence, the accurate RVE FEM model, could demand a relatively large number of elements and, consequently, nodes and d.o.f. This requirement implies the need to handle a stiffness matrix with the size of the number of d.o.f squared or an equivalent data structure. Since the matrix is sparse, i.e. most of the elements of the stiffness matrix are null, it is possible not to store most of the null elements in the matrix. This approach requires less operating memory than the storage of full matrix, enabling the solution of problems with more d.o.f. However, there is one major drawback on this strategy: the process to access the stored elements of the stiffness matrix may adversely reduce the computation speed. In the following subsections, two alternative methods to store and access the stiffness matrix are described.

4.3.1 Store the non-null elements in a vector with their indices and values

One of the simplest forms of storing the non-null elements of a sparse matrix $\mathbf{A}$, is to use three simple vectors $\mathbf{i}$, $\mathbf{j}$, $\mathbf{z}$, with the dimension n corresponding to the number of non-null elements of the sparse matrix. Each position of the vector $\mathbf{i}$ is used to store the line, $\mathbf{j}$ the column, and $\mathbf{z}$ of a the non-null-element, so that all non-null elements are stored. For instance, the matrix $\mathbf{A}$ from Table 4.1, can be stored using the vectors $\mathbf{i}$, $\mathbf{j}$ and $\mathbf{z}$, as defined in Table 4.2.

TABLE 4.1: Example of a matrix $\mathbf{A}$ to be stored.

index	1	2	3
1	1.3		-0.5
2	-8.9	1.9	
3			0.9

TABLE 4.2: Vectors defining the matrix $\mathbf{A}$ from the Table 4.1

i	**j**	**z**
1	1	1.3
1	3	-0.5
2	1	-8.9
2	2	1.9
3	3	0.9

In this way, expression (4.17) must hold.

$$\forall A_{ij} \neq 0 \quad \exists_1 k \in [1..n] \; : \; \mathbf{i}_k = i \; \wedge \; \mathbf{j}_k = j \; \wedge \; \mathbf{z}_k = A_{ij}. \tag{4.17}$$

To access a given element A_{ij} locate k that fulfills the previous condition, if k exists access to $\mathbf{z}_k$ otherwise that value is $A_{ij} = 0$. This strategy allows at the same time to save $\mathbf{A}$ in a very compact format. Furthermore, some operations with the matrix can be performed more efficiently. For instance, as the matrix vector product $\mathbf{A}.\mathbf{x} = \mathbf{y}$ can be computed considering:

$$\mathbf{y} = \sum_{k}^{n} \mathbf{z}_k.\mathbf{x}_{\mathbf{j}_k}.\mathbf{e}_{\mathbf{i_k}} \tag{4.18}$$

The symbol $\mathbf{e_i}$ is a unitary vector, with $\mathbf{e}_{\mathbf{i}j} = \delta_{ij} = \{1 \text{ if } i = j \; ; \; 0 \text{ if } i \neq j\}$, used here to represent the *assemblage* process of the vector $\mathbf{y}$. In spite of this simple type structure

for **A** hold the mentioned advantage, it is also important to consider the following disadvantages:

- the random access of a specific element A_{ij} requires a time consuming search operation;
- delete or introduce non-null elements on the matrix **A** may imply to rebuild the data structure.

These disadvantages are especially limitative if the matrix it is used to define a general linear system $\mathbf{A}.\mathbf{x} = \mathbf{b}$, that need to be rearranged to introduce linear constraints. Those constrains can be for instance:

- boundary conditions on the discretized initial value problem (as described on section 3.3);
- relations between d.o.f. given by interpolation (as described on section 4.2.1).

In general, the mentioned operations require a rebuild of the data structure.

4.3.2 Use of hash tables to store and access the non-null components

An alternative, structure and correspondent process to access and handle the sparse matrix of the coefficients involving the use of hash tables is described forward. This approach guarantees a fast access to the elements of the matrix with no search, or just a small search within relatively small sets, despite requiring more operational memory than the sequential storage of non-null elements, as previously mentioned. The class of data structure used is called *hash table* and a description of this structure can be found on [33](chapter 11), [34](chapter 6) and [35](chapter 5). In this section, a brief description of the standard *hash tables* is provided, and then adaptations of the standard *hash tables* are described. Those adaptations, take into account the specific purpose of store and operate with the coefficient matrix in the context of the multi-scale algorithm.

Hash tables

The *hash table* is a very common type of data structure, which can be used to store and fast access to sets of data that cannot be organized in a sequential manner using indices (or there are inconvenient reasons to do it). In spite of that, each member of the data set has a different key value **K** allowing to identify and distinguish it from the others. Depending on the set of data, the key could be for example: a name, an address, a product number, an identification number, etc. Briefly, a standard hash table is composed by three identities:

- vector (or array) $\mathbf{V}$;
- *hash function* ψ;
- *collision* resolution method.

The vector $\mathbf{V}$ is used to store the elements of the data set in a sparse manner. Consequently, $\mathbf{V}$ must be larger than the maximum number of elements to store. The hash function ψ, is a function of the key values $\psi = \psi(\mathbf{K})$ that returns a position on $\mathbf{V}$. This way, ψ creates an association between $\mathbf{K}$ and a position on $\mathbf{V}$ in a deterministic manner, i.e. the result of this function is always the same for the same value $\mathbf{K}$. However, in general, the function ψ is chosen to be "chaotic" and difficult to "predict" in the sense that, it may be used to substitute the generation of uniformly distributed random numbers in certain contexts. Because of that fact, sometimes ψ is categorized as a *pseudo-random generator*, in spite of being deterministic. The main idea is to have a function that tends to distribute the data uniformly. Nevertheless, an element with the key $\mathbf{K}$ is simply accessed in a direct manner with $\mathbf{V}(\psi(\mathbf{K}))$.
Note that, in some cases, the hash function can return the same value for two different keys, this is $\mathbf{K_1} \neq \mathbf{K_2}$ but $\psi(\mathbf{K_1}) = \psi(\mathbf{K_2})$. Such cases are called *collisions* and represent a problem, since two blocks of data cannot be stored directly in the same position of $\mathbf{V}$. A good hash function tends to generate a more or less uniform spread of the data in the sparse vector, in order to minimize the frequency of *collisions*. Furthermore, the number of *collisions* tends to decrease as the ratio between the total size of $\mathbf{V}$ and the size of the data set to store increases. Nevertheless, a method to resolve this *collision*, avoiding the problem of saving the data in the same position of V, is required. Among other possibilities, two *collision* resolution methods are:

- use the positions of $\mathbf{V}$ to store references to other smaller data structures that can hold the data in collision;
- save the data in the next consecutive empty position.

In this last case, a small search is required to access the data when successive positions of $\mathbf{V}$ are occupied. Note that, special cases allow the definition of a *prefect hash function*, which is an injective function that never generates *colisions*. Additionally, to this condition, if the number of elements to store coincides with the range of values of the function, the function is called *minimal prefect hash function*, because it optimizes the space required for the storage vector.

4.3.3 Application of hash tables to store the stiffness matrix

As mentioned early, the hash tables can be used to store a large sparse matrix $\mathbf{A}$, while simultaneously providing fast access to its members. However, this option requires less operating memory than the storage of the raw matrix. The main idea is to consider a sparse vector $\mathbf{V}$ that will hold the non-null elements of the matrix and use a hash function $\psi(\mathbf{K}) = \psi(\{i, j\}) = k$ to establish the correspondence between A_{ij} and V_k.
The stiffness matrix to store, has characteristics that can be considered for a better performance:

- full occupation of the main diagonal;
- very high occupation of the main diagonals (diagonals near to the main diagonal);
- in general the non-null members are symmetrically distributed
  (if $A_{ij} \neq 0$ then $A_{ji} \neq 0$).

Therefore, it is very convenient to fully store all the items in the central diagonals in a vector with direct access, separately form the remaining part of the matrix. It is also suitable, to save pairs non-null members of the matrix A_{ij} and A_{ji} together in the hash table, given the symmetry of their positions. Those two, strategies reduce the amount of required memory and the tendency for *colisions*.

Storage of the main diagonals

Given a sparse distributed matrix $\mathbf{A}$ with dimensions $n.n$, with very high occupation rate among the elements in the central diagonals, let us consider the main diagonal and $(\delta - 1)^{th}$ immediately upper and lower diagonals. Then the elements in the diagonals can be stored in an array $\bar{\mathbf{V}}$ with size $[n \times \delta \times 2]$. The first and second index of $\bar{\mathbf{V}}$ are associated with both the column and the line, while the third index indicates whether or not the element belongs to the upper or lower part of the matrix. Notice that, a small part of the array is not used, however the correspondent memory is negligible and therefore the used method provides a very direct and simple access to the elements.

Storage of the sparse elements outside of the main diagonals

Outside of the main diagonals, the elements of the matrix are considered to be distributed and stored in a sparse manner on the storage vector. For this purpose a *pseudo random hash function* is used, in order to distribute the elements as described in the section 4.3.2. Because this class of hash functions has many applications has been the

subject of study in many papers. Most of those functions have as input a single integer number, which provides a certain standardization. Since in this application the keys contain two numbers corresponding to the position (i, j) in the matrix, a process called *preconditioning* is used to convert the key in a single integer number k. The *preconditioning* performed in this application is given by:

$$k = k(i,j) = i + (j-\delta)(j-\delta-1)/2 \mid i \in \{1, ..., n-\delta\} \wedge j \in \{i+\delta, ..., n\}. \quad (4.19)$$

Essentially the function k, provides a "sort order" number for the elements (i, j) , which results in an injective function, where $k(i_1, j_1) \neq k(i_2, j_2)$ for any two different pairs $(i_1, j_1) \neq (i_2, j_2)$ within the domain of the function.

For the hash function two different methods described in [34] have been tested considering this specific application, then the best method was chosen, i.e. the one that generated less *conflicts*. As it will be described forward, both of the methods fulfill this requirement in a "fairly" acceptable manner, for this application. However, we assume the possibility of the existence of other methods that provide better results. The two methods considered are:

- the division method;
- the midsquare method.

The division method is one of the most widely accepted and defined as:

$$\psi(k) = k \bmod m + 1. \quad (4.20)$$

Where ψ is the pseudo random number generated, m is some integer divisor. The operator mod returns the remaining value from the integer division between k and m. Notice that the division method produces a value for ψ in the range $\psi \in \{1, ..., m\}$. In order to obtain good properties for the hash function the number m should be ideally a large prime number, according to [34] and [35]. However, since m conditions the size of the storage vector, in the practice it is also acceptable to use $m = 2^x - 1 | x \in \mathbb{N}$, according to [35]. Then x can be approximated with:

$$x \approx \text{integer}\left(\frac{log\, m_0}{log\, 2}\right), \quad (4.21)$$

here m_0 is an approximate value for the size of the storage vector.

Another possibility is the use of the midsquare method, widely used with success in many applications according to [34]. In this method, the key is firstly multiplied by itself. Then, a certain number of digits from the middle of this result are chosen (depending on the table size) to form the result of the function, in a reverse order ([34]). For example, the key number $k = 52532$, results in the squared value $k^2 = 2759611024$, then the numbers 9611 are extracted from the middle and, finally, reversed; hence: $\psi(52532) = 1169$.

Numerical tests on the hash function performance

Numerical experiments were conducted, in order to determine which of the described hash functions can produce a better performance, accordingly to the aim of this application, i.e. which of the functions produces the more uniform scatter of the data in the storage vector and, consequently, presents less tendency to *collisions*. Considering the data to store $\mathbf{D}$, the upper part of the matrix $\mathbf{A}$, and excluding, the main diagonal and the next $(\delta - 1)^{th}$ upper diagonals, the test data have been generated in the following conditions:

- matrix $\mathbf{A}$ with size $[10000 \times 10000]$;
- parameter $\delta = 24$;
- number of elements in the sparse matrix given by $n_e = x$;
- $0.3n_e$ elements in blocks 9x9 distributed randomly;
- $0.3n_e$ elements in blocks 3x3 distributed randomly;
- $0.4n_e$ elements distributed randomly without considering blocks;

Hence, the number of elements to store in the sparse vector was around $n_v = 38000$. The performance of each of the methods to distribute the data in storage vectors with different size b, was evaluated. For this, different load factors $\alpha = b/n_v$ the maximum number of elements $maxELEM$ to store in the same position of $\mathbf{V}$ was determined. The variable $nUNIQUES$, corresponding to the number of positions from $\mathbf{V}$ occupied by a single element, was also determined. A synthesis of the results obtained is presented in Table 4.3.

The presented table shows that booth methods have an acceptable performance. A loading factor around $\alpha = 13.8$ conducts to a maximum number of elements to store in the same position of 4, besides a considerable fraction of the elements are stored in empty positions. Nevertheless, the division method tends to lead to less collisions and

TABLE 4.3: Comparison of methods used to distribute the values in the hash table.

		Division method		**Midsquare method**	
b	$\alpha = b/n_v$	$maxELEM$	$nUNIQUES$	$maxELEM$	$nUNIQUES$
1.05E+06	27.60	1	37985	3	36500
5.24E+05	13.80	1	37985	4	35220
2.62E+05	6.90	1	37985	5	33302
1.31E+05	3.45	1	37985	6	28350
6.55E+04	1.73	2	33107	6	21711
3.28E+04	0.86	3	16724	7	12575
1.64E+04	0.43	6	2946	11	3766

more elements placed in a single position of **V**. Therefore, the division method was considered to be better distributing the elements in **V**.

Strategy for collision resolution

As stated before, many strategies are presented in the literature to resolve the *colisions*, i.e. to avoid the problems created when more than one position of the storage vector is associated to different keys. A possible strategy to resolve the *collisions* is to associate a data set that can contain zero, one or multiple elements of data. This data set should be able to expand or contract dynamically. A commonly used structure with that characteristics called *linked list* was employed. In order to provide a general insight of the implementation efficiency, a very general description of this structure is given. However, for a detailed description on *linked lists*, their variations and performance, refer to [34] or [33] for instance. Furthermore, this data structure is usually provided with the standard libraries of many programming languages. A schematic representation of the linked list used is represented in Figure 4.1.

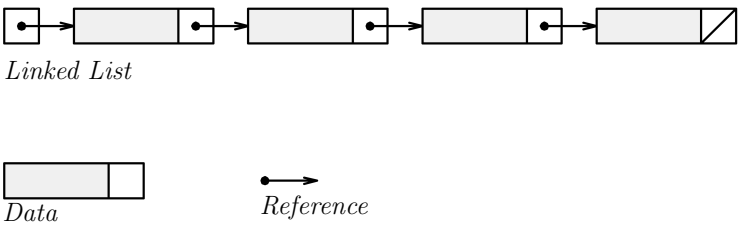

FIGURE 4.1: Schematic representation of the linked list and its constituents.

The data structure is composed by a set of items. Each of the items contains the data to store, and a memory reference. The memory reference (or pointier), existing in each item, provides access to another item, with exception of one *last* item in the chain, that does not refer to any item. This way, all the items are connected in a consistent

chain. This structure allows to insert and remove items with minimum computations, simply redirecting references. One of the main draw backs, however, is the time required to search for a given item, that may require the sequential access to other items. Nonetheless, in this context the maximum number of items to store, corresponding to the maximum number of *colissions* in the hash table, can be relatively small, as shown in Table 4.3. Hence, the the search is very efficient.

Overview of the data structure for the stiffness matrix

In order to summarize the overall procedures for data structure used to keep the stiffness matrix, this section presents the algorithms indicated from Tables 4.4 to 4.8. Those algorithms, can be used for the main operations involving the matrix $\mathbf{A}$. Those operations include: initialization, evaluating the hash function, accessing to A_{ij} value, setting the value of an element A_{ij} and deleting a given value. As previously described, the symmetric positioned values A_{ij} and A_{ij}, are stored together in the hash table. A temporary variable $u = 1$, meaning that A_{ij} belongs to the lower part of the matrix, while $u = 2$, means that A_{ij} belongs to the upper part. Two different types of arrays are used to store the hash table $\bar{\mathbf{V}}$ and $\mathbf{V}$. The array $\bar{\mathbf{V}}$ is used to store all the elements of the main diagonals of $\mathbf{A}$, (including zeros), in a sequential form directly in the array, since this part of the matrix tends to be dense as already explained, while the array $\mathbf{V}$, is used to store the remaining part of the matrix $\mathbf{A}$ in a sparse manner. This way, the sparse array $\mathbf{V}$ is used to store references destined to contain elements outside the main diagonals of $\mathbf{A}$ and not stored in $\bar{\mathbf{V}}$. The *linked lists* structures are used in this process, in order to avoid possible *colisions*. Since $\mathbf{V}$ is sparse, a large fraction of the references are null. Nevertheless, the connection between the indices in $\mathbf{A}$ and the positions in $\mathbf{V}$ is done using a *hash function* that can seldom generate *colisons*. Consequently, most part of the references of $\mathbf{V}$ are either null or conduct to the lists containing only a single element A_{ij} or a substantially reduced number of elements in collision.

4.4 The method GMRES for iterative solution of unsymmetrical systems

As previously stated, the aim of addressing realistic materials with a complex microstructure in general requires, the use of large and detailed RVEs, in order to ensure a representative behavior. This can be achieved using a large and refined mesh, that conducts to large amount of nodes and d.o.f. Therefore, it is important to ensure that the consumption of computational memory is optimized. At this point, the use of a numerical

TABLE 4.4: Initialization of the internal data in the hash table.

(1) Set n the size of matrix $\mathbf{A}$ to store;

(2) Set δ the number of upper main diagonals to store separately;

(3) Set $n_v \approx 20 * n$ the approximate number of non null elements in the upper matrix;

(4) Set α the load factor for the sparse part of the hash table;

(5) Compute $m_2 \leftarrow 1 + \delta(n-1)$ length to allocate to store the main diagonals;

(6) Compute $m_0 \leftarrow \alpha * n_v$;

(7) Determine the integer $x \leftarrow \text{integer}(log(m_0)/log(2))$;

(8) Determine $m \leftarrow 2^x - 1$ to be the size of the vector to store the sparse part of $\mathbf{A}$;

(9) Initialize $\bar{\mathbf{V}}$ with size $[n \times \delta \times 2]$, with zeros (for the main diagonals);

(10) Initialize $\mathbf{V}$ with size $[m]$, with *null references*(for the sparse elements outside the diagonals).

iterative scheme to solve the discretized problem may be an advantage, since it does not require operating transformations on the matrix of the coefficients, which is in general very costly in terms of memory and time. Furthermore, the iterative methods usually allow the use of computations in parallel if required. There are several iterative schemes that can be used, for instance the classical Successive Over-relaxation (SOR), Steepest Descendent, Conjugate Gradient (CG), Pre-conditioned Conjugate Gradient (PCG); among others see for instance [36]. The Generalized Minimal Residual Method (GMRES) have the advantage of allowing not only the solution of unsymmetrical systems, but also updating the approximate solution with a relatively reduced amount of memory and computational time. Nevertheless, this method was chosen to provide an example of an efficient interactive method for this overall strategy. In fact, no tests have been performed to choose this method rather than others and a future exhaustive bibliographic research for better methods is recommended. For this reason it is assumed the possible existence of other different interactive methods that can perform better.

This GMRES method [37] can be used for Solving Nonsymmetric or Symetrical Linear Systems and is based on Arnoldi's method, for matrix factorization regarding the Krylov subspace. For a detailed description on this subject, refer to [37] and [36].

TABLE 4.5: Method for determine the position of the element A_{ij}.

(1) Determine if the element (i, j) belongs to the upper or lower part of $\mathbf{A}$.
if $i \geq j$ **then**
  $u \leftarrow 2$ (upper part of $\mathbf{A}$)
else
  $u \leftarrow 1$ (lower part of $\mathbf{A}$)
  $t \leftarrow i$; $i \leftarrow j$; $j \leftarrow t$
end if

(2) Verify if (i, j) belongs to the main diagonals and evaluate the hash function.
if $|i - j| < \delta$ **then**
  $v \leftarrow 1$ (associated with $\bar{\mathbf{V}}$)
  $k \leftarrow j - i + 1$ (2^{nd} index of $\bar{\mathbf{V}}$)
else
  $v \leftarrow 0$ (associated with$\mathbf{V}$)
  $k \leftarrow i + (j - \delta)(j - \delta - 1)/2$
  $k \leftarrow k \bmod m + 1$
end if

(3) Return u,v and k.

4.5 Overall algorithm

Table 4.9 presents an overview of the improved multi-scale algorithm for three dimensional RVEs.

4.6 Validation of the Algorithm

In this section, two applications for the described algorithm are presented in order to verify the quality of the results obtained and to analyze the convergence rate.

4.6.1 Homogenized stress of an alloy with voids using linear and periodic boundary conditions

In this example, the described algorithm is used to obtain the homogenized stresses considering the linear and periodic boundary conditions, and using a distortional deformation gradient. The results are then compared.

TABLE 4.6: Method for obtain the element A_{ij} from $\mathbf{A}$.

(1) Determine the flags u, v and the position k in the hash table using the algorithm described in Table 4.5.

(2) Obtain the value A_{ij}
if $v = 1$ **then**
  $A_{ij} \leftarrow \bar{\mathbf{V}}_{i,k,u}$
else
  Obtain the reference $R \leftarrow \mathbf{V}_k$
  if $R = null$ **then**
    $A_{ij} \leftarrow 0$
  else
    Locate and get A_{ij} from the linked list referenced with R
    if A_{ij} was not found **then**
      $A_{ij} \leftarrow 0$
    end if
  end if
end if

Therefore, considering the plane strain state, a square RVE of a fictitious alloy with void inclusions, represented on Figure 4.2, was considered.

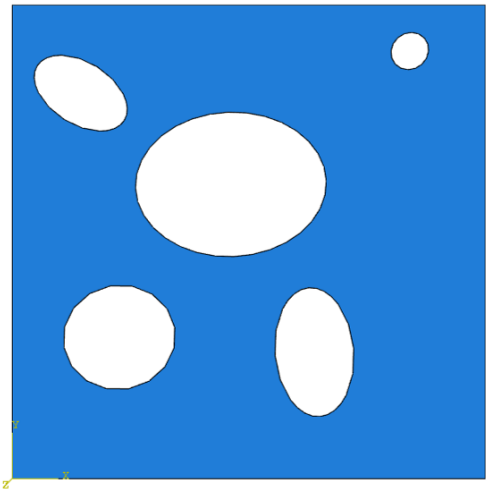

FIGURE 4.2: Geometry of the RVE considered (plane strain assumed).

The RVE has 0.100 mm on the edge and is composed by linear elastic material, with Young modulus $E = 200$ GPa and poison ratio $\nu = 0.3$. To control the errors induced by the discretization, four types of FEM mesh were considered. Those meshes, are composed by triangular and quadrilateral isoparametric elements with three and four

TABLE 4.7: Method for remove a element A_{ij} from $\mathbf{A}$.

(1) Determine the flags u, v and the position k in the hash table using the algorithm described in the Table 4.5.

(2) Remove the values A_{ij} and A_{ji}
if $v = 1$ **then**
  $\bar{\mathbf{V}}_{i,k,1} \leftarrow 0$
  $\bar{\mathbf{V}}_{i,k,2} \leftarrow 0$
else
  Obtain the reference $R \leftarrow \mathbf{V}_k$
  if $R \neq null$ **then**
    Obtain the reference $R = \mathbf{V}_k$
    if A_{ij} exists in the linked list **then**
      Remove A_{ij} and A_{ji} from the linked list
      if linked list empty **then**
        Delete linked the list
        $\mathbf{V}_k \leftarrow 0$
      end if
    end if
  end if
end if

nodes respectively. The number of nodes and elements used for each mesh is given in Table 4.10.

The discretized models of the RVE were subjected to a pure distortive deformation under the linear and periodic boundary conditions. The considered deformation gradient $\mathbf{F}$ was the following:

$$\mathbf{F} = \begin{bmatrix} 1.00 & 0.01 \\ 0.01 & 1.00 \end{bmatrix}.$$

The computed, shear components P_{12} of the homogenized First Piolla-Kirchhoff stress, regarding the different combinations of boundary conditions and meshes, are compared in Table 4.11, where the values are given in MPa. In Table 4.11 a relative error, is also presented, considering the most refined calculation as exact.

A comparison of the First Piolla-Kirchhoff stress component P_{11}, regarding the different assumptions mentioned is also given in Table 4.12, the values are given in MPa. The computed, stress component P_{11} of the homogenized First Piolla-Kirchhoff stress, regarding the different combinations of boundary conditions and meshes, are compared in

TABLE 4.8: Set the value of the element A_{ij} from $\mathbf{A}$.

(1) Determine the flags u, v and the position k in the hash table using the algorithm described in the Table 4.5.

(2) Set the value for A_{ij}
if $v = 1$ **then**
  $\bar{\mathbf{V}}_{i,k,u} \leftarrow A_{ij}$
else
  Obtain the reference $R \leftarrow \mathbf{V}_k$
  if $R = null$ **then**
    Initialize a linked list and obtain the reference R
    Set $\mathbf{V}_k \leftarrow R$
    Add A_{ij} to the linked list
  else
    if A_{ij} exists in the linked list **then**
      Set A_{ij} in the linked list
    else
      Add A_{ij} to the linked list
    end if
  end if
end if

Table 4.12, where the values are presented in MPa. Again in Table 4.12 a relative error is presented, considering the most refined calculation as exact.

The distribution within the RVE of component P_{12} for the most refined mesh is described according to the plot of the Figure 4.3 for the linear boundary condition, and according to the Figure 4.4 for the periodic boundary condition.

The homogenized First Piolla-Kirchhoff stress tensor in MPa, obtained for the linear boundary condition, was the following:

$$\mathbf{P} = \begin{bmatrix} -74.15 & 852.67 & 0.00 \\ 852.34 & -40.70 & 0.00 \\ 0.00 & 0.00 & -24.45 \end{bmatrix} \text{MPa}.$$

While, for the periodic boundary condition, the homogenized First Piolla-Kirchhoff stress tensor was the following:

TABLE 4.9: Overall homogenization algorithm

(1) Given:

- Geometric definition of the RVE;
- Constitutive model of the different phases;
- Deformation gradient $\mathbf{F} = d\mathbf{x}/d\mathbf{X}$;

(2) Generate FEM mesh for the RVE;

(3) Determine opposed edges or faces, and set-up master and slave pairs;

(4) Compute interpolation coefficients for the master and slave pairs of dof;

(5) Generate a discrete version of the boundary conditions, regarding the FEM mesh, the master slave pairs and the interpolation coefficients;

(6) Under the standard FEM framework, produce a discrete linear version of the virtual work equation;

(7) Substitute the discrete b.c. in the virtual work equation using the hash table framework;

(8) Solve the virtual work equation using the Newton-Raphson method in combination with the GMRES solver;

(9) Computation of average quantities.

TABLE 4.10: Number of nodes and elements for the different meshes.

		Elements	
	Nodes	Quadrilateral	Triangular
MESH0	252	197	10
MESH1	697	594	28
MESH2	1161	1025	35
MESH3	2461	2242	78

TABLE 4.11: Homogenized shear component P_{12} (MPa) for different assumptions.

	Linear B.C.	Error(%)	Periodic B.C.	Error(%)
MESH0	995.75	6.80	928.40	8.88
MESH1	953.66	2.29	876.81	2.83
MESH2	941.41	0.97	862.70	1.18
MESH3	932.35	0.00	852.67	0.00

TABLE 4.12: Homogenized stress component P_{11} (MPa) for different assumptions.

	Linear B.C.	Error(%)	Periodic B.C.	Error(%)
	-65.51	5.95	-68.07	8.21
MESH1	-68.15	2.16	-72.10	2.76
MESH2	-68.87	1.13	-72.70	1.95
MESH3	-69.65	0.00	-74.15	0.00

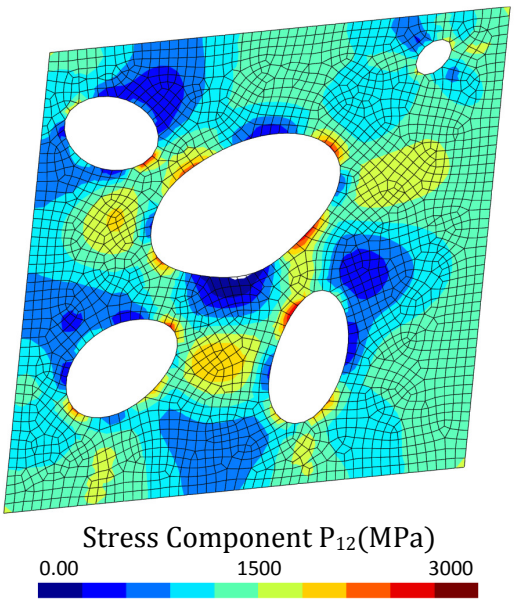

FIGURE 4.3: Contour of the shear stress component P_{12} using the linear B.C.

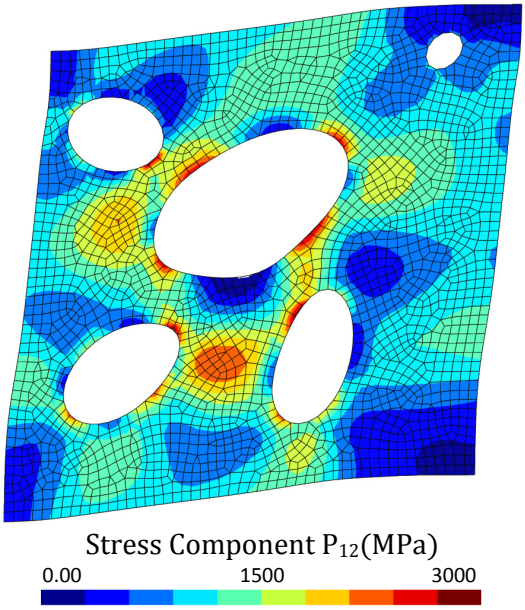

FIGURE 4.4: Contour of the shear stress component P_{12} using the periodic B.C.

$$\mathbf{P} = \begin{bmatrix} -69.65 & 932.35 & 0.00 \\ 932.14 & -48.57 & 0.00 \\ 0.00 & 0.00 & -24.90 \end{bmatrix} \text{ MPa.}$$

It is possible to verify that the homogenized shear stress obtained for the linear boundary condition is around 10% larger when compared with the same stress component that is obtained for the periodic boundary condition. This fact is in agreement with the literature [38], [39], [40] and it is due to the fact that the linear boundary condition is more 'restrictive', in a kinematic sense, than the periodic boundary condition. This can be confirmed by the deformed configurations, of Figures 4.3 and 4.4. The periodic condition is less restrictive which results in less stiffness and less accumulation of stress over the RVE. Also, according to the literature, the homogenization tends for the same results using different boundary conditions as the size of the RVE increases.

Given the presented results, it is also possible to verify that, the stress tensors obtained for both of the boundary conditions tends to converge for stable values as the mesh refinement increases. The convergence rate of the homogenized stress, as the mesh becomes more refined, is apparently similar in both cases. Since this rate was the same and the use of periodic B.C. requires interpolation of d.o.f., in opposition to the linear B.C. Therefore, the use of interpolation does not adversely affect the quality of the results in this example.

4.6.2 Effects of the interpolation of degrees of freedom strategy

In this section, a numerical test is described. This test was performed with the aim of determining the interpolation of degrees of freedom effects on two variables: the computed homogenized stress and the convergence rate of the algorithm.

A representative volume element, RVE of an alloy with a cubic hole at the center, was modeled. The constitutive behavior of the alloy was idealized according to the classical elasto-plastic model of von Misses (see [17] for details on this model). The parameters for the material were defined according Table 4.13.

TABLE 4.13: Mechanical properties of the alloy [41].

E	ν	σ_{y0}	σ_y
72.4 GPa	0.33	352 MPa	$352 + 853\bar{\varepsilon}_p$ MPa

The geometry of the RVE is characterized by a cube with an edge of 100 mm and a cubic void, which is centered, with 33.33 mm of edge. For the discretization of the RVE, two

types of finite element mesh were considered: MESH1 and MESH2. MESH1 is the periodic mesh with 2170 nodes and 1664 (isoparametric, hexahedral) elements, represented in Figure 4.5, MESH2 is the non-periodic mesh with 4860 nodes and 11700 (isoparametric, hexahedral and tetrahedral) elements represented in the Figure 4.6. MESH2 is partially disorganized near to one of the faces, which results in more elements and nodes.

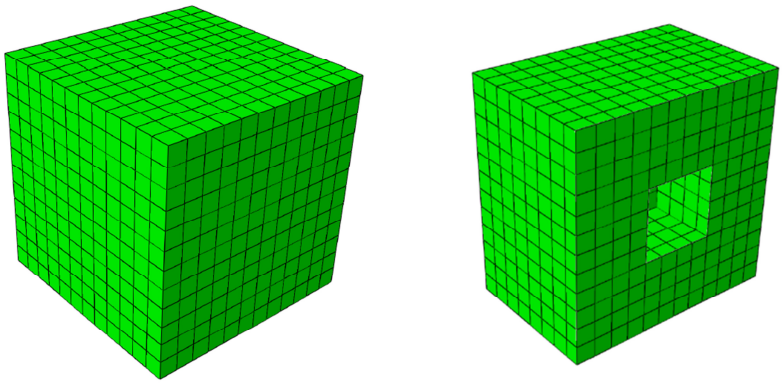

FIGURE 4.5: MESH1 - Periodic mesh for the RVE considered (left: complete RVE, right: half-cut).

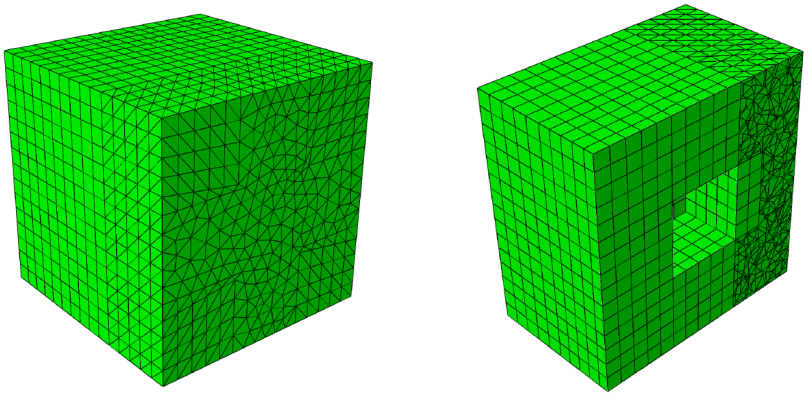

FIGURE 4.6: MESH2 – Non-periodic mesh for the RVE considered (left: complete RVE, right: half-cut).

The goal of using these two types of mesh was obtaining comparable results in equivalent calculations, where the enforcement of boundary conditions was done without and with interpolation. The linear boundary conditions and the periodic boundary conditions were used. The following macroscopic deformation gradient $\mathbf{F}$ was imposed to the RVE:

$$\mathbf{F} = \begin{bmatrix} 1.10 & 0.00 & 0.00 \\ 0.00 & 1.00 & 0.00 \\ 0.00 & 0.00 & 1.00 \end{bmatrix}.$$

The homogenized first First Piolla-Kirchhoff stress tensor was computed for the different configurations of mesh and boundary conditions. The non-null components obtained for this tensor in different conditions are listed in Table 4.14.

TABLE 4.14: First Piolla-Kirchhoff stress tensor (MPa) in different configurations.

	Periodic B.C.		Linear B.C.	
	MESH1	MESH2	MESH1	MESH2
P_{11}	1002.3	1032.7	1152.0	1127.3
P_{22}	934.1	965.5	1115.5	1151.4
P_{33}	934.1	965.5	1115.5	1151.4

In Figure 4.7, half of the RVE trimmed in a parallel direction to the loading is represented. The field represented in the figure, corresponds to the Equivalent Stress obtained under periodic displacements boundary conditions for the MESH1.

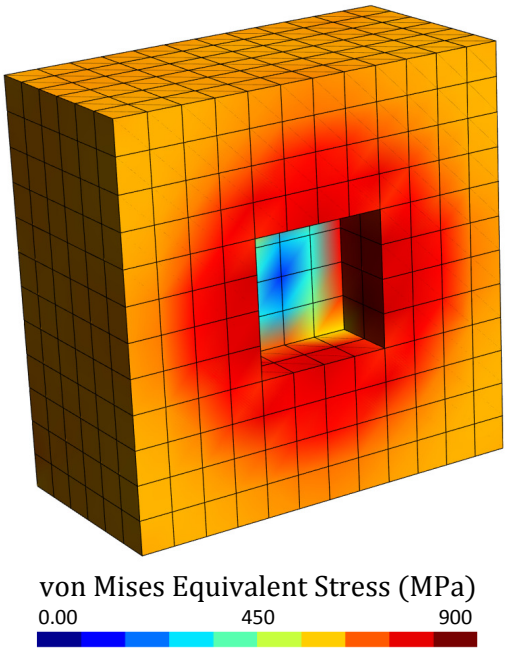

FIGURE 4.7: Equivalent von Mises stress(MPa) on a half-cut of the RVE in the direction of the loading (MESH1 and Periodic B.C.).

This field, among other fields of displacements and obtained stress follows a certain pattern of symmetry in congruency with the loading conditions and the geometry of the RVE. The homogenized macroscopic stress obtained for the linear B.C. is around 15% higher than the computed values for the periodic B.C. This difference, once again, is in agreement with the fact that, in a kinematic sense, the linear boundary condition is more 'restrictive', than the periodic boundary condition. As Table 4.14 shows, the homogenized First Piolla-Kirchhoff stress components, obtained for MESH1 and MESH2, have less than 5% of difference considering the same boundary condition. Regarding

the differences between meshes and the mesh dependency of the plasticity model the result was considered acceptable. This suggests that the interpolation of d.o.f. does not influence in a significant manner the overall stress results.

Convergence rate

The evolution of the relative residual norm $||x_{n-1} - x_n||/||x_n||$ within the iterations using MESH1 and MESH2 is presented in Table 4.15.

TABLE 4.15: Evolution of the relative residual norm.

	Linear B.C.		Periodic B.C.	
Iteration	MESH1	MESH2	MESH1	MESH2
1	1.173E+04	2.147E+04	3.937E+01	3.119E+01
2	1.399E+03	1.050E+03	2.483E+00	5.410E+00
3	1.101E+01	6.701E+00	2.074E-01	4.304E-01
4	9.651E-05	1.770E-04	6.946E-03	6.512E-03
5	1.723E-08	1.612E-08	2.097E-07	1.405E-07

The evolution of the relative residual norm was similar whether using MESH1 or MESH2 for the same boundary condition. In all the cases the convergence rate obtained was quadratic. The use of the non-periodic MESH2 with the periodic B.C. required the use of interpolation of d.o.f. in the faces of the cube. However in this case, the convergence rate was not affected by the use of interpolation.

Chapter 5

Development of an Algorithm to Generate Random RVEs

5.1 Introduction

The endeavor on homogenization research is motivated by a set of parameters, namely the increment of the computational power available, the advances on simulation models, the interest of the industry on improving the reliability of the predictions, not to mention the aim to design tailored materials for specific proposes. As important classes of tailored materials we may identify: (1) dispersed particle microstructures, (2) continuous fibre microstructures, (3) discontinuous fibre, whisker or elongated single crystal microstructures, (4) fabric woven braid microstructures. [42]
Many studies such as [43] and [14] conclude that the generation of representative volume elements (RVE) is an important aspect to take under consideration in the simulations, because it can be a time costly procedure and over simplifications can neglect important phenomena leading to inaccurate results.
However, the generation of representative geometries describing the structure of some materials realistically still remains as an important challenge in spite of the many algorithms and models that have been proposed so far.

5.1.1 Models based in the dispersion of the particles

Models based on the dispersion of particles are very common in applications such as: unidirectional fibre reinforced composites, soils, concrete and other grain materials. It is possible to quote the investigation by [23] as one of the studies using models based on particle dispersion; in fact it describes a multiscale model based on a multilevel finite

element to model the behaviour of the long fibre SiC/Ti composite materials; its real structure is depicted in Figure 2.

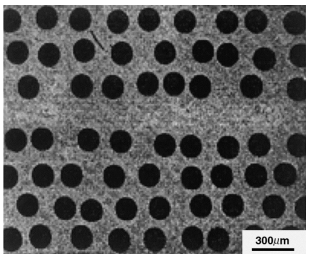

FIGURE 5.1: Periodic microstructure of a SiC/Ti composite [23].

Wongsto[44] conducts a micromechanical finite element analysis of unidirectional fibre reinforced composites, from which a real structure is represented on Figure 5.2.

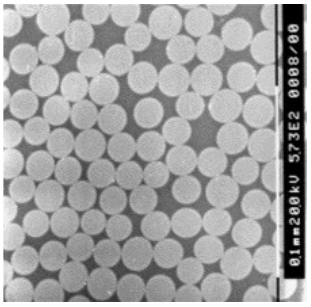

FIGURE 5.2: Random fibre distribution observed from the real composites [44].

Hafner, provides a study [45] on the simulation of concrete behaviour using multiscale techniques. A sample view of the three-dimensional generated model is presented in Figure 5.3.

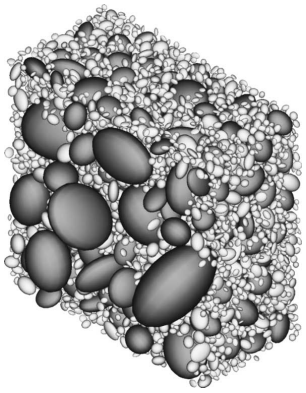

FIGURE 5.3: Section of a three-dimensional geometrical mesoscale model of concrete [45].

A particular case of this class of problems is the generation of RVE, with disks or spherical inclusions (such as the one provided by [44] and [46]).

5.1.2 Problems of packing spheres and disks of the same size

Disks and spheres packing have been a long standing research topic due to its academic and industrial importance[47]. Examples of applications extend from granular processing to fruit packing, adsorption on surfaces and other statistical mechanics problems. In 1611, Kepler was asked: "What is the densest way to stack equal sized cannon balls?"[48]. Later, the classical statistical mechanics of hard-sphere systems generated a large collection of scientific publications, dating back at least to Boltzmann,1898 [48]. Bernal pioneering work[49] on the attempt to model the structure of liquids using random close packing (RCP) initiated a new interest on the studies about the subject. Since then many scientists contributed to the study, definition and application of the sphere packing. However, this subject still remains open to further discussion and investigation.

In fact, Torquato[15] argues that the RCP notion is not well defined mathematically because the terms "random" and "close packed" are at odds with another. Hence, the author argues that the final states of packing are protocol dependent.

As a matter of fact, preparing a representative volume element (RVE) with a considerable amount of circles is not a trivial problem if the applications require a statistically random distribution of circles and a very high level of compaction. The programs used in order to fulfill such requirements can run very slowly. This generally happens because in the conventional algorithms as the number of inclusions N increases more conflicts or interactions must be considered.

5.1.3 Methods for generate models of dispersion of inclusions

Buryachenko in his work[50] divides the dense random packing methods in two types: the sequential generation models and the collective rearrangement models (CRM). Examples of the sequential generation models are the Random Sequential Addition (RSA) methods [51], the cluster growth method [52], and the advance Front Method [47]. For the cluster growth method in particular many variations have been proposed, but it was proved that the process tends to generate inhomogeneous and anisotropic models [53]. Examples of collective rearrangement models (CRM) are the ones based on Discrete Element Method (DEM) (see for instance [54]) and simplifications of it where all the particles of the packing can interact. It is known that, the DEM method generally consumes a substantial computation time, when a large number of particles interact.

5.1.4 Methods for generating models of equal size spheres or disks

Concerning the examples of algorithms able to generate random distributions of spheres and disks of equal size, Jodrey[55] proposed and algorithm for simulation of close random packing of equal spheres. This algorithm is based on the process of compression of a hard-sphere gas and achieves densities ϕ_c between 0.642 and 0.649. However, the algorithm was not statistically analyzed and the authors advise that the distributions obtained in two dimensions may not be random.
Feng, proposed an algorithm [47] based on the advancing front technique, for the generation of distributions of discs in two dimensions. In this method, an initial cluster of particles increases progressively as more particles are added to the front of the cluster. The complexity of the algorithm for generating N disks is in the order of $O(N\sqrt{N})$ [47]. Nonetheless, it is known that this type of method generates inhomogeneous and anisotropic distributions, as explained by the work [53]. No variations of the algorithm for the tridimensional space are proposed and the authors advise about the possibility of the algorithm to generate large gaps of particles in the interior.
Addressing the same subject, Feng and Han[56] proposed a compression algorithm for generating models of spheres in three dimensions. The algorithm can fill any arbitrary polyhedral or cylindrical domain and attain packing densities in the order of $\phi_c = 0.528$. However, the randomness of the distributions was not statistically studied.

Another algorithm proposed by Wongsto [44], generates a distribution of particles starting with a hexagonal periodic distribution. Later analysis [46] suggests that the distributions generated by this method are not completely random.
Melro′s algorithm [46] uses a set of heuristics for compacting an initially random but not packed distribution of particles. The algorithm allows the generation of models with high volume fraction. However, the time used to generate the models increases with the edge size in a geometric rate, besides requiring the calibration of an extensively high number of empirical parameters for the heuristics to work properly on a given RVE size.

5.1.5 Layout

In this Chapter, a new algorithm with linear complexity and able to generate distributions of 2D disks randomly packed is proposed. The algorithm can easily be extended for 3D or other dimension problems. In fact, the algorithm is able to add sequentially new disks in random positions (that do not conduct to over- laps without the existing disks) directly, i.e. without trial and error attempts. To achieve this purpose, a new concept, based on the mapping of the positions available to place new disks with a scalar

value, is developed.
Besides, the algorithm also guarantees the maximum packing possible for a perfectly random distribution. The time used to place any disk is constant during the process. This allows a feasible method for the generation of RVE of any size in a fair amount of time.
The generated models have been statistically analyzed in order to confirm the random state of the distributions. Mechanical simulation tests have also been performed in order to verify the elastic isotropy of the generated models. Finally, a derivation of the algorithm is proposed, allowing to obtain models with higher volume fractions. This derivation considers the idea proposed in [15] sustaining that there is a compromise between randomness and packing. Hence, the higher volume fractions (higher than the ones obtained in the original algorithm) are produced if the random state is reduced by heuristic rules.

5.2 Description of the algorithm

In this section, the proposed algorithm for the generation of highly compact distributions of constant diameter circular inclusions is described. Firstly, the concepts of *Admissible region* and *Free Volume* are defined in subsection 5.2.1. Then a recursive decomposition of the RVE into domains and some related notation are described in the subsection 5.2.2. In the subsection 5.2.3, a function called *Free Volume Function* is defined using the concepts of the previous sections. As forward explained in the section 5.2.4, the *Free Volume Function* plays a very important role in the overall algorithm because it is used to determine available positions to place inclusions. The data structure and the algorithms used as support for the evaluation and updating of the *Free Volume Function* are presented on the subsection 5.2.5. In section 5.2.6, the overall algorithm is presented. In section 5.2.7, a criterion to establish the minimum size of the smaller domains used in the domain decomposition is established and justified. Finally, the advantages and limitations of the method are highlighted in subsection 5.2.8.

5.2.1 Admissible region and Free Volume

The concepts of *Free Volume* and *Admissible Region* are central in this algorithm and are explained below. For any two circular inclusions of the same radius R (Figure 5.4), the minimum distance between centers ensuring that no overlap occurs is $2R$.

Following, if the center position of an inclusion is given, any other inclusion center must be placed in an admissible region exterior to a circle of radius $2R$. For instance,

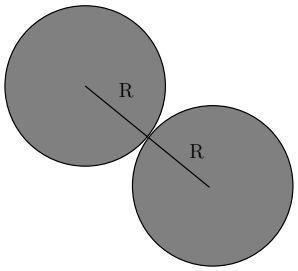

FIGURE 5.4: Two particles close together with the minimum distance of $2R$.

Figure 5.5 represents an inclusion in dark gray and a light gray circle where no inclusion can exist without overlapping.

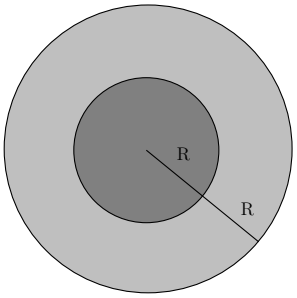

FIGURE 5.5: Region of non-admissible positions around an inclusion (in yellow) where no center of other inclusion can exist without overlapping.

For a given distribution of inclusions on an RVE, the *admissible region* is defined as the region where any point can be the center of a new inclusion to place without overlapping the existing ones. This concept is depicted on Figure 5.6. The *admissible region* is obtained as the remaining part after extracting the circles of radius $2R$ around all the inclusions.

The *admissible region* is mathematically defined by the expression (5.1).

$$\mathbb{A} = \bigcap_{i=1}^{N} \{x \in \mathbb{D} : ||x - x_i|| \geq 2R\} \tag{5.1}$$

Where $\mathbb{A}$ is the admissible region, $\mathbb{D}$ is the domain where the inclusions intend to be distributed, N is the total number of inclusions x_i is the center point a given inclusion, while R is the radius of the inclusions. For a given distribution of inclusions, the concept of *Free Volume* is defined as the area of the admissible region. For instance in Figure 5.6, the *Free Volume* is the area in white. This concept is presented on the expression (5.2).

$$V_{av} = \int_{\mathbb{A}} dx \tag{5.2}$$

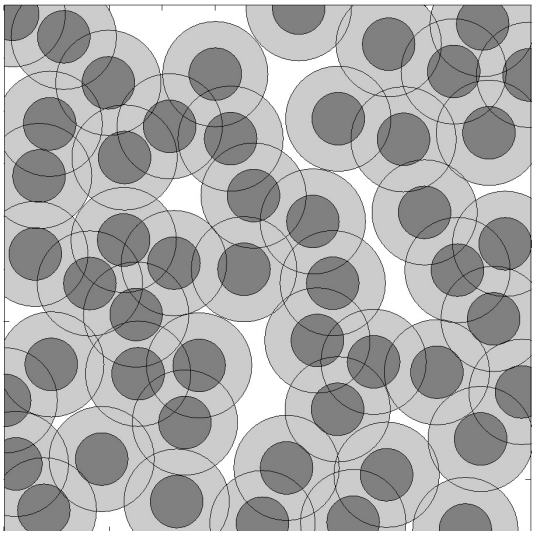

FIGURE 5.6: Inclusions randomly distributed on an RVE in dark gray. If a new inclusion is placed with center on the gray (light or dark) regions then overlap occurs; otherwise, if the particle is centered in the remaining (white) *admissible region* no overlap occurs.

Where V_{av} is the *Free Volume*.

5.2.2 Recursive decomposition of the RVE in domains

5.2.2.1 Recursive decomposition of the RVE

Consider the decomposition of the RVE in four labeled parts corresponding to domains, as depicted on the rectangle at the top of Figure 5.7.

This type of decomposition can be performed repeatedly in any of the obtained domains. As such, in Figure 5.7, the RVE at the top is divided in to four equal domains, and then the domain labeled as 2 is presented in the middle and also divided in to four subdomains. At the bottom of the figure, the subdomain labeled as $2, 1$ is represented, which is also divided in to four subdomains.
Using this type of recursive decomposition, it is possible to locate any point in the RVE by performing successive decompositions of domains.

5.2.2.2 Indicial notation of the domains

In order to reference each of the domains, an indicial notation is used. Therefore, each domain is denoted by a set of indices corresponding to the numeration of the parts chosen in the process of decompositions, as previously described. For instance, the domain represented in Figure 5.7 and denoted by $(2, 1, 4)$ is obtained by decomposition

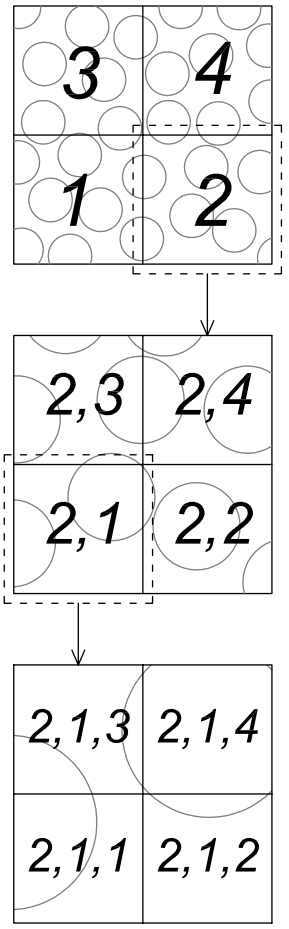

FIGURE 5.7: Decomposition of the domain of the RVE in to four domains (top), decomposition of the domain 2 in to four subdomains (middle) and decompositions of the subdomain $2,1$ in four subdomains (bottom).

of the RVE in four parts and selection of the 2^{nd} part; it is then decomposed again and selecting the 1^{st} part; finally it is again decomposed and the 4^{th} part is selected.

5.2.2.3 Sorting rule for the subdomains

Considering the presented indicial notation the domains can be sorted to have the lowest possible indices on left. Using this definition the number of order k of a domain $(i_1, i_2, ..., i_n)$ is given by expression (5.3).

$$k = \sum_{p=1}^{n} m^{(n-p)}(i_p - 1) + 1 \tag{5.3}$$

Where m is the number of divisions of each domain and n is the number of domain decompositions, while i_p is the value of the index number $p \in \{1..n\}$. Notice that in this work, the number of divisions is always $m = 4$. For instance, regarding Figure 5.7

it was considered $n = 3$ and $m = 4$. Then, in this example there are: $4^3 = 64$ smaller domains, sorted in the Table 5.1 according to expression (5.3).

TABLE 5.1: Sorting order for the domains with $n = 3$ and $m = 4$.

Order	index		
k	i_1	i_2	i_3
1	1	1	1
2	1	1	2
3	1	1	3
4	1	1	4
5	1	2	1
6	1	2	2
7	1	2	3
8	1	2	4
9	1	3	1
10	1	3	2
11	1	3	3
⋮	⋮	⋮	⋮
62	4	4	2
63	4	4	3
64	4	4	4

5.2.3 Domain associated to a volume and the Free Volume Function

5.2.3.1 Domain associated to a volume

For a given number of n decompositions of the RVE, the smallest subdomain $d_k^n(v)$ associated to a volume v, has the number of order k defined by the expression (5.4).

$$k = min\left\{ j \in \{1, 2, ...N\} : \sum_{i=1}^{j} v_i \geq v \right\} \tag{5.4}$$

Where v_i is the *Free Volume* of subdomain d_i with number of order i, according to the sorting numeration defined in expression (5.3) and N is the number of the smallest subdomains. If for n decompositions the subdomain associated to v is d_i^n and for $n+1$ decompositions the subdomain domain associated to v is d_j^{n+1}, then d_j^{n+1} is contained on d_i^n according to expression (5.5).

$$d_i^n = d_i^n(v) \wedge d_j^{n+1}(v) = d_j^{n+1} \Rightarrow d_j^{n+1} \subset d_i^n \tag{5.5}$$

5.2.3.2 The Free Volume Function

Since the smallest subdomain can be as small as intended, depending on the number of decompositions n, the definition (5.4) is used to define the *Free Volume Function* according to expression (5.6).

$$\begin{aligned} f &: \{v \in \mathbb{R} : v > 0 \wedge v \leq v_{av}\} \to \mathbb{A} \\ f(v) &= \left\{x \in \mathbb{A} : \forall n > 0,\ \exists^1 k :\ x \in d_k^n(v)\right\} \end{aligned} \tag{5.6}$$

Where x is a point of the *admissible region* $\mathbb{A}$, v is a scalar volume between zero and the *Free Volume* of the RVE , and d_k^n is the subdomain with number of order k given in expression (5.4) for n decompositions (the concepts of *admissible region* and *Free Volume* have both been previously defined). Informally (5.6) could be understood as: the return of the function f is a point contained in the domain associated to v after infinite decompositions.

The *Free Volume Function* (5.6) holds the properties (5.7) and (5.8).

$$\forall x_0 \in \mathbb{A}\ \ \exists v_0 \in [0, V_{av}]\,, f(v_0) = x_0 \tag{5.7}$$

$$\forall v_1 \neq v_2 \in [0, V_{av}]\,, f(v_1) \neq f(v_2) \tag{5.8}$$

The property (5.7) means that the function is objective, i.e. any point of the admissible region can be obtained applying the relation. As far as the property (5.8) is concerned, it means that the function is injective, i.e. any different values of the domain correspond to different points of the admissible region.

5.2.4 Use of the Free Volume Function in the algorithm

In this algorithm, the inclusions are placed sequentially one after another repeating two operations:

1) selecting a position to place the inclusion;

2) placing the inclusion.

Those operations are repeated until the desired volume fraction of inclusions is achieved. Operation 1) corresponds the evaluation of the *Free Volume Function* of a random number, generated between zero and the total *Free Volume*.

5.2.5 Evaluation and update of the Free Volume Function

Two aspects to be considered for an efficient implementation of the Free Volume Function:

1) the enclosing domain is selected efficiently using a dedicated data structure and algorithm;

2) the *Free Volume Function* changes (since it depends on the distribution of inclusions) each time a new inclusion is introduced, so the data structure used must be updated easily.

5.2.5.1 Structure to store domain data

The Free Volume contained in the domains is stored on a data structure, called *Tree*.

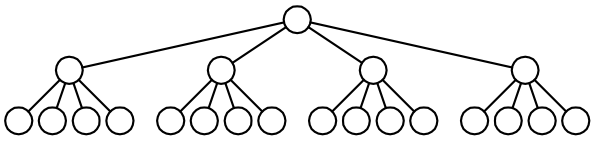

FIGURE 5.8: "Tree" type of data structure.

In the *Tree* data structure represented in Figure 5.8, the circles represent the so called *nodes*. Each node is a set of data and it is connected to other nodes. When considering a specific node, the node connected at the upper level is called *father node* and the nodes connected at a lower level are called *son nodes*. The node without *father node* is called *root node*.

In this problem, each node is associated to a subdomain; the *father node* is associated to the domain where the subdomain is contained and the four *son nodes* are associated to the four subdomains obtained by decompositions of the subdomain. The *root node* is associated to the domain of the whole RVE. The nodes without *sons* are associated to the smaller considered subdomains.

5.2.5.2 Properties of the domain data structure

From the described data structure and the definition of *free volume* it is possible to verify two properties.

Property 1 The *free volume* of a domain can be computed by the sum of the *free volume* of the four subdomains obtained by decomposition of that domain. That implies that the *free volume stored in a node must be equal to the sum of the free volume of its son nodes.*

Property 2 Recalling the expression (5.5) (section 5.2.3) sustaining that if one subdomain is obtained as part of a decomposition of another, and the smallest it is associated to a volume v, then both of the domains are associated to v. This implies that *if a node represents the domain that is associated to a given volume v then one of its father nodes also represents a domain associated to v.*

To illustrate these properties, consider for instance Figure 5.9, where some nodes are labeled "A", "B" and from 1 to 9. The associated free volumes are v_A, v_B and v_1 to v_9.

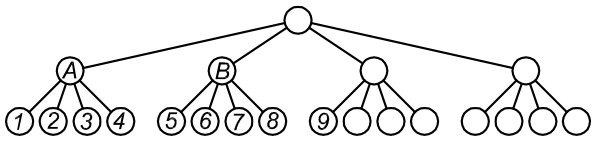

FIGURE 5.9: Data structure with labeled nodes

From Property 1: $v_1 + v_2 + v_3 + v_4 = v_A$. From Property 2, if node 7 is associated to a volume v, then the node B is also associated that volume v.

5.2.5.3 Evaluation of the *Free Volume Function*

The exact evaluation of the *Free Volume Function* is impracticable, since an infinite number of decompositions would be required. Then, this operation is replaced by another that returns a randomly close and valid position (belonging to $\mathbb{A}$) in two steps:

a) determining the enclosing domain of the function's point of return considering a large number of decompositions;

b) selecting a random position of the *admissible region* $\mathbb{A}$ inside the enclosing domain.

The enclosing domain of the exact Free Volume Function, i.e. the domain associated to a given volume, was defined by expression (5.6).
That domain is evaluated efficiently using the domain data structure and its properties (section 5.2.5.2). Regarding property 2, it suggests a recursive procedure: selection of the node representing all the RVE. Then, from the current node selection, the son node representing the domain that encloses the function is obtained. Repeat this strategy

several times.
For a node corresponding to the enclosing domain, the property 1 allows an efficient way to determine which of the son nodes corresponds to an enclosing domain. The son nodes of a given node sorted, according to (5.3) appears in a consecutive order. Also for any two nodes sorted according to (5.3), all the son nodes of the first node have lower numeration than the sons of the second. As a result, the summation that appears on expression (5.4), and also recalled on expression (5.9), can be performed for a set of son nodes using information already computed for the respective father node.

$$\sum_{i=1}^{j} v_i \tag{5.9}$$

Consider for instance the data structure defined on Figure 5.9 and the node B to be the node that encloses a volume v. The volume $V_t = v_A + v_B$ was already computed in order to select the node B to be associated to volume v. Then the sum $v_1 + v_2 + v_3 + v_4$ can be computed as $V_t - v_B$. So that $v_1 + v_2 + \ldots + v_5 = V_t - v_B + v_5$.
A flowchart for the determination of the enclosing domain is presented in Figure 5.10.

In the flowchart of Figure 5.10, v represents the volume for determination of the enclosing domain, d is a counter that indicates the current decomposition and d_{max} represents the maximum number of decompositions.

5.2.5.4 Update of the Free Volume Function

Each time a new inclusion is added to the RVE, the *admissible region* changes. As a consequence, the *free volume* and the *Free Volume Function* change as well. However the structure used to hold the *free volume* in each domain can be changed by updating the data structure.
For the smaller subdomains that surround the new inclusion, a variation of free volume δV is computed. Then in that subdomain and all the subdomains that contain it (i.e. all the succession of father nodes in the tree) are decremented of the value δV. This process is illustrated in Figure 5.11.

A flowchart representing the update process of the structure holding the *Free Volume* in the different domains is presented in the Figure 5.12.

5.2.6 Overall algorithm

Considering the previous statements and algorithms, the overall proposed algorithm is described in the flowchart of Figure 5.13.

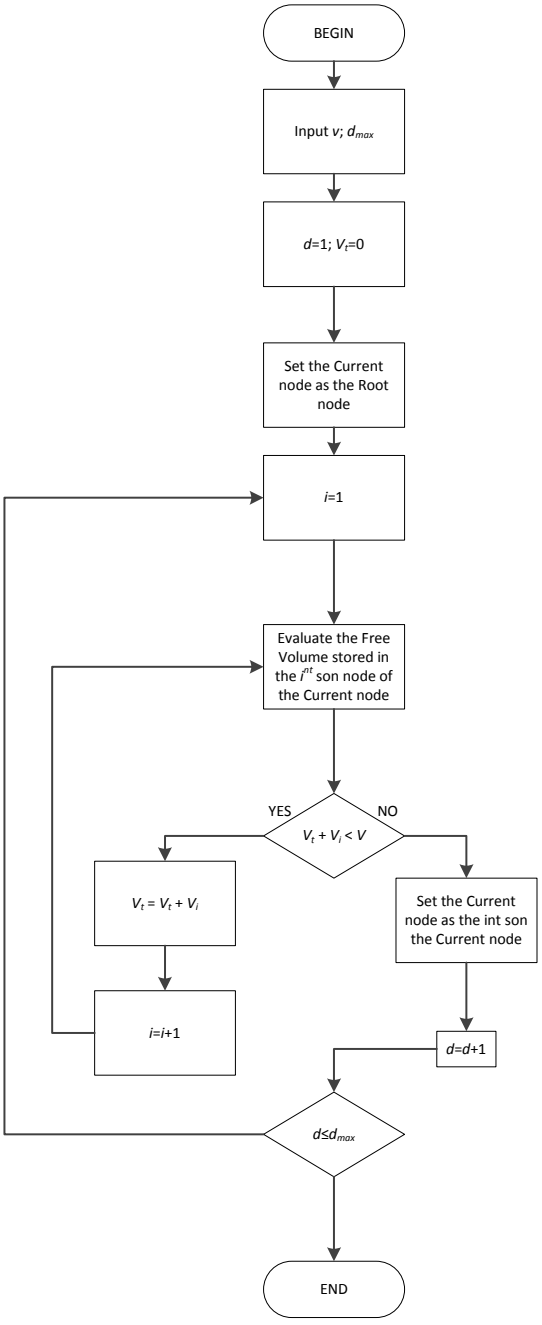

FIGURE 5.10: Flowchart of determination of the enclosing domain of the *Free Volume Function*.

In the presented flowchart N_f represents the number of inclusions, F_v represents the total free volume. v_f^{req} and v_f are the required and current fraction of inclusions.

5.2.7 Size of the smaller domain and number of decompositions

It is possible to sustain that the number of domain decompositions influence the performance of the algorithm in many aspects:

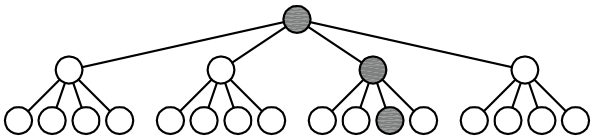

FIGURE 5.11: Update of the structure holding the free volume. If quantity δV is removed from a domain (in gray) same quantity is removed from all the succession of father nodes.

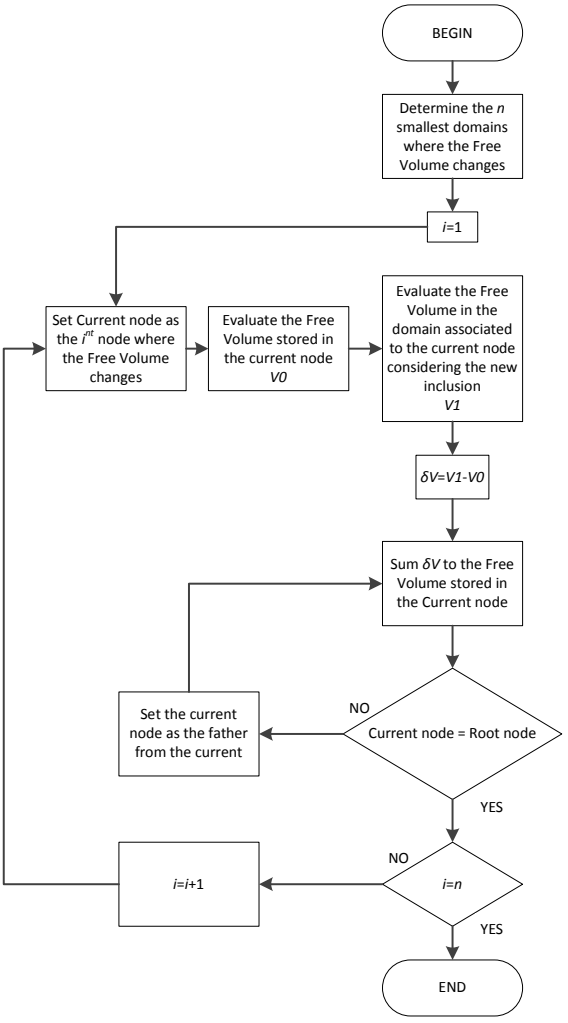

FIGURE 5.12: Flowchart of the *Free Volume structure* update.

1. Area of the smaller enclosing domain and number of inclusions that influence the Admissible Region of that domain;

2. Size of the data structure (number of nodes) used to store the domain data;

3. Number of operations required to update the domain data structure or evaluate the enclosing domain.

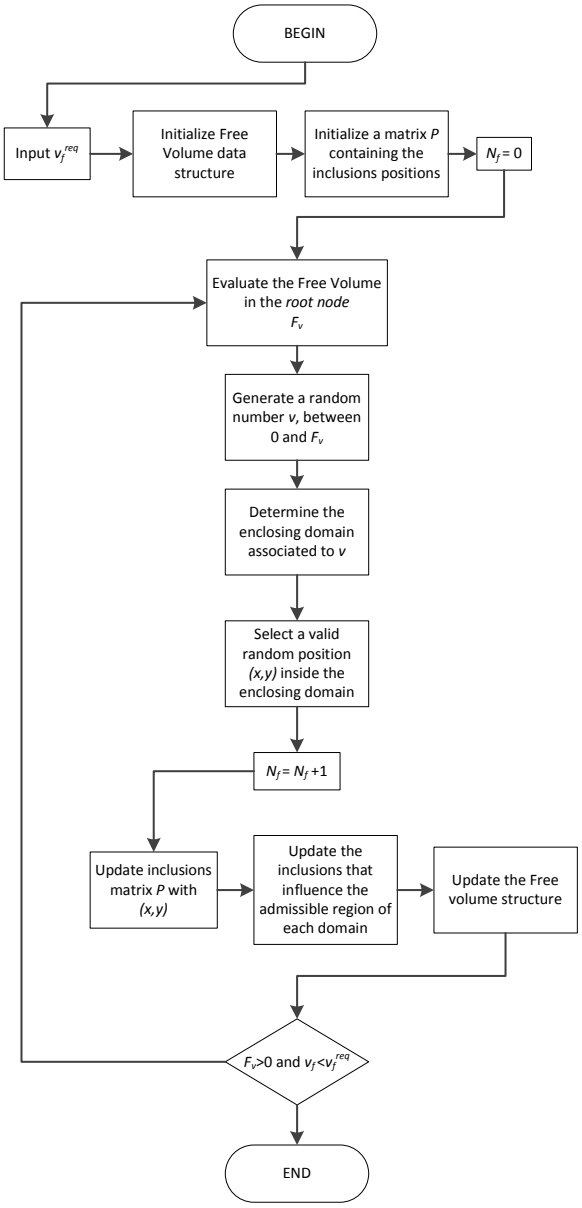

FIGURE 5.13: Flowchart of the overall algorithm.

The previously described, algorithms to update the domain data structure and evaluate the enclosing domain require a number of operations that are proportional to the number of domain decompositions. However, the area of the smaller enclosing domain, as well as the number of inclusions influencing the *Admissible Region* in the smaller domain, decrease in an exponential fashion with the number of decompositions.
In Table 5.2, the evolution of the parameters related to the smaller enclosing domain and the data structure size used are presented for an RVE with the edge of 50 radius ($50R$) of the inclusions, and a volume fraction of 55%.

The average and maximum number of inclusions influencing the admissible region have been estimated using the Monte Carlo Method(MCM) and a random distribution of 10

TABLE 5.2: Evolution of parameters of the smaller domain and data structure size with the number of domain decompositions for an RVE with 55% of inclusions and edge size 50R

Decomp.	Area/R^2	Ave. Inc.	Max. Inc.	Nodes
1	2500	446	446	1
2	625	124.49	133	5
3	156.25	35.89	42	21
4	39.06	11.6	16	85
5	9.77	4.47	8	341
6	2.44	2.15	4	1365
7	0.61	1.33	4	5461
8	0.15	0.97	3	21845
9	0.04	0.82	3	87381
10	0.01	0.75	3	349525

Decomp. - number of domain decompositions
Ave. Inc. - average number of inclusions influencing the Admissible Region†
Max. Inc. - maximum number of inclusions influencing the Admissible Region†
Nodes - total number of nodes of the data structure
†Estimative using Monte Carlo method

thousand enclosing domains for each number of domain decompositions.
The number of domain decompositions was selected in order to reduce the computation time and to use no more than the common standard of available memory in a common computer. A number of decompositions were selected, allowing an edge length of the order of $0.78R$. In this way, only a small number of inclusions influencing the enclosing subdomain need to be considered in order to select a valid position inside the enclosing domain. For a RVE with edge length $50R$, this option corresponds to seven domain decompositions.

5.2.8 Advantages and limitations of the method

With this strategy, the speed of the algorithm does not depend on the number of particles placed and its complexity is linear ($O(n)$). Since the inclusions are randomly distributed, there is no optimization of the inclusion packing in order to obtain volume fractions higher than 55%. Furthermore, it is possible to sustain that the method is eminently suitable to generate distributions of inclusions in RVEs with any geometry and to fill with circular inclusions of the same size gaps generated by other methods of generating RVEs.

5.3 Performance analysis

In order to verify the performance of the algorithm and compare it with others, several studies have been performed in different RVEs. For a constant inclusion volume fraction

$\phi_c = 0.58$, models with different ratios of edge length a and inclusion radius R have been generated and the time has been measured. The results obtained for different relations (a/R) in the present algorithm and the one proposed in [46] are described in Table 5.3.

TABLE 5.3: Time required to generate the models (inclusion volume fraction $\phi_c = 0.58$) for different edge length per radius relations (a/R).

RVE size	Computation Time (min)	
a/R	FREE_V	RAND_uSTRU_GEN
30	0.07	0.36
50	0.17	0.62
70	0.35	1.09
100	0.64	1.71
120	0.98	2.95
150	1.76	6.10

5.4 Statistical characterization of the models

The randomness of an inclusion distribution can be quantified numerically, using statically procedures. A review of such statistical procedures can be found in [46].
In order to compare the statistical characterization of the presented algorithm with the one already provided for other algorithms in [46], the same statistical procedures and variables were adopted.

5.4.1 Voronoi areas and neighbouring inclusion distance

Five models were generated with the described algorithm considering an RVE size of 50 inclusion radius $(50R)$ and a fraction of inclusions $\phi_c = 0.56$. For each of the models, a distribution of Voronoi areas was obtained, as well as a distribution of neighboring inclusion distances. For each distribution, the coefficient of variation of the areas (ρ_A) and distances (ρ_D) was computed according to expression (5.10).

$$\rho(\chi) = \frac{\sigma(\chi)}{\mu(\chi)} \tag{5.10}$$

Where χ is the random variable, $\sigma(\chi)$ is the standard deviation and $\mu(\chi)$ is the mean. Table 5.4 presents the average values obtained for the described algorithm (FREE_V), and the ones provided by [46] for other methods.

For the Voroni areas, the FREE_V method appears to originate higher values of variation than the other methods. Regarding the distances to the neighbor inclusion, the FREE_V

TABLE 5.4: Coefficient of variation for Voronoi polygon areas and distances to neighbor inclusions.

Method	ρ_A	ρ_D
FREE_V	0.144	0.193
RAND_uSTU_GEN	0.137	0.196
Wongsto's method	0.129	0.190
Matsuda's Y-distribuition	0.106	0.190
Matsuda's point distribuition	0.135	0.256

method originates values near to the ones obtained with the other methods, with the exception of Matsuda′s point distribution, where the variation is much higher than the other methods.

5.4.2 Distribution functions

An overall of 20 RVE models have been generated with edge length of 50 radius (50R) and a fibre volume fraction of 56% using the FREE_V method and the RAND_uSTRU_GEN method provided in [46]. The statistical descriptors Ripley's K function, Pair distribution function, Nearest neighbours probability density functions (PDF), Nearest neighbour orientations PDF have been computed. The obtained curves for both methods are very similar in almost all descriptors except in the Nearest neighbours PDF.

The PDF associated to the variable distance to the first neighbour inclusion of a random inclusion is represented in the Figure 5.14. The graphic shows that PDF for the periodic

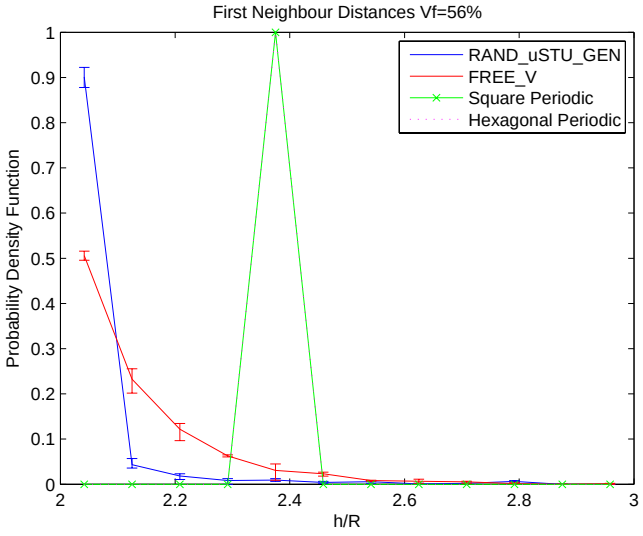

FIGURE 5.14: First neighbour distances for an inclusion fraction $\phi_c = 0.56$.

distributions exhibits a peak where all probability is concentrated. For the random distributions generated with the methods RAND_uSTRU_GEN[46] and FREE_V the higer probility values are found at distances near to the inclusion, and reduces monotonically

to zero as the distance increases. In the case of the FREE_V method, the maximum value of PDF is much lower than the obtained for the RAND_uSTRU_GEN one. The reduction of the probability with the distance is smoother in the case of the method FREE_V than in the RAND_uSTRU_GEN method.

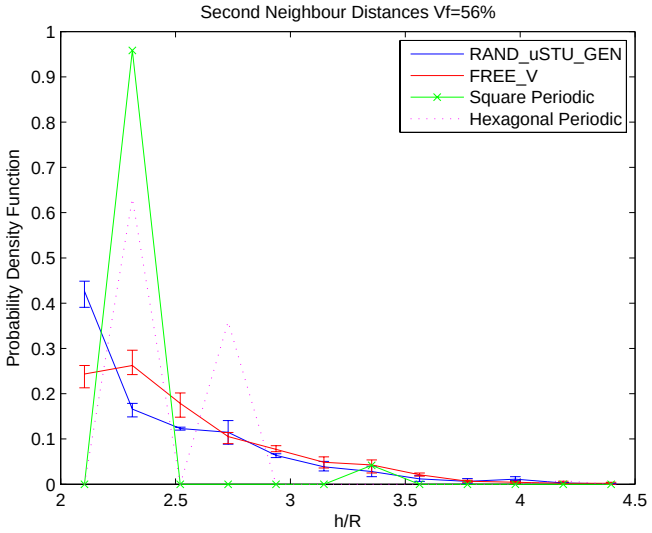

FIGURE 5.15: Second neighbour distances for an inclusion fraction $\phi_c = 0.56$.

For the second neighbour distances PDF (Figure 5.15), the curves obtained by the methods differ considerably. While the PDF curve associated to RAND_uSTRU_GEN decreases monotonically from the highest value at a near distance from the inclusion, the PDF curve associated to FREE_V presents a small increase followed by a smooth monotonic decrease. In the PDF associated to the third neighbour distance (Figure 5.16), the curves for the two tests methods do not fit each other, despite having a similar behaviour.

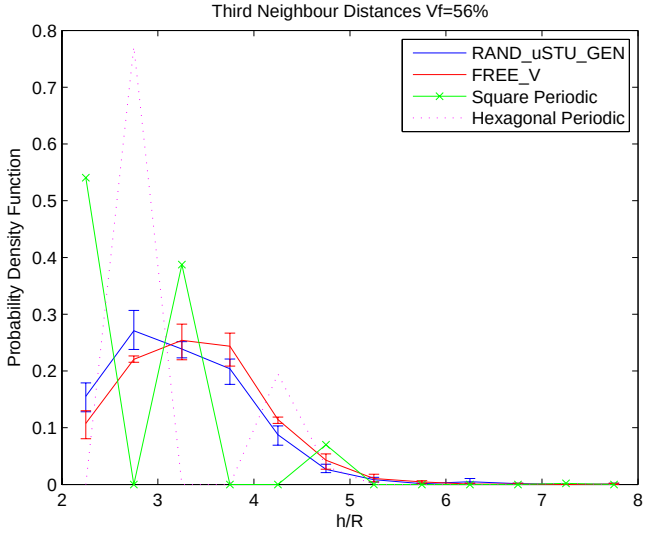

FIGURE 5.16: Third neighbour distances for an inclusion fraction $\phi_c = 0.56$.

5.5 Micromechanical characterization of the models

This section describes a numerical experiment where RVE models have been generated in order to characterize a composite material. For such models, homogenized elastic properties have been obtained using the finite element method (FEM) and homogenization techniques. Afterwards, the results were compared with experimental data.

5.5.1 Material

Panels of a unidirectional E glass fibre/913 epoxy resin composite described in [57] were considered. The material has a fibre radios of $R = 15\mu$m, a fibre volume fraction $\phi_c = 0.54$ and the elastic properties of the matrix and fibres are defined in the table 5.5.

TABLE 5.5: Material properties.

Propreties	Young's moduli E(Gpa)	Poison's ratio ν
Epoxy resin	5.32	0.365
E-glass fibre	72.5	0.20

5.5.2 Generated models

A total number of 400 models have been generated using the algorithm described in the previous sections. The generated models have a square shape with the edge of 50 radios of the inclusions (50R). It was assumed that the real material is a repetition in a periodic pattern of the generated models; therefore, the left and bottom edges must match geometrically with the right and top respectively. A model generated with the FREE_V algorithm is depicted in the Figure 5.17.

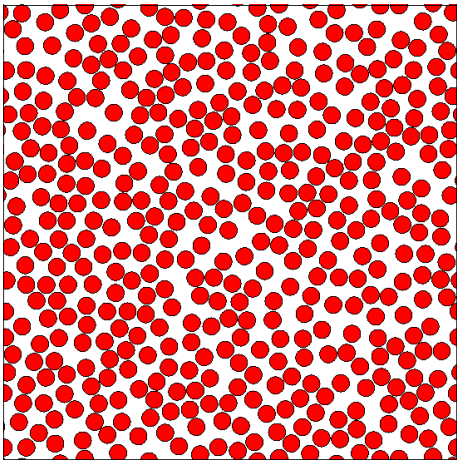

FIGURE 5.17: Model allowing a geometrical periodic pattern assumption for the real material ($a = 50R$ and $\phi_c = 0.54$).

A plane strain state was considered and isoparametric planar triangular elements with 3 nodes and 1 gauss point have been used. An average of 73000 nodes and 144000 elements per model were used. A detail of the refinement of the generated meshes is presented in Figure 5.18.

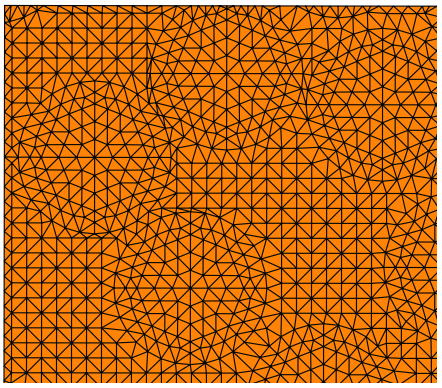

FIGURE 5.18: Detail of the refinement of the used mesh.

The meshes have been generated using Delaunay tessellation according the process suggested in [46].

5.5.3 Numerical simulation

The simulations have been performed using software specially conceived for the purpose of micro-scale simulation based on FEM, described in Chapter 3. In the calculations, strains are prescribed to the RVEs using boundary conditions and the equivalent homogenized stress computed. With periodic boundary conditions, the left bottom node is considered constrained, while the remaining boundary nodes are constrained according to equations (5.11):

$$\begin{aligned} \mathbf{u}_B + \mathbf{u}_T + \mathbf{u}_{LT} &= 0 \\ \mathbf{u}_L - \mathbf{u}_R + \mathbf{u}_{RB} &= 0 \\ \mathbf{u}_{RT} - \mathbf{u}_{RB} - \mathbf{u}_{LT} &= 0 \end{aligned} \tag{5.11}$$

where B, T, L and R denote bottom, top, left, and right.

5.5.4 Determination of homogenized properties

For each model, three different small deformations corresponding to three small strains ε have been applied (horizontal tensile, vertical tensile and pure shear) and the respective stress σ has been computed.

The obtained stress and strain allow the determination of the constitutive relation and the matrix $\mathbf{C}$ of the material that respects the relation (5.12).

$$\boldsymbol{\varepsilon} = \mathbf{C}\,\boldsymbol{\sigma} \tag{5.12}$$

The homogenized properties have been obtained directly from the matrix $\mathbf{C}$ components according the expression (5.13).

$$\begin{aligned} E_1 &= 1/C_{11} \\ E_2 &= 1/C_{22} \\ \nu_{12} &= -C_{21}\,E_1 \\ \nu_{21} &= -C_{12}\,E_2 \\ G_{12} &= 1/(2\,C_{66}) \end{aligned} \tag{5.13}$$

Where E is the Yong′s moduli, ν is the Poisson′s ratio and G is the shear modulus; the numeric indexes 1 and 2 denote the directions orthogonal to the fibres.

5.5.5 Analysis and results

Figure 5.7 presents the stress field for the horizontal direction, i.e. direction 1 (σ_{11}) obtained for one of the distributions subjected to a tensile strain in the direction 1. It is

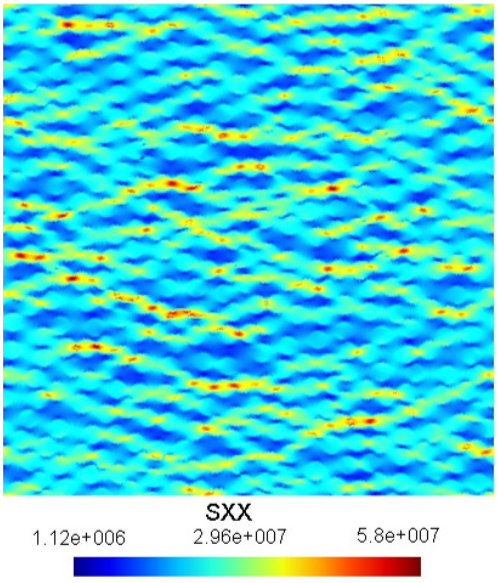

FIGURE 5.19: Normal stress σ_{11}(Pa) obtained for a traction in the direction 1 (horizontal direction).

possible to verify that the field of stress is influenced by the pattern of inclusions. The higher values of stress are distributed preferentially accordingly to groups of inclusions that join together in the direction of the stretch.

Figures 5.20 to 5.22 present the histograms corresponding to the calculated elastic properties. Table 5.6 shows the experimental measured properties and a synthetizes of the numerical analysis.

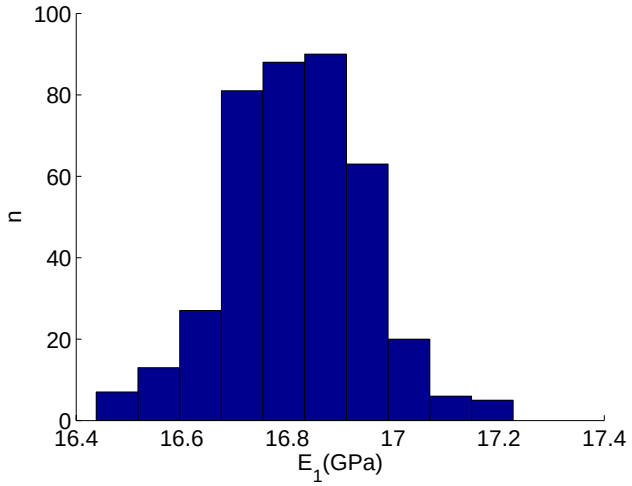

FIGURE 5.20: Histogram of the obtained Yong's moduli E_1.

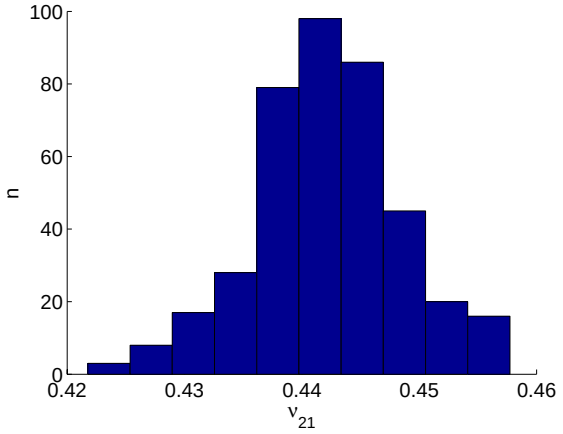

FIGURE 5.21: Histogram of the obtained Poisson's ratio ν_{21}.

TABLE 5.6: Comparison of experimental and numerical determined properties.

	Experimental‡	Mean	Std. Dev.	Error(%)	Gusev‡
E_1(GPa)	17.1	16.816	0.1295	1.7	16.0
E_2(GPa)	17.1	16.792	0.1675	1.8	16.0
ν_{12}	0.391	0.444	0.00421	13.6	0.410
ν_{21}	0.391	0.442	0.00627	13.1	0.410
G_{12}(GPa)	6.07	5.829	0.0517	4.0	5.61

‡ values mentioned in [57] and assumption of traversal isotropy

The transversal isotropy is verified by the relations $E_1 = E_2$, $\nu_{12} = \nu_{21}$ and $G_{12} = G_{12}^{calc} = \frac{E_1}{2(1+\nu_{12})}$ that are expressed in term of ratios in the table 5.7.

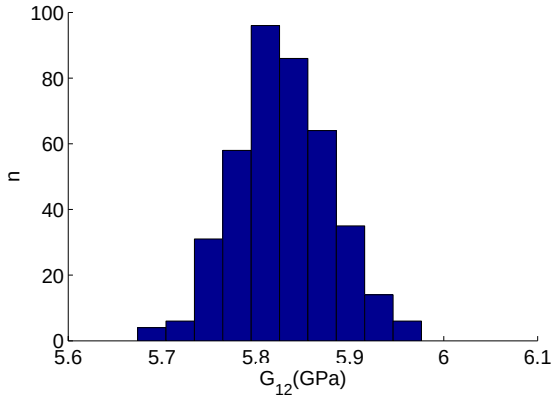

FIGURE 5.22: Histogram of the obtained Shear modulus G_{12}.

TABLE 5.7: Verification of transversal isotropy.

	$\frac{E_1\nu_{21}}{E_2\nu_{12}}$	$\frac{E_1}{E_2}$	$\frac{\nu_{12}}{\nu_{21}}$	$\frac{G_{12}^{calc}}{G_{12}}$
Mean values	1.006	1.001	1.005	1.001

It is possible to conclude that the results show a good agreement between the experimental results and the numerical predictions. Besides, the relations between homogenized properties confirm that the use of the proposed algorithm conducts to isotropic models.

5.6 Improved Algorithm

In the algorithm described in section 5.2, inclusions can be added until no *Admissible Region* is available. However, since the inclusions are distributed randomly, there is no packing optimization and the maximum volume fractions obtained tend to be under 55%. In this section a modified algorithm, which allows higher volume fractions, is described.

5.6.1 Free Volume Modified

In the previous algorithm, all the points of the *Admissible Region* have the same probability to be chosen in order to place a new inclusion. In the improved algorithm the probability of a point of the *Admissible Region* to be selected to place a new inclusion randomly changes and is conditioned by a packing criterion. This way, the packing criterion allows the definition of a non-constant field of probabilities for an inclusion to be placed.

In order to modify the probability field, a modified variable, the *Free Volume Modified* W_f derived from the *Free Volume* V_f is used.

Placing inclusions near to existing ones conducts to a smaller reduction of the total *Free Volume* than in arbitrary positions. It also tends to produce a more compact structures. In accordance to this packing criterion, the areas near the existing inclusions have a higher contribution to the total W_f than the ones that are far from the inclusions. When placing a new inclusion, a random number w between 0 and W_f, is selected and associated to a region that corresponds to that w. This implies that when placing a new inclusion, the points in areas near the already placed inclusions have a higher probability to be selected than others that are far.
The relation between V_f and W_f in the smallest domain decomposition with area A, can be related using a scalar *Transformation Function* g according to the expression (5.14).

$$\frac{W_f}{A} = g\left(\frac{V_f}{A}\right) \tag{5.14}$$

The function g should be defined within the interval $[0; 1]$.

5.6.2 Transformation Function

A wide range of *Transformation Function* types can be adopted, the following examples are described: linear(expression(5.15)), bilinear(expression(5.16)) and inverse proportional(expression(5.17)).

$$g_1(x) = \begin{cases} k\,x & \text{if } x < \delta \\ 1 & \text{otherwise} \end{cases} \tag{5.15}$$

$$g_2(x) = \begin{cases} g_0 + \frac{1-g_0}{1-x_0}(x - x_0) & \text{if } x = 0 \\ x\frac{g_0}{x_0} & \text{otherwise} \end{cases} \tag{5.16}$$

$$g_3(x) = \begin{cases} min(g_{max}, \frac{1}{x^n}) & \text{if } x > 0 \\ 0 & \text{otherwise} \end{cases} \tag{5.17}$$

Where k, δ, x_0, g_0, g_{max} and n are parameters empirically determined in order to obtain high volume fractions without compromising the randomness of the distributions.

5.6.3 Model generated with the improved algorithm

Figure 5.23 shows a square model with edge $a = 50R$ and a fraction of inclusions $\phi_c = 0.62$ generated using the improved algorithm with the *Transformation Function* g_3 defined in (5.17) with parameters $g_{max} = 400$ and $n = 1.2$.

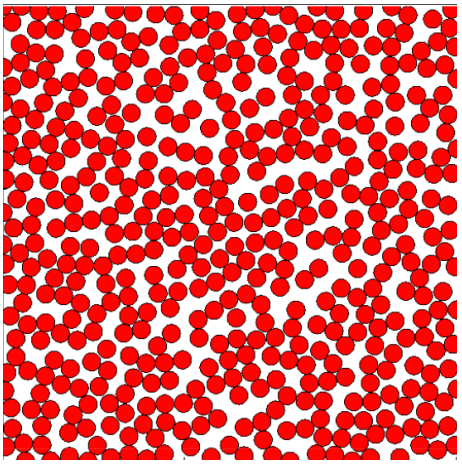

FIGURE 5.23: Model generated using the improved algorithm ($a = 50R$ and $\phi_c = 0.62$).

5.7 Conclusions

In this Chapter, a new algorithm to generate material models based on a random distribution of inclusions was presented. The presented concept of free volume function is fundamental for the algorithm to produce random models efficiently. The presented algorithm has linear complexity ($O(n)$) allowing a highly efficient computation of large models, in accordance and confirmed by performance tests. Furthermore, simulations to predict the mechanical behaviour of a composite fibre glass material, using the FEM method and homogenized techniques, have been also performed. The results show a good agreement with the experimental data. The transversal isotropy of the generated models was confirmed.
Due to the perfectly random distribution of the inclusions, the obtained models do not have, in general, fractions of inclusions higher than 55%. To overcome this problem, a variation of the algorithm that includes a packing heuristic is proposed. However, no numerical experiments were conducted with models generated by the improved algorithm. In addition, the proposed algorithm can be easily extended to generate distributions of spheres in three dimensional spaces and multi-dimension spaces.

Notwithstanding, an important improvement of the algorithm would be the development of a process that excludes from the generation, models with a lower volume fraction. However, this process should keep an important property of the algorithm: all the models with the same fibre volume fraction have the same probability of be generated. A possible idea to achieve this could be the use of an initial distribution with the required volume fraction reallocating the inclusions randomly and repeatedly.

Chapter 6

Microstructure of the Materials and their Macroscopic Properties

6.1 Introduction

In the previous chapters, the basic principles of homogenization and their application were presented. Then the problem of the generating of realistic RVEs, and their statistical representatively was analysed. Furthermore, a new algorithm for the generation of RVEs with disk inclusions was presented. In this chapter, the attention turns to the relationships between the microstructure of the material and its macroscopic properties. Those existent relations are numerically investigated.

Computational homogenization is a very powerful and promising tool. However, it is a complex and demanding field, since:

- it requires a "statistically accurate" generation of the geometry of the models, which should reproduce the truly random nature of the real materials and their microstructure.
- the geometrical complexity can result in extremely expensive computationally problems or difficulties to mesh using automatic procedures;
- it is hard to access the precise morphology, constitutive laws and properties of the materials at the microstructure (for instance, the interface transition zone (ITZ) in concrete, described by [58], remains an important issue of research);
- the homogenization strategy for nonlinear regimes is still on debate by the scientific community;

- the simulation of microstructures conducts to significant amounts of data and calculation errors which are difficult to manage automatically.

The above mentioned reasons justify why a large amount of homogenization research work only deals with simple, isotropic, two phase RVEs, based on a matrix reinforced (or weakened) by disk or spherical inclusions. For contextualization purposes, the following subsections refer to practical issues on the application of homogenization, RVE size and the influence of the morphology on the statistical distribution of the properties.

On this study, and for simplicity reasons, a material composed by inclusions randomly distributed on a uniform matrix and its heterogeneous distribution was considered. To conduct the analyses, a general framework that generates and simulates RVEs, based on the FEM method and on the homogenization techniques mentioned in the previous Chapters 3 and 4, was developed. Two and three-dimensional RVEs were generated and the variation of the properties investigated using a statistical approach. An outline of the study is given in subsection 6.1.6.

6.1.1 Practical applications and RVE size

Practical applications impose restrictions on the morphology of the RVE due to the lack of information of the micro structural geometry or the inability to manage the complexity of the geometry. Because of these reasons, the level of detail of the micro structure, the geometrical features of the inclusions, the size of the RVE, and other simplifications should be carefully decided. In fact, there is a well-known trade-off between RVE size, accuracy and computational time to perform the simulations. For instance, in the case of unidirectional fibre reinforced composites (FRC), periodic considerations of simplistic RVE structures, assuming a hexagonal periodic distribution, can be successfully employed for some specific purposes, despite it has been shown (see for instance [13]) that they cannot capture important characteristics related to the distribution of the micro fields in the material (e.g. probability of failure).
The size of the RVE depends on the physical properties to homogenize. For instance, in a study of homogenization of a two-phase three dimensional Voronoi mosaic (see [39]), it is shown that the RVE size differs if the thermal conductivity or elastic properties are considered. Additionally, [59] found that for a typical unidirectional carbon fiber-reinforced composite (considering the transverse plane), the minimum RVE size is related to the chosen physical properties to consider, such as, similarities in the distributions of stress or strain in the matrix, elastic properties, average deformation energy, etc.
In the literature, some studies investigate the minimum RVE size for specific materials and applications. For instance, the work of [60] attempts to determine the minimum

RVE size associated to the effective modulus of a two phase random material composed by a dispersion of non-overlapping identical spheres. On its turn, the work of [59] establishes the minimum RVE size for unidirectional FRC according to the geometry and micro field criterion. Kanit[39] provides a good review of the methodologies proposed to define the minimum RVE size.

6.1.2 Fluctuations of results, RVE size and morphology

The relation between the fluctuation of results and the geometry of the RVE constituents has been addressed for some particular cases. Ostoja[61] considered 2D RVEs based on a matrix with thin needle-shaped inclusions to obtain homogenized elastic properties. Considering a constant range of fluctuations on the homogenized properties it was observed that the required size of the RVE depends on the aspect ratio of the inclusions. Ren [62] and [63] considered 2D RVEs based on polycristals and determined a relation between the size of the RVEs and the level of anisotropy of single crystals.

6.1.3 Attempts to reduce the size of the RVEs

In order to reduce the size of the RVEs required to perform homogenization, some methodologies have been proposed. Zeman[64] considered laboratorial images of a unidirectional FRC of graphite, and used an optimization technique to generate a small volume of the geometry. This element of volume tends to be more representative than a volume extracted from the original images with the same size at a random position. In the works of Gusev[65] and Kanit[39], effective properties were obtained using a large amount of smaller samples (Monte Carlo method) than the representative RVE and considering the main statistics.

6.1.4 The morphology of the RVE and the distribution of the effective properties

The strategy to obtain the effective properties, using the Monte Carlo method with a large amount of runs, consists of estimating the expected properties of the RVE as average values obtained for a large amount of samples. The strategy is in agreement with the central limit theorem, which is valid for a large amount of samples. The central limit theorem assumes that if a random variable Y is defined as average of an amount of n random variables X_i $(1 \leq i \leq n)$ with any type of distribution, then Y tends to a normal distribution as n tends to infinity, with the same expected value as X_i. However, the rate at which the variable Y approximates the normal distribution depends on the

type and dispersion of the random variables X_i.
If the overall homogenized properties are considered as random variables, then the relations between the statistical distributions of those variables and the parameters of the RVE (geometry of inclusions, volume fraction, etc.) are very important in this context. In fact, these relations can provide the roots to a more direct connection between morphology and representativeness of the RVEs. This would allow a better understanding of the stochastic behaviour of materials, when associated with the morphology.
As the RVE size (to obtain a scatter within a given tolerance) and the geometry seem to be related in some cases, it might be possible to establish a relation between the type and parameters for the random distribution associated with the effective properties and the morphology of the RVE.

6.1.5 The distribution of homogenized properties and reliability of the materials

The connection between the inclusion properties and the variability of the homogenized material properties can be used for reliability design purposes. Furthermore, the distribution of the extreme stress and strain values at the finer scale (responsible for certain damage mechanisms), for a given set of RVEs, is probably dependent on the morphology of the components. Then, for tailored materials, it could be of interest to associate the geometry of the constituents with the reliability of materials, developing parametric failure, yielding, or other threshold criterion for instance.

6.1.6 Outline

In Section 6.2,a general framework that generates and simulates RVEs is described. The assessment and validation of the framework is presented in Section 6.3. The validation includes the selection of an appropriate mesh refinement and the comparison of results with classical analytical models. Sections 6.4 to 6.7 report a comprehensive set of experiments on RVEs based on disc inclusions randomly distributed on a uniform matrix. In particular, in Section 6.4, the type of stochastic variable that is associated with the overall homogenized elastic property of a randomly generated RVE is investigated. Section 6.5 illustrates how the mismatch of stiffness between matrix and inclusions can affect the spread of the homogenized properties. In Section 6.6, a thin interface layer that surrounds the inclusions is considered, and the influence of such interface on the overall properties is investigated. Section 6.7 compares the dispersion of the overall properties using models of two or three dimensions. The conclusions of the studies are summarized on Section 6.8.

6.2 Test set-up and implementation issues

In this section, the framework developed to generate RVEs of the material (regarding it's micro structure) and the computation of the overall properties are described. Moreover, a computational implementation of the principles mentioned on Chapter 3, within the commercial software ABAQUS, is briefly explained.

6.2.1 Discretization and implementation on ABAQUS

Recalling, the algorithm for computational homogenization of RVEs described in Chapter 4, it considers the Hill-Mandel principle, the kinematic restrictions and the equilibrium conditions (Equations 3.2 to 3.5) mentioned in Chapter 3. In order to comply with those principles, classical boundary conditions were considered by applying interpolation, between nodes in opposite faces and edges of the RVE. However, in order to obtain a simple process to generate the meshes and post process the data, those same principles and strategy of interpolation was used within the commercial FEM software ABAQUS.

Among the classical boundary conditions that can be considered are:

- Taylor assumption;
- Linear displacements on the boundary;
- Periodic displacements and anti-periodic tractions on the boundary;
- Uniform traction on the boundary.

The last three types of boundary conditions have an asymptotic convergence of the homogenized properties as the size of the RVE increases[66]. Nevertheless, the boundary condition that enforces periodic displacements is the one that is able to produce better results in the linear regime according to several studies[38], [66]. Therefore, the periodic boundary condition was the one employed in the current study.

The enforcement of periodic boundary conditions on ABAQUS was implemented using linear constrains equations between the degrees of freedom. Since, in general, the boundary nodes do not exactly match the opposite ones, those nodes are related, with the nearest ones on the opposite face, through interpolation, as explained in section 4.2.1.

6.2.2 Algorithm used to generate the RVE

In order to generate the geometry of the model, a classical general algorithm, the so-called random sequential addition (RSA)[67], was adopted. In this algorithm, the fist inclusion is inserted in a random position of the matrix. Then, the next inclusions are introduced sequentially one by one in a random position such that they do not overlap the ones already placed in the RVE (this is usually achieved by trial and error approach). If there are no modifications to the original algorithm (e.g. domain decomposition), then the computational time increases at high rate, as the number of inclusions increases. This happens because whenever a new inclusion is inserted, the overlap with all other particles has to be verified. Efficient alternatives to this algorithm, were proposed in the Chapter 5, but also in the works of Melro[46], Wongsto[44] and others. Nonetheless, the RSA algorithm was selected, due to its simplicity, general purpose and guarantee of generate a perfectly random distribution by construction.
The RVE with the form of a square or cubic domain, should be able to create a medium without discontinuities on the inclusions, as the RVE is placed in a orthogonal regular mesh. In order to fulfill this criterion, the RSA algorithm is slightly modified: when an inclusion is placed randomly, copies of the same inclusion are also placed attending to the periodicity of the medium and the boundary. Therefore, the verification of overlapping also has to be examined for all copied instances. The modified RSA algorithm adopted is presented in Figure 6.1.

6.2.3 Strategy used to compute the overall elastic properties

The macroscopic elastic properties are obtained from the constitutive elastic matrix, which is obtained from a set of stress strain-pairs. For a given RVE, different strain states are applied independently using the periodic boundary conditions, as defined by expression (3.23). For each of those strains, the stress state is computed using the FEM method, and converted into homogenized stress using the average definition described in expression (3.1). Considering, that each of the stress-strain pairs, are related according to expression (6.1).

$$\boldsymbol{\varepsilon} = \mathbf{C}\,\boldsymbol{\sigma} \tag{6.1}$$

Where, $\boldsymbol{\sigma}$ is the stress tensor, $\boldsymbol{\varepsilon}$ is the strain tensor and $\mathbf{C}$ the matrix expressing the linear relation. Then it is possible to invert the relation (6.1) to obtain $\mathbf{C}$, given the

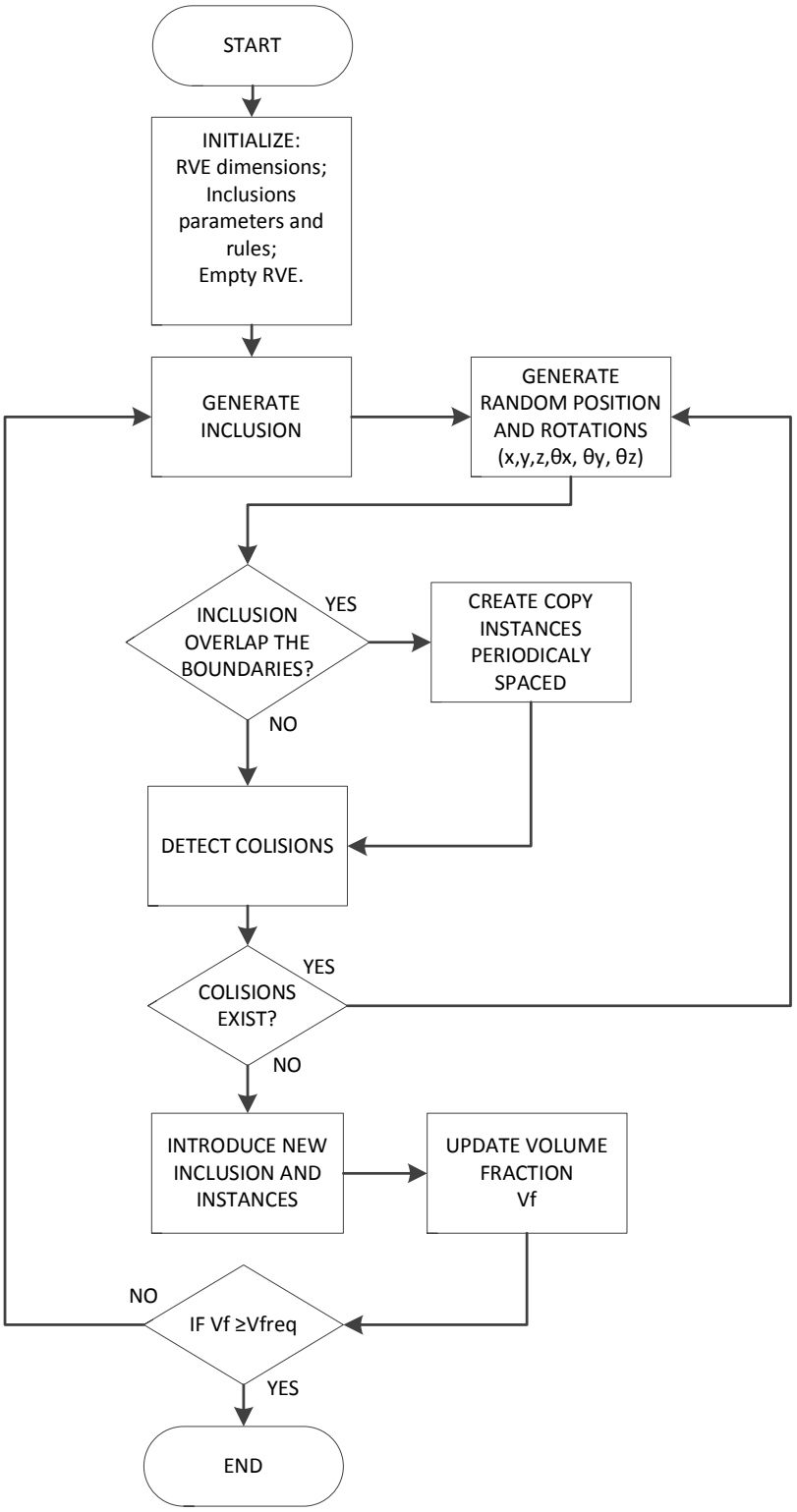

FIGURE 6.1: Flowchart of the RSA modified algorithm to generate the RVE.

stress-strain pairs. Assuming a generic orthotropic material, the **C** matrix is given by:

$$\mathbf{C} = \begin{bmatrix} \frac{1}{E_1} & \frac{-\nu_{23}}{E_2} & -\frac{\nu_{31}}{E_3} & & & \\ -\frac{\nu_{12}}{E_1} & \frac{1}{E_2} & -\frac{\nu_{32}}{E_3} & & & \\ -\frac{\nu_{13}}{E_1} & -\frac{\nu_{23}}{E_2} & \frac{1}{E_3} & & & \\ & & & \frac{1}{2G_{23}} & & \\ & & & & \frac{1}{2G_{31}} & \\ & & & & & \frac{1}{2G_{12}} \end{bmatrix}. \tag{6.2}$$

In expression (6.2), E is the elasticity modulus, ν is the Poisson ratio and G the shear modulus. The sub-indexes stand for the direction associated with each variable. Considering the symmetry of the matrix $\frac{\nu_{23}}{E_2} = \frac{\nu_{32}}{E_3}$, $\frac{\nu_{31}}{E_3} = \frac{\nu_{13}}{E_1}$ and $\frac{\nu_{12}}{E_1} = \frac{\nu_{21}}{E_2}$. Consequently, general 3D problems require determining nine coefficients of **C** matrix. While, planar (2D) problems require determining only six coefficients.

6.2.4 Work flow of the implementation

The flowchart of the general framework, which generates RVEs and computes homogenized properties in the commercial software ABAQUS and MATLAB, is presented in Figure 6.2.

In the first step, MATLAB is used to run scripts that allow the generation of the geometric definition of the micro structure of the RVE. Then, MATLAB calls for ABAQUS which uses a Python script to generate a working model (mesh, boundary conditions etc.), and proceeds to the FEM stress strain analysis. From the obtained stress state, the homogenized stress is computed (using a Python script) and then retrieved back to MATLAB. Finally, MATLAB is used to compute the elasticity matrix and the homogenized elastic properties of the overall RVE.

6.3 Validation of the framework

In this section a validation of the framework is described, and developed in order to compare the homogenized properties of an RVE composed by realistic materials, and the ones obtained by theoretical and empirical expressions of the literature.

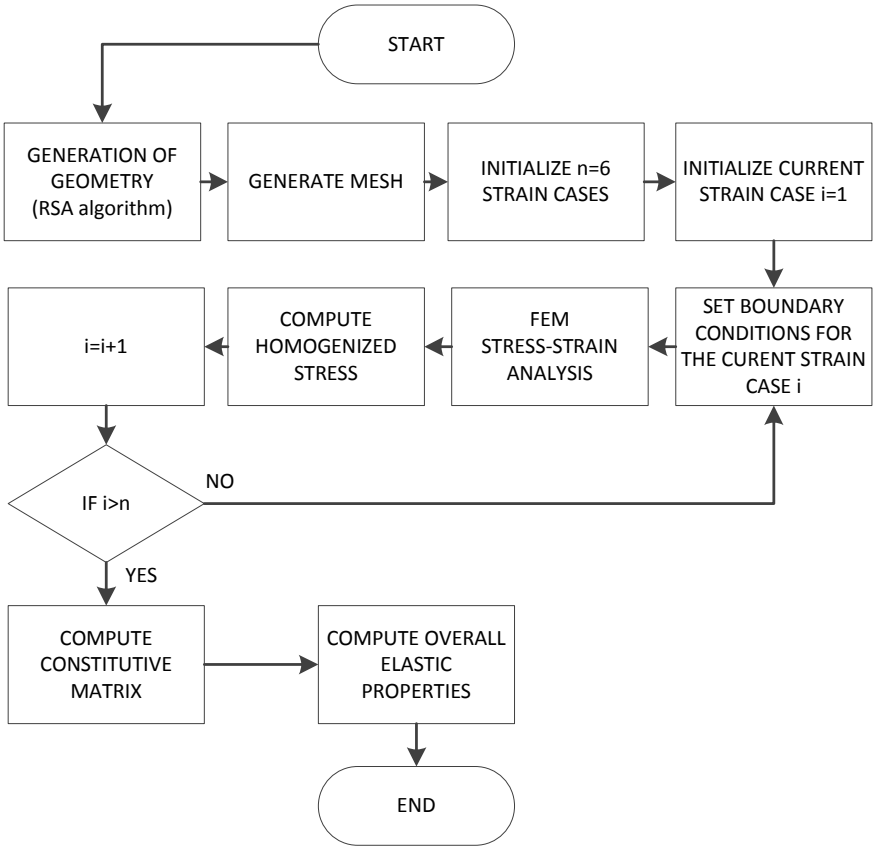

FIGURE 6.2: Flowchart of the general framework.

6.3.1 Material Parameters

In order to validate the framework, an Epoxy Fiber Glass Composite material was considered. The elastic propreties of the fibres and resin phases of this composite, are defined in Table 6.1, accordingly to [68] regarding the material E glass/MY750/HY917/DY063.

TABLE 6.1: Parameters of the composite material.

L/R	V_f	E_i (GPa)	ν_i	E_m (GPa)	ν_m
20	0.3	74	0.2	3.35	0.35

In this Table 6.1, the index i stand for inclusion, the index m stands for matrix, L is the size of the edge of the RVE and V_f is the inclusion volume fraction. The scalar E is the elasticity modulus and ν is the Poisson ratio.

6.3.2 Mesh refinement

Since this example aims to evaluate the dispersion of the homogenized properties due to geometrical factors, it is very important to reduce the contribution of the calculation

errors. Otherwise, the dispersion of the homogenized properties would be be biased. Therefore, in order to control the precision of the results due to the refinement of the mesh, a single geometrical definition of the RVE was used to generate models with different mesh sizes, and compute the elastic properties with different mesh sizes. Each of the meshes is discretized essentially by quadrilateral elements and a small fraction with triangular elements. The homogenized properties corresponding to each mesh and the relative error, with regard to the most refined mesh, are given in Tables 6.2 and 6.3.

TABLE 6.2: Homogenized elastic parameters for different mesh sizes.

Mesh	Mesh size	E_1(GPa)	E_2(GPa)	ν_{21}	ν_{12}	G(GPa)
1	1	5.3276	5.3142	0.3256	0.3265	1.9622
2	0.5	5.5128	5.5008	0.3262	0.3269	2.0390
3	0.25	5.6058	5.5893	0.3264	0.3274	2.0693
4	0.125	5.6308	5.6129	0.3268	0.3279	2.0799
5	0.0625	5.6370	5.6193	0.3269	0.3279	2.0828
6	0.03125	5.6388	5.6211	0.3268	0.3279	2.0835
7	0.015625	5.6393	5.6216	0.3268	0.3279	2.0837

TABLE 6.3: Estimated error for the elastic properties considering mesh 7 as reference.

Mesh	Mesh size	%Error E_1	%Error E_2	%Error ν_{21}	%Error ν_{12}	%Error G
1	1	5.5265	5.4672	0.3670	0.4295	5.8306
2	0.5	2.2432	2.1481	0.2021	0.2991	2.1446
3	0.25	0.5946	0.5740	0.1307	0.1514	0.6937
4	0.125	0.1507	0.1544	0.0101	0.0064	0.1817
5	0.0625	0.0413	0.0412	0.0037	0.0035	0.0432
6	0.03125	0.0082	0.0082	0.0004	0.0004	0.0089
7	0.015625	0.0000	0.0000	0.0000	0.0000	0.0000

Mesh 6 was selected to perform the tests of this section, attending to the trade-off between precision and calculation time obtained. The selected mesh and a detail of it, are depicted on Figures 6.3 and 6.4 respectively.

6.3.3 Analytical models and bounding limits

In order to assess the liability of the results, the Hashin-Shtrikman[69] models were employed. Expression (6.3) considers an extreme situation, where the phases of the materials have a "series arrangement", which provides a lower limit E_s for the elasticity modulus. On the other hand, expression (6.4) considers the other extreme situation, where the phases of the materials have a "parallel arrangement", that provides an upper

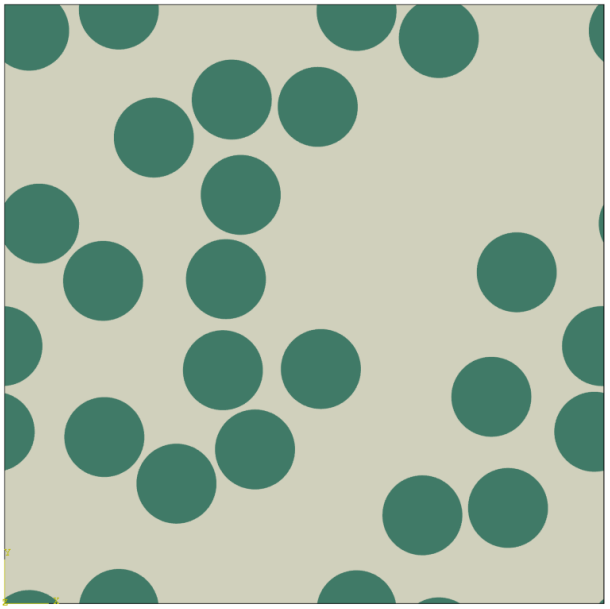

FIGURE 6.3: Periodic model used to test the influence of the mesh on the homogenization.

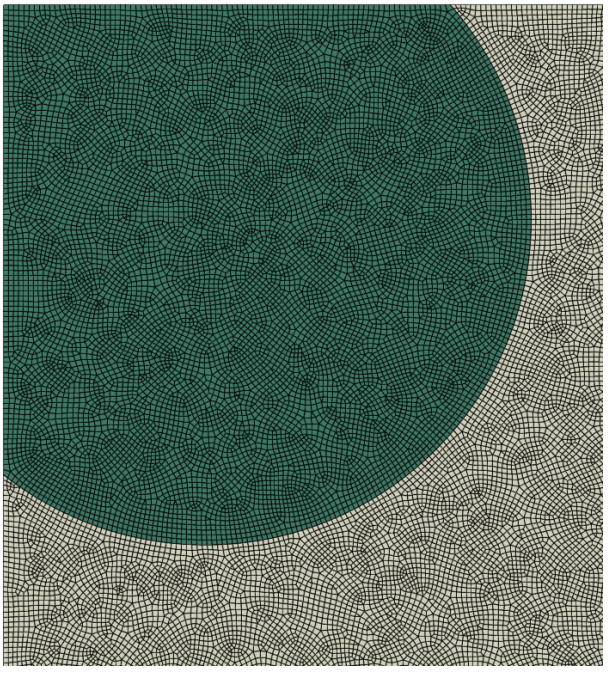

FIGURE 6.4: Detail of the mesh 6 in the model (1 060 812 elements CPS4R, 32 580 elements CPS3, 1 079 025 nodes).

value E_p for the elasticity modulus.

$$E_s = \left[\frac{V_i}{E_i} + \frac{1 - V_i}{E_m}\right]^{-1}, \tag{6.3}$$

$$E_p = E_i V_i + E_m(1 - V_i). \tag{6.4}$$

In expressions (6.4) and (6.3), index i stands for the inclusions and the index m stands for matrix. The scalar V represents the volume fraction while E represents the elasticity modulus. For a better approximation, the classic Halpin-Tsai model[70] that estimates the elastic properties was selected. According to this model, a property P can be estimated by:

$$n = \frac{\frac{P_i}{P_m} - 1}{\frac{P_i}{P_m} + \xi}, \tag{6.5}$$

$$P = P_m \frac{1 + \xi\, n\, V_i}{1 - n\, V_i}. \tag{6.6}$$

In expressions (6.5) and (6.6), P is an arbitrary property to estimate (e.g. elasticity modulus or Poisson ratio) and n is a temporary variable. The parameter ξ is a fitting factor, which usually takes the value of 1 if P is the elasticity modulus, or 2 if P is the Poisson ratio.

Table 6.4, lists the overall elastic parameters, computed for the material described in 6.3.1, considering different numerical and analytic calculation techniques.

TABLE 6.4: Estimation of the parameters according to the analytical models Hashin-Shtrikman[69] and Halpin-Tsai[70].

Parameter	Value	
E (GPa)	H-S Lower limit	4.695
	H-S Upper limit	24.545
	Halpin-Tsai ξ=1	5.879
	Halpin-Tsai ξ=2	6.930
	Numerical model E_1	5.639
	Numerical model E_2	5.622
ν	Halpin-Tsai ξ=1	0.2971
	Halpin-Tsai ξ=2	0.3000
	Numerical model ν_{21}	0.3268
	Numerical model ν_{12}	0.3279

6.4 Distribution fitting

The homogenized elastic properties of an RVE, based on disk inclusions randomly distributed, are considered as stochastic variables. Since, those properties are usually assumed as normal or Gaussian variables. This hypothesis will be tested in this section. Therefore, 500 samples of RVEs with fixed parameters were generated and the homogenized properties computed, using the framework described in Section 6.2. The results obtained are illustrated in the histograms of Figures 6.5 to 6.9. The main statistics are presented in Table 6.5.

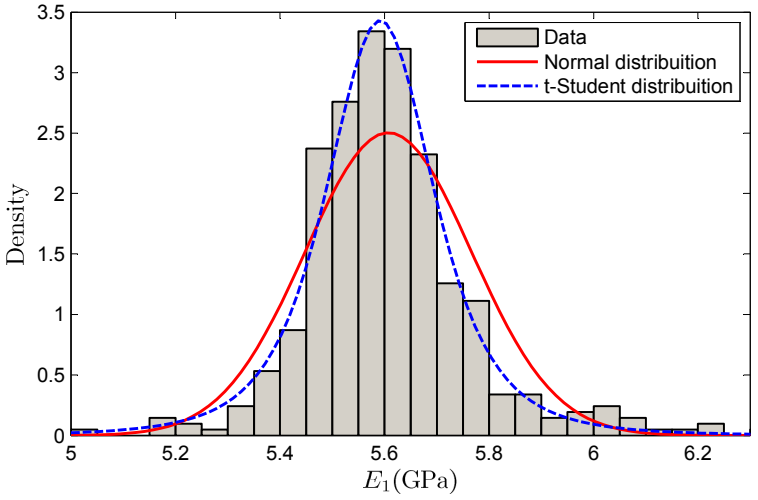

FIGURE 6.5: Homogenized elasticity modulus E_1 for 500 RVEs and fitting distributions.

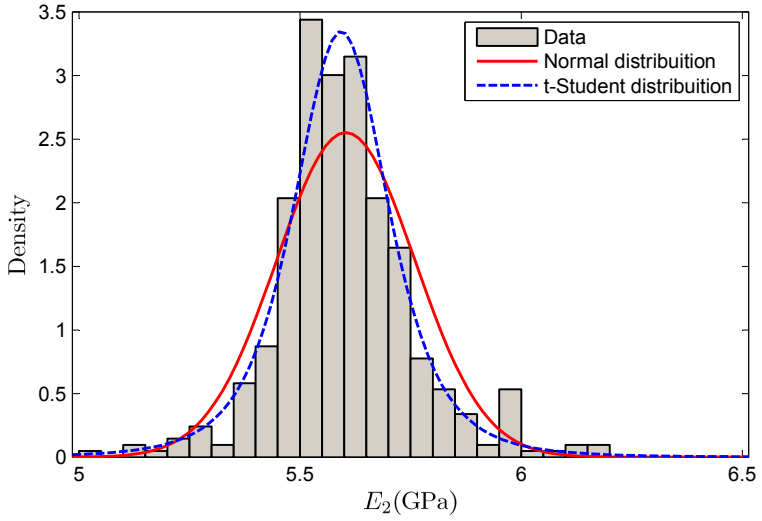

FIGURE 6.6: Homogenized elasticity modulus E_2 for 500 RVEs and fitting distributions.

In order to ensure the correct fitting of the sample results data to the distribution of the random variable, a hypothesis test was performed. The null hypothesis (H_0) considered was the following: the random variable corresponding to a given parameter is described by a certain distribution of probability (Normal and t-Student was tested), in contrast

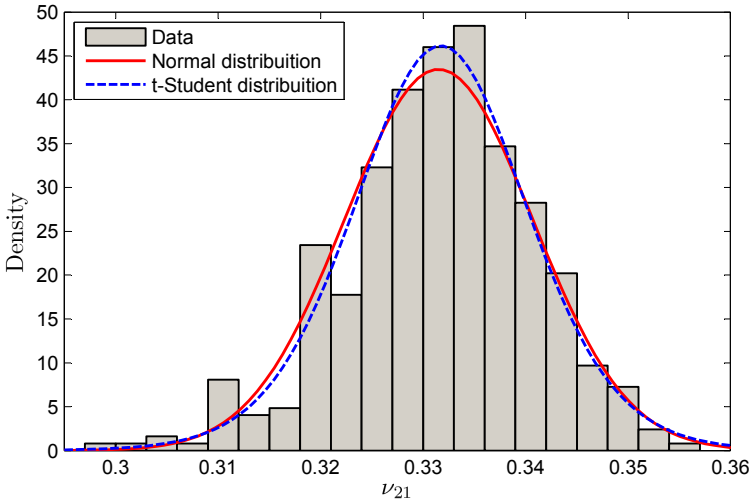

FIGURE 6.7: Homogenized Poisson ratio ν_{21} for 500 RVEs and fitting distributions.

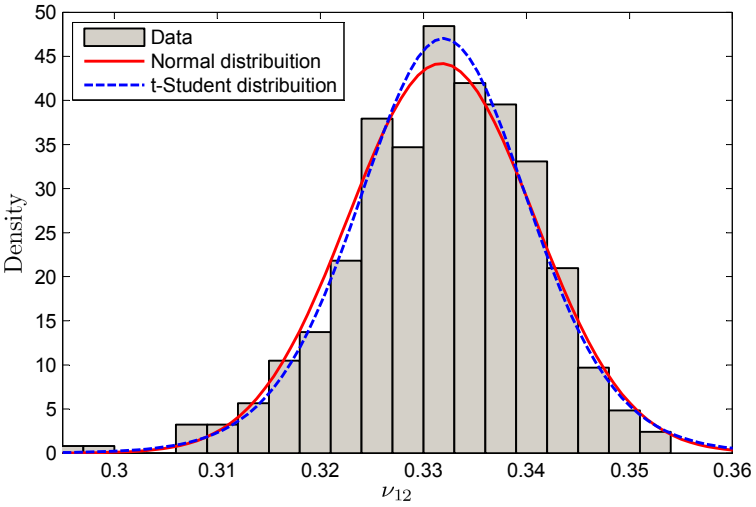

FIGURE 6.8: Homogenized Poisson ratio ν_{12} for 500 RVEs and fitting distributions.

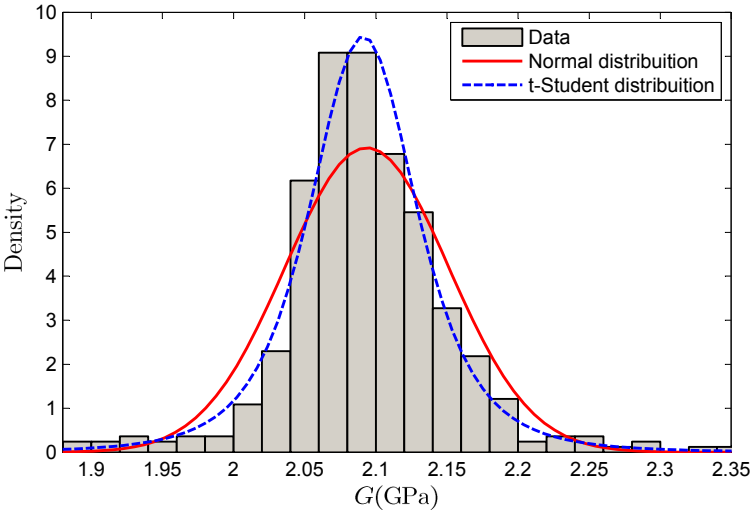

FIGURE 6.9: Homogenized shear modulus G for 500 RVEs and fitting distributions.

TABLE 6.5: Main statistics for the homogenized parameter on a sample size N=500.

Parameter	mean	standard dev.	coef.var.
E1(GPa)	5.603	0.1582	2.82%
E2(GPa)	5.599	0.1555	2.78%
v21	0.3318	0.0092	2.79%
v12	0.3320	0.0090	2.70%
G(Gpa)	2.094	0.0571	2.72%

to the hypothesis that the random variable does not follow that same distribution. The hypothesis test estimates the probability of obtaining such (or more extreme values) than the ones given by the sample results statistics, and considering the null hypothesis true. The χ^2 of good fitting test (see for instance [71]) was used.

The obtained p-values presented in Table 6.6, correspond to the desired probability. For the Normal distribution with regard to E_1, E_2 and G p-values inferior to 5% (significance level α) were obtained, meaning that the null hypothesis can be safely rejected. However, for the Poisson ratio ν_{21} and ν_{12}, the p-value obtained is higher than 5% which does not allow safely rejecting the null hypothesis. For the t-Student distribution the p-values values are all higher than 5%, implying that the null hypothesis cannot be safely rejected, for any of the parameters.

From these results it is possible to conclude that the Normal variable is not appropriate to characterize the distribution of the homogenized Elasticity modulus and Shear modulus. Furthermore, it can be concluded that the t-Student variable can provide a reasonable approximation, better than the Normal variable.

TABLE 6.6: *p-value* obtained for the χ^2 test of good fitting.

variable	*p-value* $H_0 : Normal\ distribuition$	*p-value* $H_0 : t\ distribuition$
E_1	0.00%	7.66%
E_2	0.00%	5.69%
ν_{21}	14.93%	15.57%
ν_{12}	12.84%	10.52%
G	0.00%	15.93%

6.5 Influence of the ratio between the elasticity modulus of the constituents

The ratio between elastic modulus of the fibers and elastic modulus of the matrix, affects the overall homogenized properties. Hence, the dispersion of the homogenized properties

is also expected to vary, with the mentioned ratio. In this section, both of those relations are investigated.

Regarding the RVE described accordingly to the data presented in Table 6.7, four configurations of parameters were considered. Within each RVE configurations of Table 6.7,

TABLE 6.7: RVE parameters, in different set-up configurations.

Configuration	L/R	V_f	E_i (GPa)	ν_i	E_m (GPa)	ν_m
1	20	0.3	varies	0.2	10	0.2
2	20	0.3	varies	0.3	10	0.3
3	20	0.2	varies	0.2	10	0.2
4	20	0.2	varies	0.3	10	0.3

different inclusions elasticity modulus E_i are considered, for a constant matrix elasticity modulus E_m, leading to a variable ratio E_i/E_m.

Regarding each configuration, five random models are generated and then different ratios E_i/E_m are considered. The results obtained for configuration 1, are summarized in Figures 6.10 and 6.11. For the other configurations, the same pattern of behavior was observed. It can be concluded that the predictions of the numerical models are in

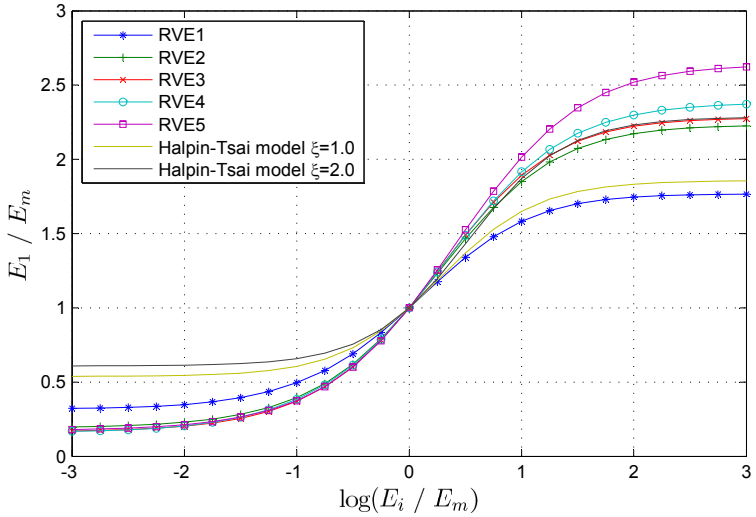

FIGURE 6.10: Evolution of the homogenized elastic modulus E_1 with the ratio E_i/E_m for the base configuration 1 and analytical Halpin-Tsai predictions.

agreement with the Halpin-Tsai model. Furthermore, it is possible to verify that for the Elasticity modulus all curves have the same shape and only intercept at the origin, forming a family. This indicates that fitting parameter ξ is strongly affected by the geometry of the RVE, but it is not (or very weekly so) affected by the elasticity of the constituents. Hence, the Halpin-Tsai model can be used to estimate the dispersion of the homogenized elastic properties when the elasticity modulus of the constituents changes.

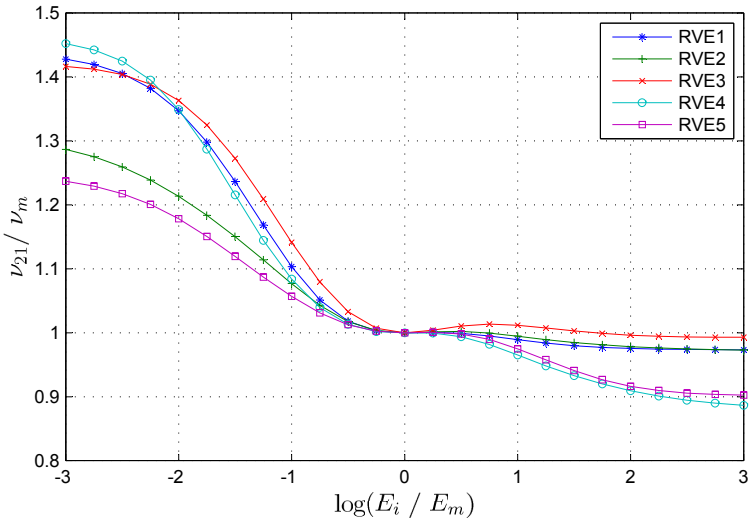

FIGURE 6.11: Evolution of the Homogenized Poisson ratio ν_{21} with the ratio E_i/E_m for the base configuration 1.

6.6 Influence of a thin interface surrounding the inclusions

Many materials have (at a fine scale) a thin interface layer surrounding the inclusions. This happens with concrete aggregates, where a thin layer forms around the aggregates, which is called interface transition zone (ITZ), and is composed by a heterogeneous phase of small particles of cement. In order to provide insight on how this interface layer can affect the overall elastic properties, a study with different layer thickness and stiffness was performed. The objective was to encompass a wide set of possibilities, in order to obtain general conclusions about that effect, and do not rely on a specific material. Realistic properties were assumed for the matrix and volume fractions according to Table 6.8.

TABLE 6.8: RVE properties considered for test the influence of the thin layer.

L/R	V_f	E_m(Gpa)	ν_m	E_i(Gpa)	ν_i	E_l	ν_l
20	0.4	3.35	0.35	74	0.2	varies	0.2

Figure 6.12 depicts the RVE model considered in this section, along with a detail showing the interface layer between inclusions and matrix.

The parameters: ratio between elasticity of the overall RVE and matrix E_1/E_m, ratio between thickness of the interface and radius of inclusions t/R and the decimal logarithm between elasticity on the interface and on the matrix $log(E_l/E_m)$ were considered. These dimensionless variables, were chosen in order to characterize the effect of the interface on the overall stiffness in a general manner, i.e. independently of the material.

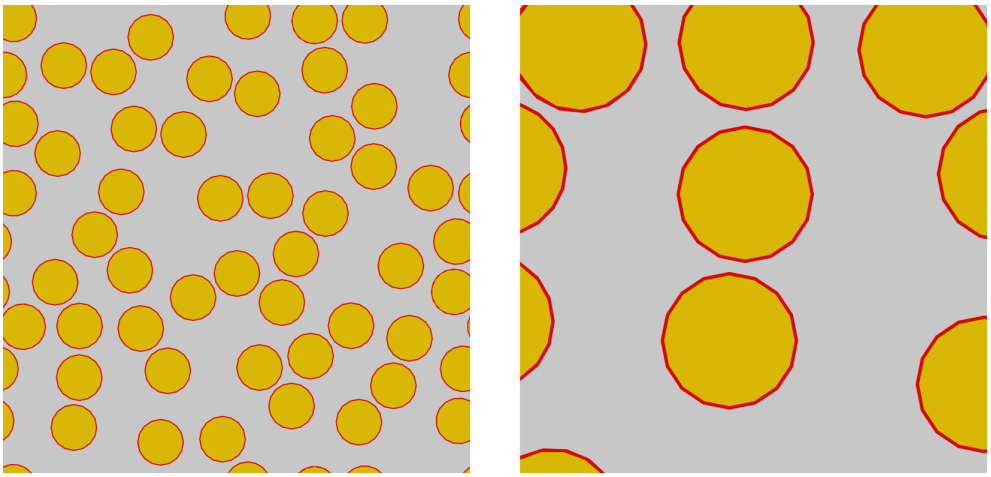

FIGURE 6.12: Geometric model of the RVE (left) and detail of the disk inclusions surrounded by a thin interface layer (right).

The plot in Figure 6.13, relates the RVE overall stiffness (represented by E_1/E_m) with the interface thickness (represented by t/R) and interface stiffness (represented by $log(E_l/E_m)$). Apparently, the overall stiffness relation with the interface parameters is not linear. In fact, the rate of variation of the E_1/E_m increase when t/R and $log(E_l/E_m)$ decrease.

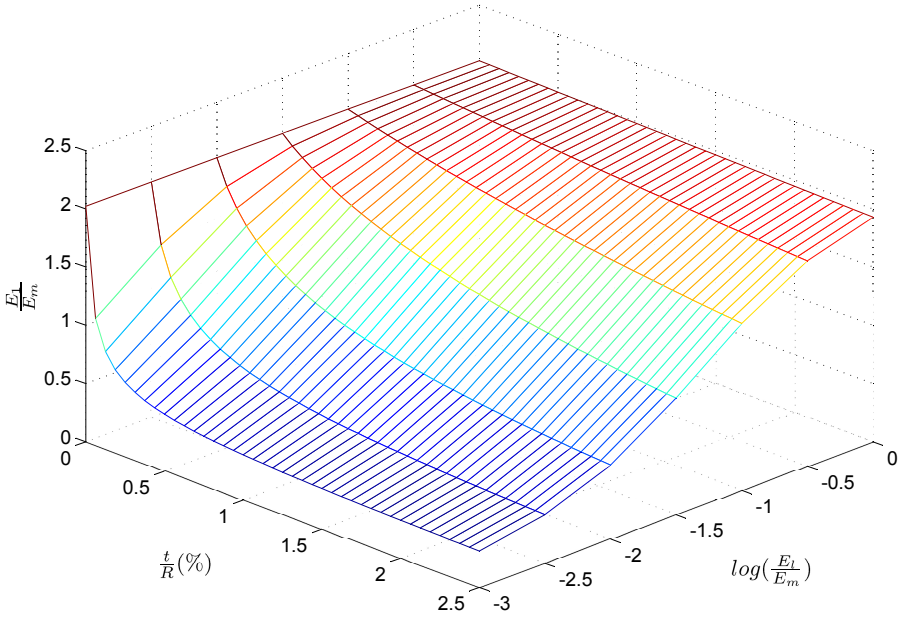

FIGURE 6.13: Influence of the thickness and stiffness of the layer on the overall stiffness of the homogenized material.

It is possible to conclude that, the relation between the overall homogenized Elastic modulus and the parameters of the interface (i.e. elasticity and thickness) is highly non-linear and very sensible to both parameters, especially for lower values of thickness and stiffness. This can be an important factor to consider when performing simplifications

on this type of RVE, using different thickness of the interface layer to replace the real one.

6.7 Numerical Experiments on Three Dimensions

In this section the distribution of the homogenized elastic properties considering two and three dimensional models are compared. Therefore, 30 two dimensional and 30 three dimensional RVE models were generated, and the overall homogenized properties computed. The properties considered for all the RVE models are described in Table 6.9. The

TABLE 6.9: Parameters of the RVE.

L/R	V_f	E_i (GPa)	ν_i	E_m (GPa)	ν_m
15	0.2	74	0.2	3.35	0.35

Figures 6.16, 6.17 and Table 6.10, describe the distributions of homogenized properties for two and three dimensional RVE models. It can be concluded that, the dispersion of homogenized elastic modulus tends to be higher in 2D than in 3D models, attending to the variation coefficient obtained in both cases.

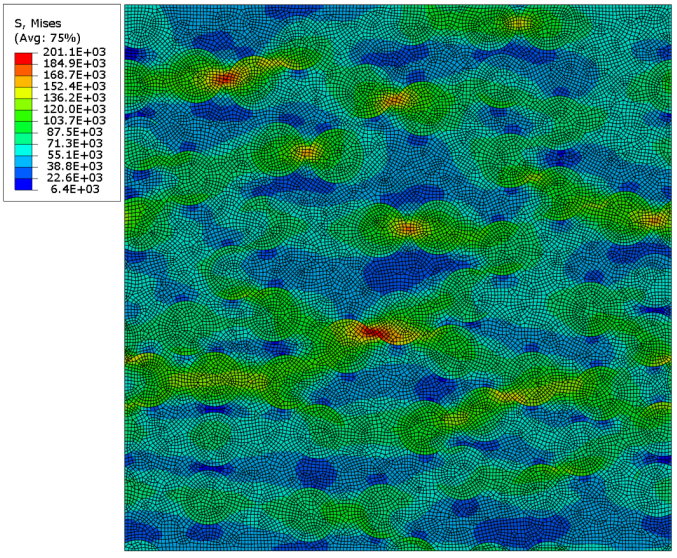

FIGURE 6.14: von Mises stress field obtained for a 2D FEM model.

6.8 Conclusions

A general framework that is able to generate both 2D and 3D FEM models of arbitrary RVEs and also compute homogenized elastic properties was developed. In that

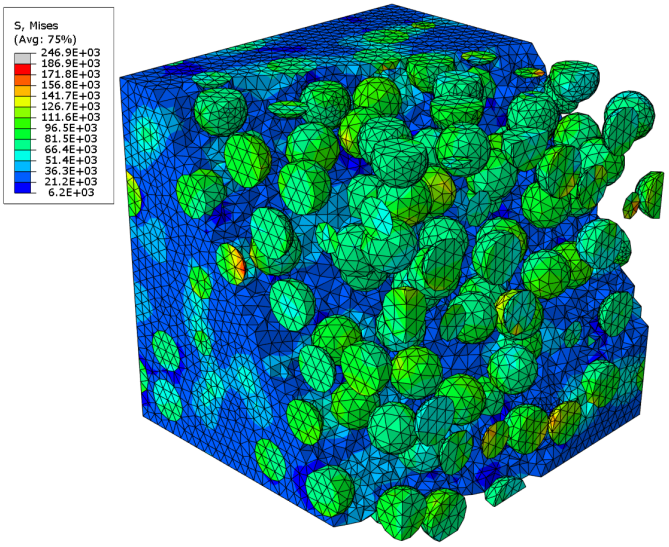

FIGURE 6.15: von Mises stress field obtained on a 3D FEM model.

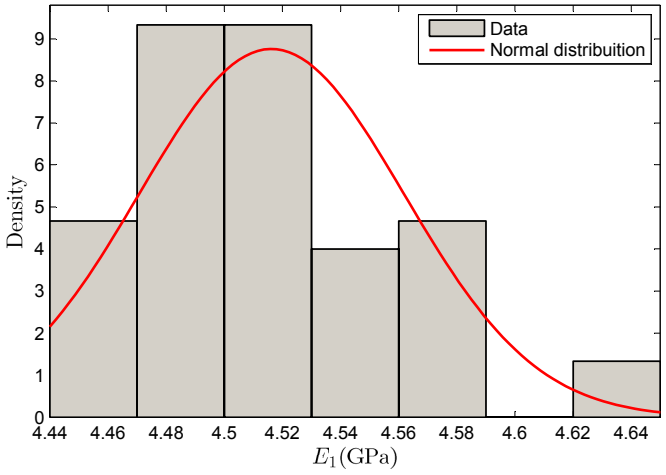

FIGURE 6.16: Histogram for the homogenized Elastic modulus considering 30 RVEs in 2D.

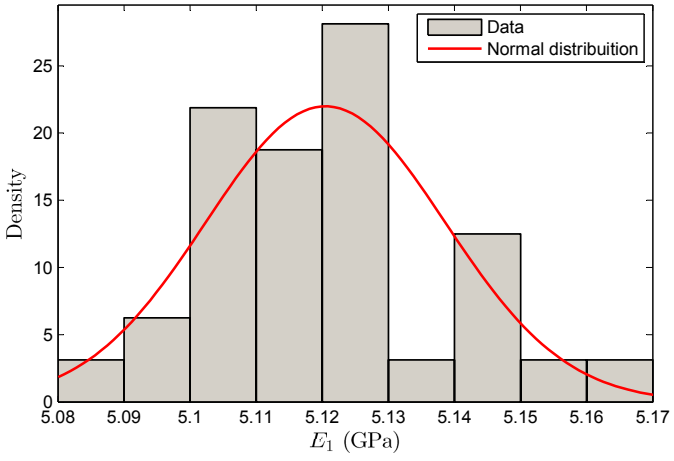

FIGURE 6.17: Histogram for the homogenized Elastic modulus considering 30 RVEs in 3D.

TABLE 6.10: Comparing 2D and 3D main statistics of the homogenized elastic properties for 30 RVE.

		2D	
Parameter	Mean	standard dev.	coef.var.
E_1(Gpa)	4.5162	0.0455	1.01%
ν_{21}	0.3417	0.0048	1.39%
		3D	
Parameter	Mean	standard dev.	coef.var.
E_1(Gpa)	5.1216	0.0182	0.36%
ν_{21}	0.3235	0.0014	0.43%

framework, the geometry of the models is generated using a RSA algorithm. To perform homogenization, the classical periodic boundary condition was employed. The implementation of the framework was achieved with the commercial softwares ABAQUS and MATLAB, using Python and MATLAB scripting languages. The overall homogenized elasticity modulus and Poisson ratio, of a randomly generated 2D RVE based on disk inclusions, was computed employing the numerical framework and two classical analytical models: the Hashim-Shtrikman limits and the Halpin-Tsai equations. The results obtained with the analytical models successfully validated the results obtained with the framework developed.

A total of 500 RVEs under plane strain were generated and the overall elastic properties computed. The generated RVEs are composed by a set of disk inclusions randomly distributed on a uniform matrix. Considering the obtained data and using a hypothesis test, it can be concluded that, the homogenized elastic modulus and shear modulus distributions, do not result from a Normal random variable. It was also determined that for the obtained distributions, a t-Student random variable could be more appropriate than the Normal variable.

The influence of the relation between the elasticity modulus of the materials on the overall homogenized elastic properties random variables was also analysed. The possibility of establishing relationships between those variables and the classical analytical model Halpin-Tsai was investigated. Four types of RVE (plane strain, homogeneous matrix with disk inclusions) were considered and, for each of those types, five different RVEs generated. For each RVE, the ratio between the elasticity modulus of the matrix and the inclusions was changed, accordingly to several different values and the homogenized properties computed. The obtained data shows that the dispersion of the results increases as the ratio between the elasticity modulus differs from 1. Additionally, it can be concluded that for each RVE geometry, the homogenized properties can be fairly predicted using the Halpin-Tsai model. Furthermore, the accurate fitting parameter ξ of that model is essentially influenced by the geometry of the RVE and almost insensitive to the ratio between the elasticity modulus of the constituents. Consequently, the

computational homogenization, can be used to estimate the fitting parameter ξ of the Halpin-Tsai model, considering the RVE geometry, even without a precise definition of the elasticity modulus of the constituents. Therefore, the Halpin-Tsai model can provide a reasonable approximation to the spreading of the homogenized elastic properties when the ratio between the elasticity modulus of the constituents changes.

Regarding RVE overall elastic properties, the sensibility of the obtained values to variations on the interface layer that surrounds the inclusions was investigated. To this end, the same distribution of inclusions was adopted, and variations on the stiffness and thickness were performed on the interface layer, and homogenized elastic properties computed. The results obtained show that the influence of those parameters is nonlinear and there is a very high sensibility of the overall elastic modulus for low values of thickness and stiffness, which can be an important factor to consider when estimating the dispersion of the results of a specific type and size of RVE. It is also important to consider this high sensibility when performing simplifications on this type of models at the interface, using, for instance, different thickness for the interface layer to replace the real one.

In order to compare the distributions of the homogenized elastic properties considering 2D and 3D models, a total of 30 RVEs on 2D(plane strain) and 3D with same volume fraction was generated and analyzed using the framework described in this work. Finally, it was also was possible to conclude that the Normal distribution does not present a good fitting with the results. The dispersion obtained for the 2D models was higher than the one obtained for 3D models.

Chapter 7

Simulation of the Internal Damage Processes and their Effects

7.1 Introduction

In the previous Chapter, some of the relations between the microstructure of the materials and their macroscopic properties were addressed. However no degradation of the materials was considered. Therefore, in this Chapter, material models that can describe damage processes are considered and their consequences discussed. The loss of stiffness in granular structures due to failure mechanisms is generally addressed by two phenomenological approaches: the *discrete crack* models [72],[73] and the *smeared crack* models [74],[75]. While discrete crack models focus on the introduction of macroscopic cracks that disrupt the continuous medium leading to the loss of stiffness, smeared crack models induce the loss of stiffness by introducing a continuous damage field that evolves according to the stress or strain history to represent the underlying dissipative mechanisms. Nevertheless, the constitutive relations developed to capture the internal degradation of the material, can induce strain localization into narrow bands, which can lead to the loss of ellipticity of the governing equilibrium equations after the onset of strain softening, not to mention the size effects [76], that, are not usually described by this type of model.

An alternative approach to study the macroscopic evolution of the damage in granular materials consists in taking into account the microstructural morphology and the interaction between different constituents. For the homogenization, RVEs of the microstructures and homogenization principles were considered according to the previous

Chapters. However the RVEs include, constitutive models for the different phases capable of describing internal degradation processes. The studied material is composed by three phases: a bending matrix, regular inclusions and a very thin interface layer, connecting the inclusions and the matrix. For each of the phases a different constitutive model was considered. Since the interface is very thin and weak, it is modeled considering cohesive elements that allow the possible formation of displacement discontinuities. The inclusions are considered to be hard and were modeled with a simple linear elastic law while the binding matrix was modeled with a damage model developed in this work. However, as stated in Chapter 6, the numerical homogenization of the materials to their macro-scale is highly demanding. This occurs specially, due, to difficulties on accessing the precise geometry, the constitutive laws and their parameters (usually are established for the structural scale) and to, computational limitations, among others.

7.1.1 Outline

The outline of this chapter is the following: in section 7.2, a general overview of the classical phenomenological damage models is described. Then, the implementation of a common damage model is described, and validations of the implementation are detailed. In section 7.3, the cohesive model associated to the interfaces between matrix and inclusions is described. As it will be further detailed, that cohesive constitutive model is expressed in terms of the relation between separation and cohesive forces developed in both tangential and normal directions. In section 7.4 some numerical experiments, regarding the implemented constitutive models, are detailed. Finally, some of the issues related with the numerical experiments and overall conclusions are addressed in section 7.5.

7.2 Damage Models

The use of damage models embedded in the standard continuum mechanics framework, has a long tradition. This field is usually known as *Continuum Damage Mechanics* (CDM). Since the first works of Kachanov[77], Chaboche [78], Lemaitre [79] and others a wide set of models have been proposed to describe the degradation of the materials at the structural scale.

Essentially, the strategy of those models consists in assuming progressive loss of stiffness, due to the formation of voids and micro cracks. Furthermore, those voids and cracks are considered small enough, so that the assumption of material continuity could prevail. Hence, the cracks are described not by discrete discontinuities, but distributed in “smears”. In fact, these types of models are often called “smeared crack models”.

This is formalized as a continuous field of a parameter **D** (called damage), that varies according to the loss of stiffness in each material point of the body. This makes possible that, the damage can be interpreted as a loss of material in terms of resistant volume, and consequent loss of stiffness. This concept can be exemplified by the expression (7.1).

$$\boldsymbol{\sigma} = (1 - D)\, \mathbb{C} : \boldsymbol{\varepsilon} \tag{7.1}$$

In the expression (7.1), $\boldsymbol{\sigma}$ is the stress tensor, $\mathbb{C}$ is a constitutive tensor, and $\boldsymbol{\varepsilon}$ is the strain tensor. The parameter D is a scalar in the range between 0 and 1. The value $D = 0$ corresponds to a damage-free state of the material, while higher values of D correspond to damaged states. The model is complemented by a law that specifies the evolution of D as a function of the strain (or stress) history. It must be noted that, in this simplistic example, the stiffness is assumed to remain always isotropic and consequently, the damage parameter used is a scalar. However, models involving more general assumptions, such as the anisotropic damage and the crack closure effects, can be found in the literature, see for instance [80], [81], [82] and [83].

7.2.1 Limitations of the CDM models

Although, damage models correspond to important advances in describing certain materials, further refinements are undoubtedly required. Such improvements, contemplate situations involving complex strain paths. In fact, deviations from the experimental observations can be expected as the strain paths become more complex.

Another important issue, related with the damage models, is the localization of the damage itself. The material degradation and consequent reduction of stiffness, leads to large strains in the damaged area. However, this damage tends to localize in small areas, depending on the size of the finite element used in the discretization. Indeed, after the damage starts to localize, the problem becomes ill-posed. A typical example that demonstrates the localization is the following:

Consider a horizontal bar of constant section subjected to axial stretching. Hence, all the sections develop the same axial stress because of the equilibrium conditions. If the bar is discretized in small elements, the damage localizes in one row of central elements. Then, the axial stress will be conditioned by the damaged zone. Furthermore, as the stretching progresses, the developed stress will be less than the necessary for the damage onset in the remaining elements. Consequently, after the damage onset the strains in the undamaged elements will decrease, in opposition to the damaged zone where the strains will increase. The described effect leads to larger strain levels in the damaged raw of

elements when the refinement of the mesh increases. This results in the development of less axial stress with thinner refinements of the mesh. Strategies of regularization have been proposed to overcome the localization problem, for instance the crack band model [84], and the use of non-local models. The non-local models can be subdivided in two categories: the integral type (for instance [85]) and the gradient type(for instance [86]).

The crack band model assumes that the dissipated energy per unit of volume due to the formation of the cracks is a constant that depends on the material. This way, the constitutive model use in each element is affected by a parameter called characteristic length, that depends on the element size. The use of crack band model requires experimental determination of additional parameters of the material. Furthermore, the models are valid in a limited range of conditions and strain paths.

The non-local damage models, consider the same assumption that the energy dissipated is a constant of the material. However, this requirement is fulfilled using non-local averaged variables, such as average strains or average damage for instance. In both of integral and gradient types of non-local models, there usually is an important drawback: the interdependency of the calculation points within each other. This interdependency usually results in the multiplication of the calculation time and required resources.

7.2.2 Practical Application of CMD in RVE for Homogenization

Given the described aspects of the CDM, it is important to recall the following limitations in the context of their implementation in the RVEs of the materials:

- some works[87] sustain that first order homogenization cannot resolve large spacial gradients;
- most of the constitutive damage models have been established for use at the structural level;
- damage models have difficulties addressing problems with complex strain paths;
- the characterization of the parameters of the material at the micro scale (on models that have been designed for a different scale), can be difficult or even technically impossible;
- the employment of non-local strategies for regularization, generally introduces adverse complexity to the overall model.

In this work, it was assumed that the interface dominates the damage onset in the RVE, and the development of the damage is essentially conditioned by the dispersion of the

inclusions. Under those assumptions, and in order to avoid the unjustified computational complexities of the homogenization, a simple CMD model was selected to describe the matrix. That model is described in the following subsection.

7.2.3 Damage Model for the RVE Matrix

An isotropic damage model was employed [88] [89], to describe the mechanical behavior of the matrix phase existent in the RVE. The aim of this model was to describe the damage process in concrete type of materials. Therefore, the most significant degradation procedures, occur under the traction stress states.

Another important concept is the effective stress $\boldsymbol{\sigma}$, defined according the expression (7.2).

$$\boldsymbol{\sigma} = \frac{\boldsymbol{\sigma}_0}{(1-D)} \tag{7.2}$$

The symbol $\boldsymbol{\sigma}_0$, represents the stress in the undamaged material. In this expression, the meaning of damage is related with the concept of sectional area reduction due to micro-cracking as a suitable measure of the state of internal damage. In this context, when denoting respectively A_0 and A to the effective load bearing areas of the virgin and damaged materials, the damage variable can be written as in the expression (7.3).

$$D = \frac{A - A_0}{A} \tag{7.3}$$

The scalar damage parameter D ranges from 0 for the virgin material to 1, which represents the failure (zero stress) under homogeneous strain condition. This formulation is in agreement with the expression (7.1), that we recall here for convenience.

$$\boldsymbol{\sigma} = (1-D)\,\mathbb{C} : \boldsymbol{\varepsilon} \tag{7.4}$$

In the framework of thermodynamics, the free energy function is defined in the expression (7.5).

$$\psi(\boldsymbol{\varepsilon}, D) = (1-D)\,\frac{1}{2}\boldsymbol{\varepsilon} : \mathbb{C} : \boldsymbol{\varepsilon} \tag{7.5}$$

In fact, free energy ψ, is related with the stress tensor $\boldsymbol{\sigma}$ according the expression (7.6).

$$\boldsymbol{\sigma} = \frac{\partial \psi}{\partial \boldsymbol{\varepsilon}} \tag{7.6}$$

Nevertheless, the energy release rate Y and the free energy ψ are related according to the expression (7.7).

$$Y = \frac{\partial \psi}{\partial D} \tag{7.7}$$

The constitutive model is complemented by a damage threshold criterion and a damage evolution law, described forward.

7.2.3.1 Damage Threshold

The damage threshold criterion, defines a limit surface in the strain space, where the damage parameter starts to evolve. In order to describe this criterion, the equivalent strain $\tilde{\varepsilon}$ is defined. The equivalent strain is a scalar function of the strain tensor according to the expression (7.8).

$$\tilde{\varepsilon} = \frac{1}{E} \max \langle \boldsymbol{\sigma}^p \rangle_+ \tag{7.8}$$

In the expression (7.8), E is the elasticity modulus of the material and $\boldsymbol{\sigma}^p$ is a tensor containing the principal stress components of the effective stress. The operator $\langle \cdot \rangle_+$, also known as Macaulay brackets, is defined according to expression (7.9).

$$\langle x \rangle_+ \quad = \quad \max\{0, x\} \tag{7.9}$$

When applied to a tensor, the operator $\langle \cdot \rangle_+$ replaces the negative components of that tensor with zeros.

The function that defines the damage threshold (inspired in the St. Venant criterion of maximum principal strain) may be defined by the expressions (7.10) and (7.11).

$$\Phi(\tilde{\varepsilon}, \kappa) = \tilde{\varepsilon}(\varepsilon) - \kappa \tag{7.10}$$

$$\kappa = \max\{\kappa_0, \max(\tilde{\varepsilon})\} \tag{7.11}$$

This way, the scalar κ, represents the maximum value of the equivalent strain history after achieving the initial damage threshold κ_0. The initial damage threshold κ_0 is given by the expression (7.12).

$$\kappa_0 = \frac{f_t}{E} \tag{7.12}$$

In (7.12), f_t is a material parameter indicating the maximum tensile strength.

7.2.3.2 Damage Evolution

When the damage criterion is fulfilled ($\Phi(\tilde{\varepsilon}, \kappa) = 0$), the damage variable can evolve. The damage D is a function of the state variable κ, which in turn is a function of the strain history, described by the state variable κ, according to the expression (7.13).

$$D(\kappa) = \begin{cases} 0 & \text{if } \kappa \leq \kappa_0 \\ 1 - \frac{\kappa}{\kappa_0} \exp\left(-\frac{\kappa - \kappa_0}{\varepsilon_f - \kappa_0}\right) & \text{otherwise} \end{cases} \tag{7.13}$$

In the expression (7.13), ε_f is a material parameter related with the damage initiation.

7.2.3.3 Regularization

As mentioned in the section 7.2, the common damage models suffer from localization and mesh dependency problems. In order to gain objectivity and avoid the aforementioned problems a regularization based on Crack Band Model [84] is used. This model assumes that the cracks develop in bands of one-element tick and a constant specific fracture energy of fracture Ψ. The specific fracture energy is defined to be the fracture energy G_f developed due to cracking per unit of volume.

Therefore, a parameter called characteristic length l^e, that represents the element size, is introduced in the constitutive model in order to guarantee the, constancy of the specific fracture energy. For the presented damage model to comply with the mentioned criterion, the parameter ε_f from equation (7.13) is replaced by a counterpart ε_{f2}, calculated according to expression (7.14).

$$\varepsilon_{f2} = \frac{\lambda}{l^e}(\varepsilon_f - \frac{\kappa_0}{2}) + \frac{\kappa_0}{2} \tag{7.14}$$

In the equation (7.14), λ is a material parameter corresponding to the width of the damage zone.

7.2.4 Computational implementation of the Damage model

As described in Chapter 2, the computational implementation of the FEM using the Newton-Raphson algorithm (Table 2.1) requires, a procedure for updating the stress state in the material and the definition of the consistent tangent operator. The consistent tangent operator is defined in the expression (7.15).

$$\mathbf{C} = \frac{\partial \boldsymbol{\sigma}(\boldsymbol{\varepsilon}, \boldsymbol{\alpha})}{\partial \boldsymbol{\varepsilon}} \tag{7.15}$$

For the Mazars model the $\mathbf{C}$ can be simply approximated using the expression (7.16).

$$\mathbf{C} = \frac{\partial (1 - D)\, \mathbb{C} : \boldsymbol{\varepsilon}}{\partial \boldsymbol{\varepsilon}} \approx (1 - D)\, \mathbb{C} \tag{7.16}$$

The procedure summarized in Table 7.1 is employed in each calculation point, to determine the stress update, regarding the expressions (7.1) and (7.8) to (7.14).

TABLE 7.1: State update algorithm for the damage model.

---

(1) Verify if the time step n is initial.
if $n = 0$ **then**
  Initialize ε_{f2} using (7.14)
  $\kappa = \kappa_0$
  $D = 0$
end if

(2) Update the undamaged stress tensor $\boldsymbol{\sigma}_0 = \boldsymbol{\sigma}_0^{n+1} = \boldsymbol{\sigma}_0^n + \mathbb{C} : \Delta\boldsymbol{\varepsilon}$.

(3) Perform spectral decomposition of $\boldsymbol{\sigma}_0$ to obtain the principal stress components $\boldsymbol{\sigma}^p$.

(4) Evaluate the equivalent strain $\tilde{\varepsilon}$ using (7.8).

(5) Verify if the damage threshold is achieved.
if $(\tilde{\varepsilon} - \kappa) > 0$ **then**
  $\kappa = \tilde{\varepsilon}$
  $D = 1 - \frac{\kappa}{\kappa_0} \exp\left(-\frac{\kappa - \kappa_0}{\varepsilon_{f2} - \kappa_0}\right)$
end if

(6) Compute the stress tensor $\boldsymbol{\sigma}^{n+1} = \boldsymbol{\sigma}$ using (7.2).

7.2.5 Verification of the Damage model

In order to ensure the proper implementation of the damage model, and to verify if mesh dependency and localization may occur, two tests were performed: a test with one element and open-hole tensile test. In those testes the specific energy due to the cracking, should remain constant in order to validate the regularization Crack Band Model.

One element test

The damage model and parameters of the matrix mentioned on Table 7.2 were considered, for three different simulations. Each simulation was performed with a single squared plane stress element with different edge length. The edge sizes considered were 50, 100 and 250 mm. The element was fixed on the left border nodes, while subjected to a prescribed displacement in the horizontal direction causing elongation until total loss of resistance. The relation between displacement and the reaction force developed is described in Figure 7.1.

TABLE 7.2: Material properties for the damage model.

E_m	ν_m	f_t	λ	ε_f
10.0 Gpa	0.25	30.0 MPa	4.0 m	7.50E-03

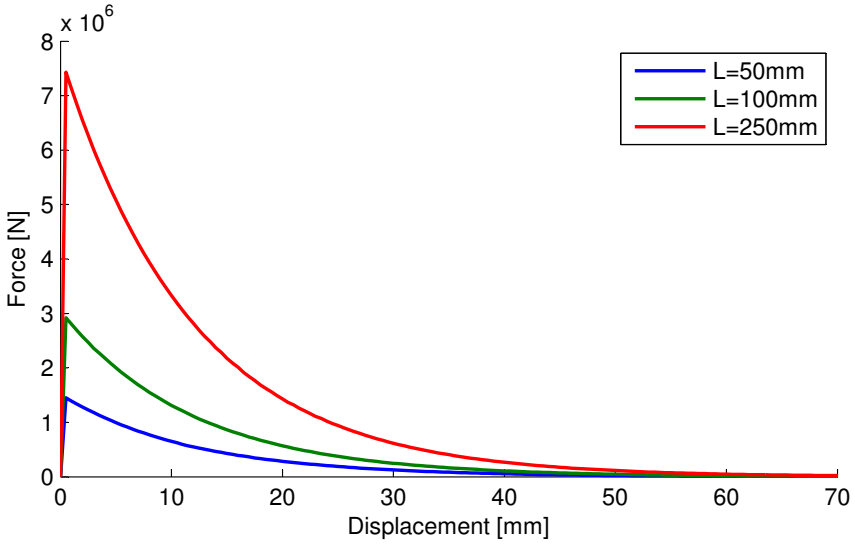

FIGURE 7.1: Force developed considering different element sizes.

The fracture energy G_f correspondent to each of the simulations, can be computed as the area under the force versus displacement diagrams. While the specific fracture energy Ψ is obtained dividing the fracture energy by the characteristic length l^e of the element,

according to the expression (7.17).

$$\Psi = \frac{G_f}{l^e} \tag{7.17}$$

The specific fracture energy, in correspondence to each of the simulations, is presented in Table 7.3.

TABLE 7.3: Specific fracture energy obtained for the different element sizes.

L[mm]	$\Psi[J]$
50	2.517E+08
100	2.514E+08
250	2.542E+08

It is possible to verify that the specific energy does not vary more than 1%, which is consistent with a correct implementation of the model.

Open-hole tensile test

A simple bar specimen with a hole in the center, represented in Figure 7.2 was considered. The specimen is clamped in the left border while a horizontal displacement is progressively imposed in the right border.

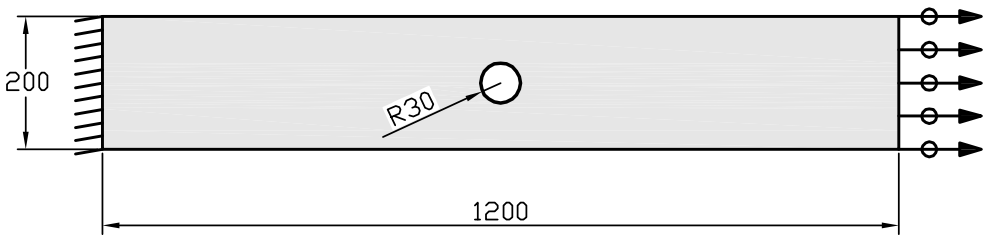

FIGURE 7.2: Geometry of the tension specimen and boundary conditions (dimensions in mm).

The test was simulated using three models with different mesh refinements. The average characteristic lengths of the elements in each of the models are 28.3, 14.1 and 8.5mm. The tensile force developed in each model is described by the diagram depicted in Figure 7.3.

Apparently the curves from the force displacement diagram are similar, which implies the release of approximated the same specific fracture energy for all the meshes.

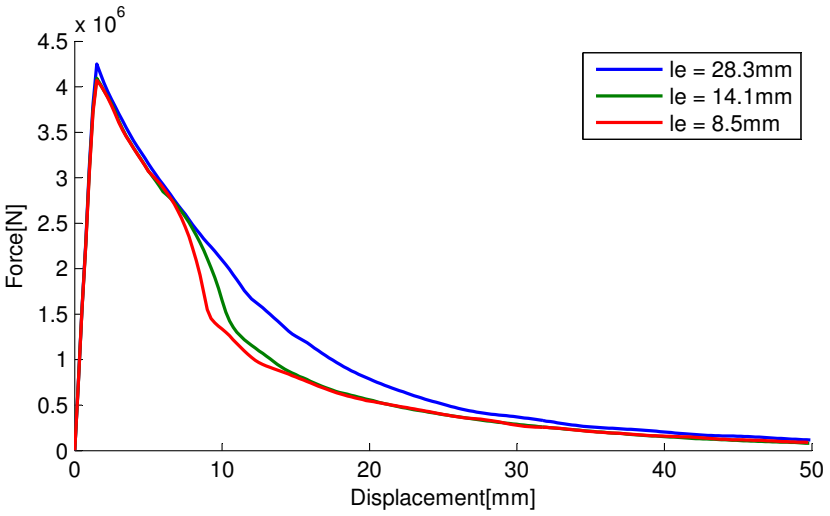

FIGURE 7.3: Force developed considering different meshes.

7.3 Cohesive Models

In some composite materials, the connection between the different phases, i.e. the interface, can be an important source of fragility. Regarding for instance, the unidirectional carbon and fiber reinforced composites with polymers, some studies ([90], [91]), indicate that strength of the material under transverse compression is mainly influenced by the strength of the fiber-matrix interface.

In order to describe the possible development of discontinuities between the matrix material and the inclusions, cohesive elements provided by the FEM software ABAQUS were used. The cohesive elements (COH2D4 [92]) can be used to describe a thin layer between different phases and its constitutive response. Since, generally, the thickness of the layer is difficult to determine, the constitutive relation is given in terms of traction force t (per unit area) and the separation δ between the phases.

A general, explanation regarding the type of constitutive law, employed is described forward, however a more detailed explanation can be found in [92], [93] and [94].

The diagram represented in Figure 7.4 describes the constitutive relation for the cohesive elements, when the separation and traction force only develops in the direction normal to the layer (mode I).

In Figure 7.4, N represents the maximum traction force developed, δ_0 represent the maximum displacement allowed without reduction of stiffness. After the displacement δ^0 is achieved, the developed traction decreases until vanishing when the separation reaches δ^f. The parameter K corresponds to the initial slope N/δ^0 and represents the initial stiffness. Often, the degradation of the material is so abrupt, that δ^0 and δ^f tend

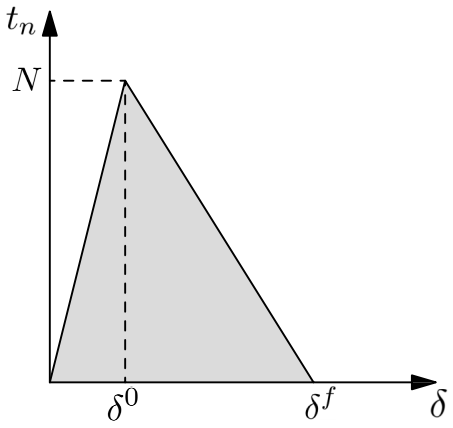

FIGURE 7.4: Traction-separation diagram for cohesive elements.

to coincide. However this can create numerical problems. Hence, the difference between δ^0 and δ^f in the model can often be considered a numerical penalty parameter. The fracture energy G_c, is defined in the expression (7.18).

$$G_c = \int_0^{\delta^f} t_n(\delta) d\delta = \frac{1}{2} N \, \delta^f = 1 \tag{7.18}$$

Since, the diagram is bi-linear and contains the origin, the parameters K, N and G_c are enough to define constitutive law.

Taking that under consideration, the traction force can develop simultaneously in the normal and tangential directions, laws for mixed modes for failure and damage are required. Among the available criterions in the literature and implemented on ABAQUS are the maximum stress criterion and the quadratic failure criterion. The maximum stress criterion is defined in expression (7.19).

$$\max \left\{ \frac{\langle t_n \rangle_+}{N}, \frac{t_s}{S} \right\} = 1 \tag{7.19}$$

The quadratic failure criterion is defined in expression (7.20).

$$\left(\frac{\langle t_n \rangle_+}{N} \right)^2 + \left(\frac{t_s}{S} \right)^2 = 1 \tag{7.20}$$

In the previous expressions (7.19) and (7.20), t_n and t_s are the normal and tangential traction components, while N and S represent the maximum allowed, traction components in the normal and tangential directions. The operator $\langle \cdot \rangle_+$, was defined in

expression (7.9). The evolution of damage is controlled by the effective displacement $\bar{\delta}$, given in expression (7.21).

$$\bar{\delta} = \sqrt{\langle \delta_n \rangle_+^2 + \delta_s^2} \tag{7.21}$$

The variables, δ_n and δ_s represent the normal and tangential components of the displacement vector. Hence, if the damage criteria is fulfilled, the damage D evolution is computed as function of maximum effective displacement $\bar{\delta}^{\max}$ according to expression (7.22).

$$D(\bar{\delta}^{\max}) = \frac{\bar{\delta}^f(\bar{\delta}^{\max} - \bar{\delta}^0)}{\bar{\delta}^{\max}(\bar{\delta}^f - \bar{\delta}^0)} \tag{7.22}$$

The symbols $\bar{\delta}^0$ and $\bar{\delta}^f$ represent the minimum displacement for damage initiation and the displacement corresponding to the complete failure of the material, respectively. Finally the traction separation is given by the expressions (7.23) to (7.25).

$$t_n = (1 - D)K_n\delta_n \quad \text{if} \quad \delta_n > 0 \tag{7.23}$$

$$t_n = K_n\delta_n \quad \text{if} \quad \delta_n \leq 0 \tag{7.24}$$

$$t_s = (1 - D)K_t\delta_s \tag{7.25}$$

In the previous equations (7.23) and (7.24), K_n and K_t represents the stiffness of the undamaged material, for the normal and tangential direction respectively. It must be taken under consideration that, when the normal compression develops, no limitation is imposed to the maximum traction force allowed. Furthermore, the effect of normal compression is disregarded in the criterion for damage initiation.

7.4 Numerical Results

7.4.1 Model and material parameters

As mentioned previously, the material microstructure is composed by a dispersion of circular inclusions in a bending matrix. Then, three phases are considered: the bending matrix, the inclusions and a thin interface layer between matrix and inclusions.
The matrix described by the continuous damage model detailed in Section 7.2.3 and the inclusions are described with a linear elastic model. The parameters used for those

models are given in Table 7.4. Regarding the parameters of Table 7.4, the index m

TABLE 7.4: Material properties for matrix and inclusions.

Matrix					Inclusions	
E_m	ν_m	f_t	λ	ε_f	E_i	ν_i
10.0 Gpa	0.25	30.0 MPa	4.0 m	7.50E-03	200.0 GPa	0.30

stands for matrix, and the index i stands for inclusions. Furthermore, the thin interface between matrix and inclusions is described by the cohesive model detailed in Section 7.3 and the correspondent parameters given in Table 7.5.

TABLE 7.5: Properties of the interface cohesive material.

δ^0	N	S	G_c
1.0mm	4.0e6N/m	4.0e6N/m	10e3 J

7.4.2 Mesh Refinement

A parametric test on the sensitivity of the simulations to the mesh refinement was conducted. The objective was, to reduce adverse numerical errors and to simultaneously guarantee an affordable computation time. To accomplish this task, four models of the same RVE were generated. Subsequently, the models were subjected to periodic boundary conditions correspondent to a tension strain. Finally, the homogenized stress-strain curves, obtained for each mesh refinement, are compared.

The RVE was randomly generated, using the algorithm described in Chapter 5 and considering an edge size of 12 times the inclusion diameter and a volume fraction of 45%. The material properties of the phases are given in Table 7.4 and Table 7.5. Figure 7.5, provides a detail of the refinement for the different meshes considered. The average element length, number of elements and number of nodes used for each mesh refinement are provided in Table 7.6.

TABLE 7.6: Meshes used on each model.

	Element Lenght	No. Elements	No. Nodes
MESH1	0.3	2371	2398
MESH2	0.2	5449	5484
MESH3	0.1	18635	18638
MESH4	0.08	29147	29058

According to the simulations a major crack developed in a direction normal to the loading. This is apparent in Figure 7.6, which describes the damage field obtained with

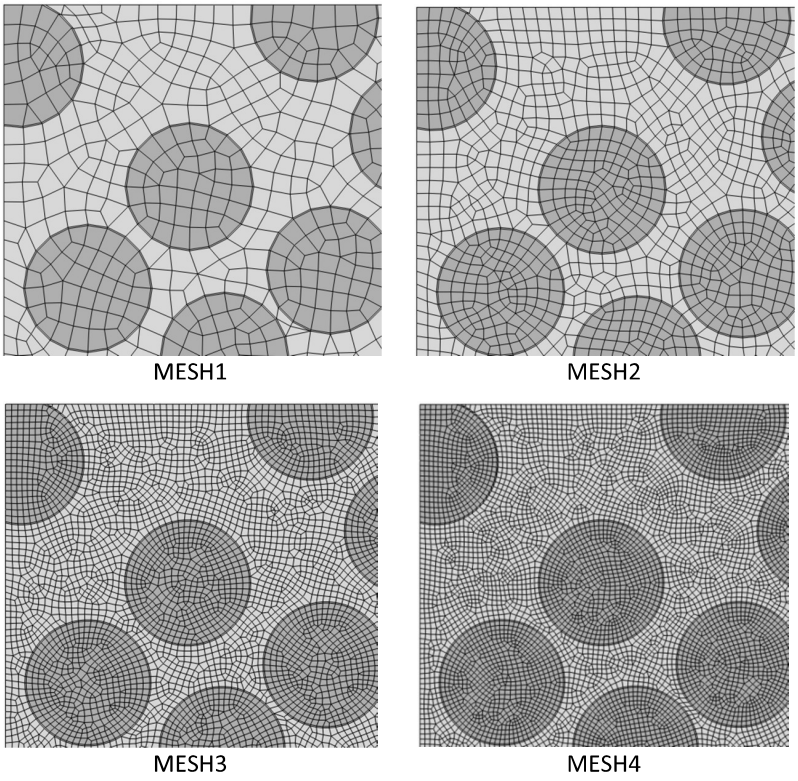

FIGURE 7.5: Detail of the refinement used in the meshes.

MESH3 at the maximum strain applied. The same pattern was observed for other mesh refinements.

Figure 7.7, depicts the relation between the homogenized stress component σ_{11} and the imposed strain ε_{11}, regarding the diferent mesh sizes. Table 7.7, indicates the maximum value of σ_{11} obtained for each mesh size, and compares those values in terms of relative error (considering σ_{11} for *MESH4* as exact).

TABLE 7.7: Maximum homogenized stress σ_{11} obtained for each mesh.

	σ_{11}^{max} [Mpa]	Relative error[%]
MESH1	5.578	4.05
MESH2	5.404	0.80
MESH3	5.303	1.08
MESH4	5.361	0.00

The obtained results, show that the three most refined meshes, provided similar results. Therefore, the mesh type *MESH3*, was selected to perform the computations in the remaining examples.

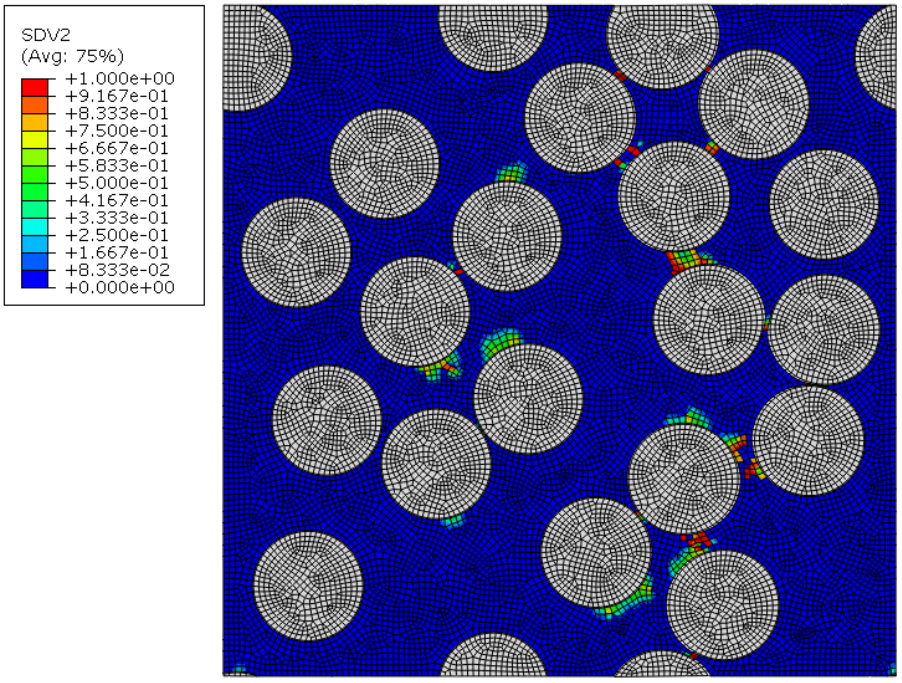

FIGURE 7.6: Contour of the Damage variable for *MESH3*.

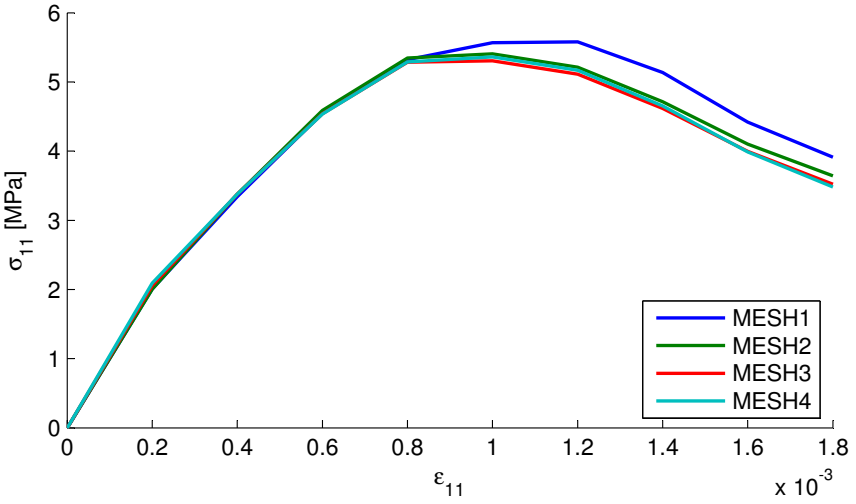

FIGURE 7.7: Homogenized stress component σ_{11} obtained for a tensile strain ε_{11}.

7.4.3 Homogenized stress in RVE with internal damage

Several realizations of RVEs were monotonically subjected to periodic boundary conditions, corresponding to different strain tensors: simple traction, compression and compression combined with traction. The objective was to evaluate the homogenization strategy of the overall material, and characterize damage patterns, which develop in the micro structure.

7.4.3.1 Tensile strength

To access the tensile strength, five realizations of RVE, were monotonically subjected to periodic boundary conditions, corresponding to a simple traction elongation in the horizontal direction. A contour plot of the damage pattern obtained is represented Figure 7.8. In Figure 7.8, a formation of cracks distributed in the interface of the

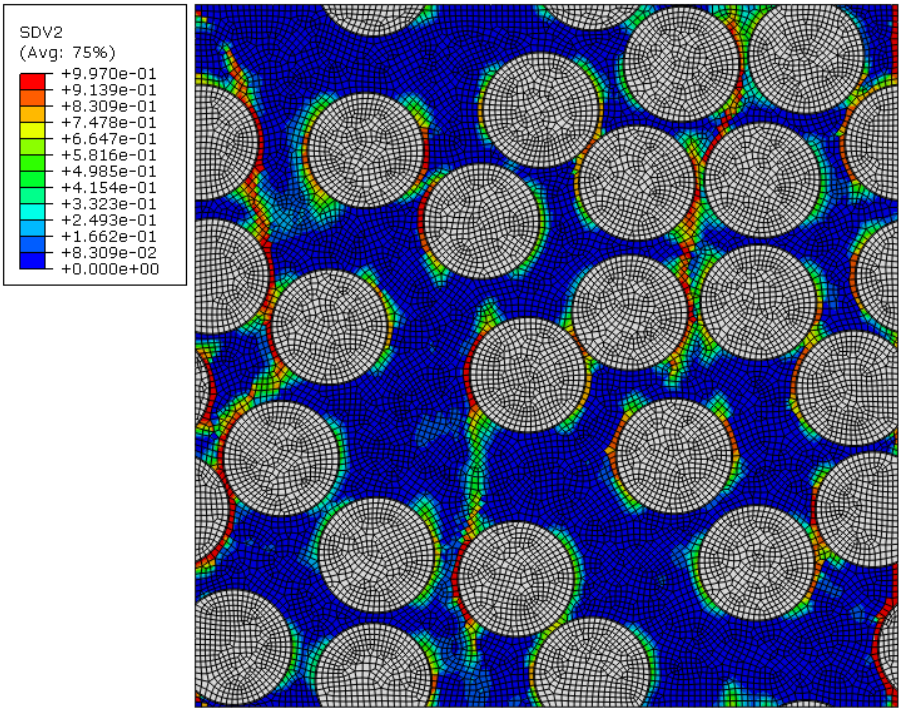

FIGURE 7.8: Damage pattern obtained under simple traction.

materials is apparent and oriented in a direction normal to the loading. Furthermore, some of the cracks in the center are merged and form a continuous band that leads to the failure of the material. The stress strain curves obtained for the different realizations are depicted in Figure 7.9.

The stress strain curves start to diverge after the damage onset. However, the maximum straight obtained for the different realizations, varies in a relatively small range around 25MPa.

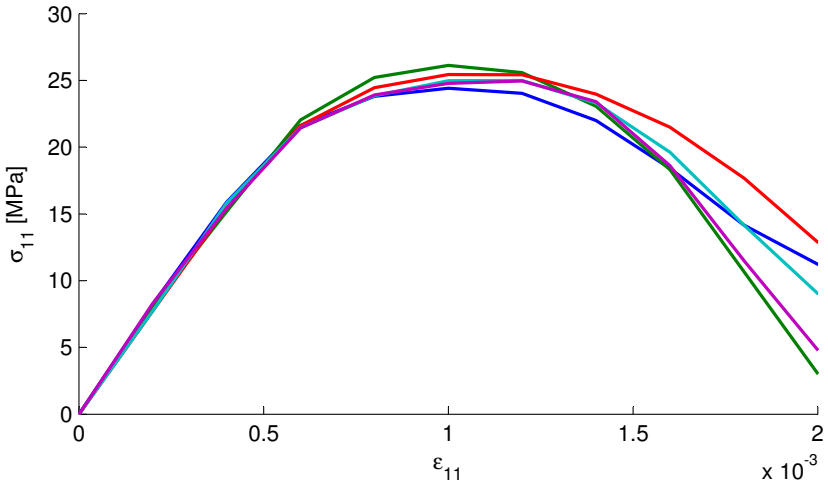

FIGURE 7.9: Stress strain curves under traction, for 5 RVE realizations.

7.4.3.2 Compression strength

The evolution of the damage was evaluated for five RVE realizations using a similar procedure as the one previously described for traction. The contour plot of the damage pattern obtained is represented in Figure 7.10. Here, it is visible a major crack band

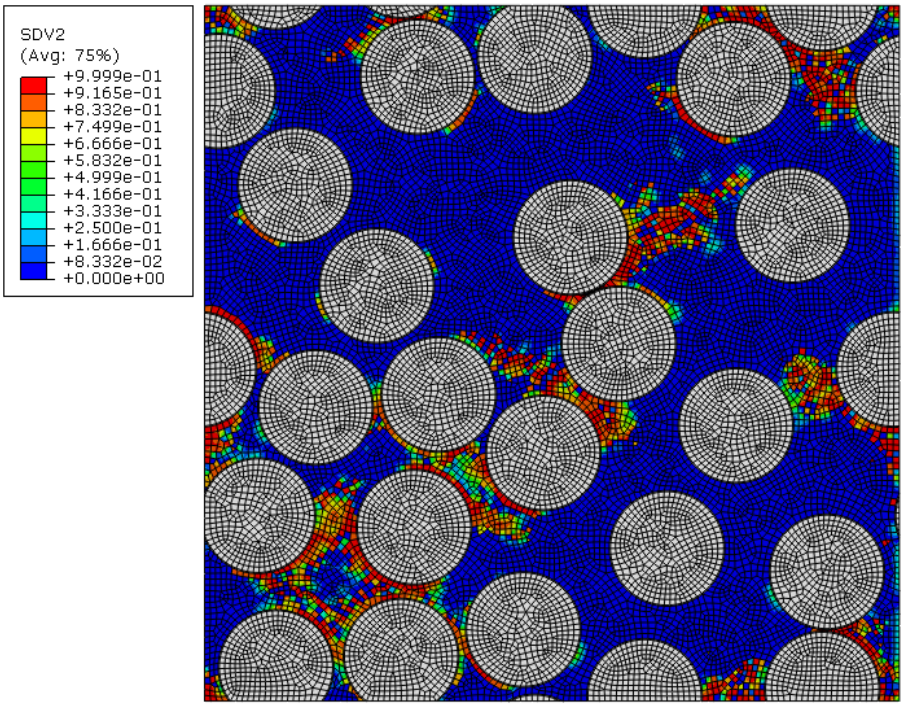

FIGURE 7.10: Damage pattern obtained under simple compression.

that forms an approximate angle of 45°with the loading direction. The stress strain relation obtained for each of the realizations is depicted in Figure 7.11.

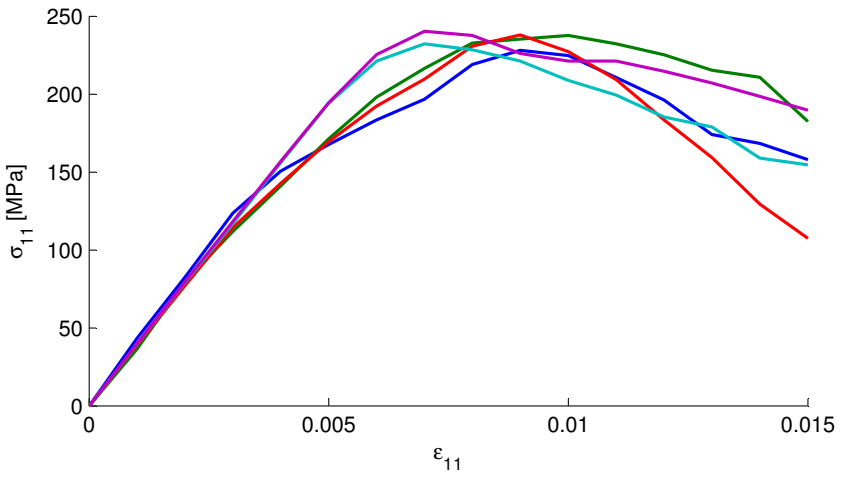

FIGURE 7.11: Stress strain curves under compression, for five RVE realizations.

Similarly to the traction loading, the stress strain curves tend to diverge after the damage onset. However, apparently in compression the divergence is more pronounced than in the traction case. This might indicate that the distribution of the inclusions, have more influence in the damage evolution for the compression case when compared with the traction.

As expected, the maximum straight under compression (240MPa) is considerably larger under when compared with the obtained under traction (25MPa).

7.4.3.3 Traction combined with compression

In order to verify the effects of a bi-axial stress and the consequent strain state, a compression strain, combined with traction in the orthogonal direction, was enforced monotonically. Once again, the periodic boundary conditions were applied to this effect. The main objective was to verify if a reduction of the maximum compressive straight occurs. Furthermore, it was aimed to identify the patterns of damage that lead to rupture of the material in a biaxial state of compression and traction. The biaxial strain tensor employed was the following:

$$\boldsymbol{\varepsilon} = \begin{bmatrix} -10.0 & 0.0 \\ 0.0 & 2.0 \end{bmatrix} .10^{-3} \tag{7.26}$$

The damage pattern obtained is depicted in Figure 7.12. It is possible to observe, the development of cracks in the interface of the materials, combined with major cracks oriented in the diagonal direction.

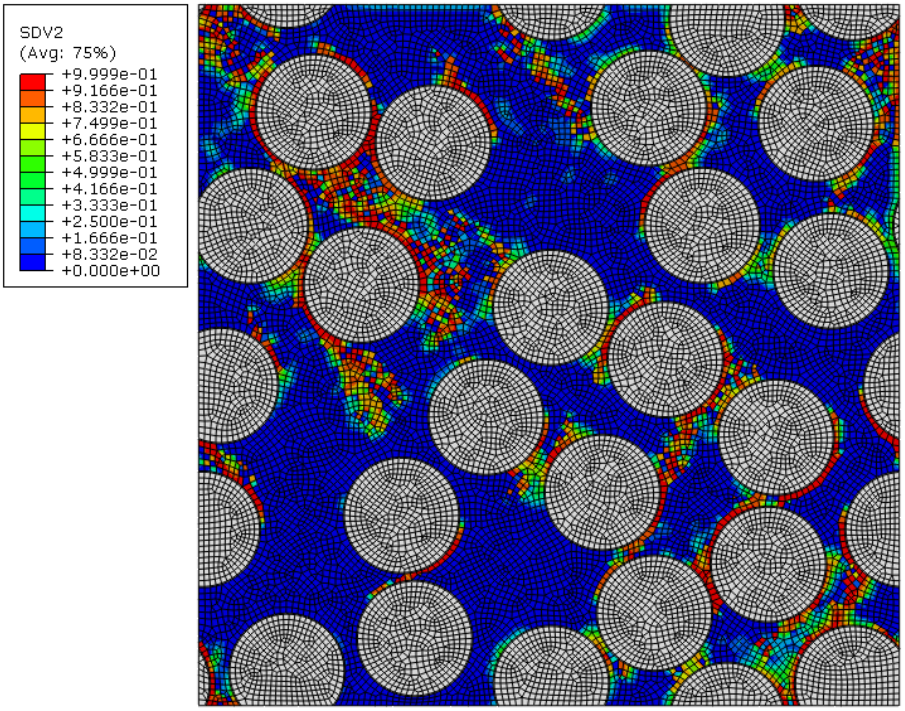

FIGURE 7.12: Damage pattern obtained under traction combined with compression.

The evolution of the compressive strength with the strain for different realizations is presented in Figure 7.13.

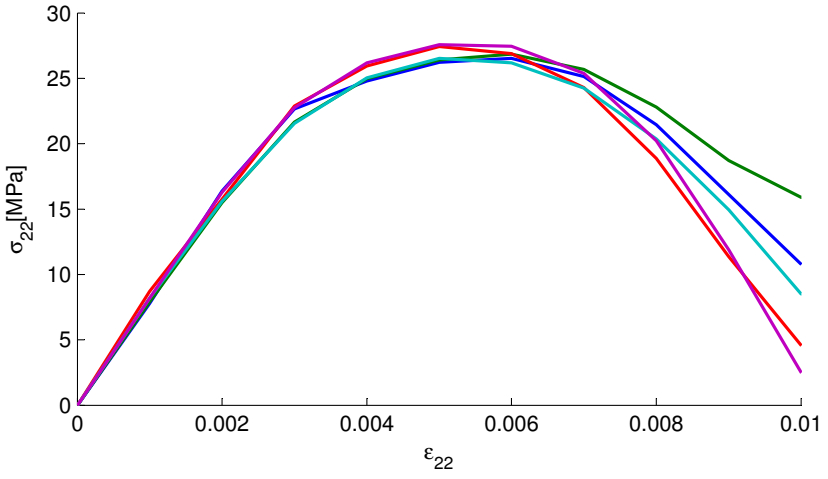

FIGURE 7.13: Stress strain curves under compression combined with traction, for 5 RVE realizations.

The maximum straight obtained was around 26 MPa, much smaller when compared with the one obtained for a simple compressive strain.

7.5 Remarks and conclusions

The presented framework demonstrated a fair capability to reproduce qualitatively the cracking patterns and consequent reduction of stiffness under a variety of loading scenarios. Notwithstanding, as already mentioned, a wide set of assumptions was considered in the presented numerical studies: the constitutive laws and parameters for the phases that have been designed for materials at structural scale, the use of the crack band model for regularization, the neglecting of size effects and the consideration of a simplified RVE microstructure.

Furthermore, according to some works [87], the principle of separation of scales sets limits for the homogenization of first order and, consequently, there are limitations for the method on handling large special gradients. Indeed, some of the conducted numerical experiments were rejected due to the formation of localization crack bands in the RVE borders. It was verified that as RVE size becomes larger the tendency for localization in the borders increase.

Our conclusions may be summarized as follows: the imposition of boundary conditions and the discretization (that considers elements and nodes aligned in the boundary) artificially creates perturbation in the stiffness and, as consequence increases the predisposition to the damage in the RVE borders. This predisposition could be more or less important depending on the conditions of the problem. For large RVEs, the distribution of the inclusions tends to be uniform due to size effects. Therefore, the density of the regions vulnerable to the damage tends to be uniform. Consequently, in large RVEs the perturbations introduced in the RVE borders "superimpose" their own cracking pattern over the relatively uniform pattern associated to the distribution of the inclusions within the RVE.

Therefore, the study of internal damage recommends the use of special boundary conditions and discretization scheme for either all RVE or only the boundaries, e.g. the employment of a special finite element. Furthermore, the use of high order homogenization schemes [95], [96], can more effectively resolve large special gradients and localization problems, despite being more complex.

Notwithstanding, the fair capability of the framework to reproduce qualitatively the cracking patterns, an experimental validation of the results is required. Preferably, this validation would consider a composite material with a simplistic structure, such as the one from this study and materials phases correctly characterized at the lower scale.

Chapter 8

Conclusions and Final Remarks

This thesis had two main objectives regarding the treatment of random close packed materials:

- improve both the generation and homogenization algorithms;
- analyze practical implications of the homogenization.

In this context, the contributions of this work are summarized in the following text.

Chapter 3
A comprehensive review of the homogenization principles is presented. That review, includes the concepts of: material scales, representative volume element (RVE), average quantities, Hill Mandel principle and kinematic equilibrium principle. Furthermore, classical boundary conditions commonly employed to fulfill those principles are described in their continuous and discretized forms.

A computational algorithm for the homogenization of three dimensional RVEs was developed as extension of an existing one[22] for 2D RVEs based on an academic FEM code [17]. To accomplish this task, a strategy of grouping the nodes (and correspondent degrees of freedom) in the faces, edges, vertex and interior of the RVE was employed. The objective was to rearrange the stiffness matrix regarding the dependencies between degrees of freedom prescribed by the boundary conditions.

Chapter 4
It is well known that practical computational homogenization requires, in general, the consideration of a large number of degrees of freedom and consequent computational costs. In this chapter, a combination of ideas for enhancing the performance of the homogenization algorithm described in the previous chapter was implemented.

The employment of periodic boundary conditions and other new arbitrary boundary conditions, in their discretized form, generally requires the prescription of relations between degrees of freedom. For large models, this operation is simplified with the development of a special purpose data structure, based on the concept of hash table, in order to store and access the components of the matrix of the coefficients. The use of hash tables allows saving the stiffness matrix in a compact format while simultaneously providing, fast access.

To achieve this, the standard concept of hash table, was adapted to fit the special characteristics of the matrix to save; this matrix is characterized by: a high density of non-null elements in the principal diagonals and by having the remaining elements distributed symmetrically and sparsely. The Generalized minimal residual method (GMRES) was employed as the iterative solution of unsymmetrical linear systems.

Furthermore, a strategy to impose periodic boundary conditions in non-periodic meshes was developed and implemented. The strategy involved the consideration of master and slave sets of nodes in opposite faces and edges, and the use of interpolation to establish the relation between degrees of freedom in those sets. Two types of interpolation are suggested. The first one uses linear interpolation with tree nodes for degrees located in the faces and two nodes for the edges. The second alternative considers, the usual iso-parametric transformation of coordinates for finite elements (transformation of real coordinates into standard element coordinates) and the same shape functions of FEM.

The performance of the overall homogenization algorithm was access through some numerical examples. Those numerical examples, comprehended two and three dimensional RVEs, with periodic and non-periodic meshes. Similar results and convergence rates were obtained for both periodic and non-periodic meshes. In all the examples, quadratic convergence rate was obtained.

Chapter 5

Regarding this chapter, a new algorithm for generating material models based on a random distribution of inclusions was presented. This problem was addressed by many studies, not only for generation of RVEs, but also a wide broad of subjects in Physics. Two important issues are the definition of 'randomness' and the existence of a tradeoff between 'randomness' and packing. To establish this algorithm, a new concept of designated *free volume* was developed and defined. The concept, leads to a new and clear parametrization of the random medium obtained by the distribution of disks or spheres of the same size. In this manner, the algorithm was constructed to guarantee that the 'randomness' obtained it is not 'hill-defined' or 'protocol dependent'.

The effectiveness of the algorithm was guaranteed by the use of appropriate domain decompositions and data structures, which allows determining free positions to add new inclusions directly, while avoiding the trial and error attempts, commonly employed in the classical random sequential addition (RSA) scheme.

To confirm the 'randomness' of the models generated with the algorithm, statistical procedures were employed and the results compared with other models existing in the literature.

Furthermore, a set of RVEs, generated using the presented algorithm, was subjected to computational homogenization under the framework described in Chapter 4. The homogenization procedure determined the effective elastic properties of each RVE. The computed elastic properties in different directions, confirms an expected isotropy.

It was also verified that, because the algorithm distributes the inclusions in a purely random manner, it is generally uncommon to achieve volume fractions higher than 55%. Therefore, considering the tradeoff between 'randomness' and 'parking', modifications to the algorithm are proposed to improve the obtained volume fractions up to 62%. Those modifications reduce the 'randomness' of the distributions in order to obtain higher packing. This is achieved when the *free volume* is modified by using one of the three proposed transformation functions.

Chapter 6

The homogenization framework was adapted to obtain elastic effective properties and tested for use within commercial software. Validation of the framework by comparison with analytical formulations was conducted. Then the elastic properties were obtained for a large set of RVEs. Using hypothesis tests to analyze that data, it was possible to conclude that certain homogenized variables, such as the elastic modulus, possess a very low probability of following a Gaussian distribution. In fact, a certain skew is apparent in the histograms obtained.

The influence of the relation between stiffness of the constituents of different RVEs was investigated using nondimensional quantities. Hence, a strong relation between the classical semi empirical Halpin-Tsai model and numerical homogenization was found. This relation confirmed a certain separation between contributions of geometry and properties of the phases to the overall elasticity. Furthermore, it should also be highlighted that the empirical reinforcement parameter ξ, from the Halpin-Tsai equations, is related with the geometry of the micro scale and can be determined using computational homogenization even if uncertain on the properties of the constituents exists.

Another important conclusion, also in agreement with the Halpin-Tsai model, is that when a large mismatch exists between the stiffness of the constituents, i.e. more than

1:10, the overall elasticity becomes relatively insensible to small variations in the elasticity of the phase with higher stiffness.

A parametric study on the influence of a thin layer involving the inclusions on the overall properties elastic properties was conducted. Again, nondimensional relations between the properties were considered in order to encompass a wide range of cases. It became apparent that overall homogenized Elastic modulus is highly sensible to the elasticity and thickness of the interface.

Finally, a comparative study on the dispersion of homogenized properties for three and two dimensional RVE models, randomly generated, was conducted. A relatively larger dispersion was obtained for the two dimensional models, while the larger average elasticity modulus was obtained for the three dimensional RVEs.

Chapter 7

The viability of computational homogenization to investigate the internal damage process of the materials was investigated. Therefore, a three phase material composed by circular inclusions embedded in a matrix, with an interface material between them, was considered. For the matrix, a common damage model was employed, while for the interface a cohesive model was considered. The constitutive model used for the phases is reviewed and implemented. Numerical tests were conducted to verify the implementation of the damage model and the mesh's independency from the results.

Finally, representative volume elements are subjected to different strain conditions: traction, compression and compression combined with traction. The patterns of damage and the stress strain curves were obtained for different RVEs. It was verified that some of the RVEs, produced localization cracks bands in the borders and were rejected because of that reason. This could be explained by limitations related with:

- the violation of the principle of separation of scales;
- the enforcement of the boundary conditions;
- the discretization of the model.

It was also verified that the tendency for localization in the borders, usually increases after a certain RVE size is achieved. The author proposes the hypothesis, that the perturbations introduced in the RVE borders become more important as the density of weaker regions tends to be more uniform as the RVE size increases.

Nevertheless, under a qualitative point of view, the framework demonstrated a fair capability to reproduce the cracking patterns and consequent reduction of stiffness.

8.1 Recommendations for future works

In this last section, some recommendations for future works are given.

The improved algorithm suggested for homogenization in Chapter 4 is highly susceptible of parallelization, which would allow the homogenization of more realistic RVE, in a more affordable computation time.

Regarding Chapter 5, the algorithm and concepts introduced allow a parameterization of the random medium. That parameterization can be easily converted in a 'prismatic' type of parameterization. For the effect, a random medium with n inclusions is produced by the algorithm by generating n random real numbers, then a set of numbers $x_1, x_2, .., x_n \in [0,1] \times [0,1] \times [0,1] \ldots [0,1] = [0,1]^n$ can describe the random distribution of inclusions. However, two similar distributions of inclusions can be generated by very different representations in the space $[0,1]^n$. If this limitation could be somehow removed, than important applications in the wide range of problems involving random close packing would be enabled. For instance, problems related with material optimization and optimal material distribution would be simplified, since the admissible domains would become simpler. Furthermore, this transformation would enable an alternative tool for the mathematical treatment of the close random packing subject.

The generalization of the algorithm to distributions of inclusions with different sizes can also be addressed considering a finite set of inclusion diameters, and using a free volume function for each of the diameters considered.

In Chapter 6, it was verified that the procedure for the homogenization of elastic properties in random RVEs produced statistical distributions of values that are not Gaussian. An important improvement to this process would be to identify the reason why this occurs. Perhaps, a more extended numerical investigation that could answer the following questions: what type of variable could fit better the data obtained? How are their parameters affected by the homogenization procedure? Which conditions and parameters could lead the variable to degenerate in to a Gaussian type? The author believes that these questions may bring improvements to the homogenization procedures.

Another point of interest was the agreement between the Halpin-Tsai model, and the computational homogenization. Then, an interesting idea would be to compare the Halpin-Tsai analytical formulation in materials based on inclusions with different shapes, spheres, for instance . This would allow to the computational homogenization to affirm itself as an alternative method able to compute the reinforcement parameter under those conditions.

In Chapter 7, the investigation of internal damage of the materials was addressed. It became evident the need for the development of homogenization boundary conditions that would allow to avoid the problem of damage localization in the borders of the RVEs. Also, a more robust framework that considers second order homogenization to address problems involving large deformation gradients is advised.

Bibliography

[1] X Sherry Liu, X Henry Zhang, Kiranjit K Sekhon, Mark F Adams, Donald J McMahon, John P Bilezikian, Elizabeth Shane, and X Edward Guo. High-resolution peripheral quantitative computed tomography can assess microstructural and mechanical properties of human distal tibial bone. *Journal of Bone and Mineral Research*, 25(4):746–756, 2010.

[2] Guang-Jie Feng, Zhuo-Ran Li, Rui-Hua Liu, and Shi-Cheng Feng. Effects of joining conditions on microstructure and mechanical properties of cf/al composites and tial alloy combustion synthesis joints. *Acta Metallurgica Sinica (English Letters)*, 28(4): 405–413, 2015.

[3] Jens Bauer, Stefan Hengsbach, Iwiza Tesari, Ruth Schwaiger, and Oliver Kraft. High-strength cellular ceramic composites with 3d microarchitecture. *Proceedings of the National Academy of Sciences*, 111(7):2453–2458, 2014.

[4] Lorna J Gibson. The hierarchical structure and mechanics of plant materials. *Journal of the Royal Society Interface*, page rsif20120341, 2012.

[5] JOHN D Eshelby. The determination of the elastic field of an ellipsoidal inclusion, and related problems. In *Proceedings of the Royal Society of London A: Mathematical, Physical and Engineering Sciences*, volume 241, pages 376–396. The Royal Society, 1957.

[6] R1 Hill. A self-consistent mechanics of composite materials. *Journal of the Mechanics and Physics of Solids*, 13(4):213–222, 1965.

[7] A Bensoussan, JL Lions, and G Papanicolaou. Asymptotic analysis for periodic structures, north-holland, amsterdam, 1978.

[8] E Sanchez-Palencia. Non-homogeneous media and vibration theory, lecture notes in physics, vol. 127, springer, berlin, 1980.

[9] KonstantinZ. Markov. Elementary micromechanics of heterogeneous media. In Konstantin Markov and Luigi Preziosi, editors, *Heterogeneous Media*, Modeling

and Simulation in Science, Engineering and Technology, pages 1–162. Birkhäuser Boston, 2000. ISBN 978-1-4612-7098-0. doi: 10.1007/978-1-4612-1332-1_1.

[10] HelmutJ. Böhm. A short introduction to continuum micromechanics. In HelmutJ. Böhm, editor, *Mechanics of Microstructured Materials*, volume 464 of *International Centre for Mechanical Sciences*, pages 1–40. Springer Vienna, 2004. ISBN 978-3-211-24154-7. doi: 10.1007/978-3-7091-2776-6_1.

[11] C Miehe and A Koch. Computational micro-to-macro transitions of discretized microstructures undergoing small strains. *Archive of Applied Mechanics*, 72(4-5): 300–317, 2002.

[12] K Terada, I Saiki, K Matsui, and Yt Yamakawa. Two-scale kinematics and linearization for simultaneous two-scale analysis of periodic heterogeneous solids at finite strain. *Computer Methods in Applied Mechanics and Engineering*, 192(31): 3531–3563, 2003.

[13] D. Trias, J. Costa, J.A. Mayugo, and J.E. Hurtado. Random models versus periodic models for fibre reinforced composites. *Computational Materials Science*, 38(2):316 – 324, 2006.

[14] O. Van der Sluis, PJG Schreurs, WAM Brekelmans, and HEH Meijer. Overall behaviour of heterogeneous elastoviscoplastic materials: effect of microstructural modelling. *Mechanics of Materials*, 32(8):449–462, 2000.

[15] S. Torquato, T.M. Truskett, and P.G. Debenedetti. Is random close packing of spheres well defined? *Physical Review Letters*, 84(10):2064–2067, 2000.

[16] J. Bonet and R.D. Wood. *Nonlinear continuum mechanics for finite element analysis*. Cambridge Univ Pr, 1997.

[17] D.Peric DRJ Owen, E.Neto. *Computational Methods for Plasticity*. Wiley, 2008.

[18] E. Hinton and DRJ Owen. *An introduction to finite element computations*. Pineridge Press, Swansea, Wales, 1979.

[19] T. Belytschko, WK Liu, and B. Moran. *Nonlinear finite elements for continua and structures*, volume 36. Wiley, 2000.

[20] K.J. Bathe. Finite element procedures. *Englewood Cliffs, New Jersey*, 1996.

[21] EA de Souza Neto and RA Feijóo. Variational foundations of multi-scale constitutive models of solid: small and large strain kinematical formulation. *LNCC Research & Development Report*, 16, 2006.

[22] F. Reis. Multi-scale constitutive modelling. *PHD seminar project FEUP DEMec*, 2011.

[23] FE^2 multiscale approach for modelling the elastoviscoplastic behaviour of long fibre SiC/Ti composite materials. *Computer Methods in Applied Mechanics and Engineering*, 183(3–4):309 – 330, 2000. ISSN 0045-7825.

[24] Kazumi Matsui, Kenjiro Terada, and Kohei Yuge. Two-scale finite element analysis of heterogeneous solids with periodic microstructures. *Computers & structures*, 82 (7):593–606, 2004.

[25] Gaëtan Compere, Jean-François Remacle, Johan Jansson, and Johan Hoffman. A mesh adaptation framework for dealing with large deforming meshes. *International journal for numerical methods in engineering*, 82(7):843–867, 2010.

[26] Pascal Frey. YAMS A fully Automatic Adaptive Isotropic Surface Remeshing Procedure. Technical Report RT-0252, November 2001.

[27] Zheng Yuan and Jacob Fish. Toward realization of computational homogenization in practice. *International Journal for Numerical Methods in Engineering*, 73(3): 361–380, 2008. ISSN 1097-0207.

[28] J.M. Tyrus, M. Gosz, and E. DeSantiago. A local finite element implementation for imposing periodic boundary conditions on composite micromechanical models. *International Journal of Solids and Structures*, 44(9):2972 – 2989, 2007. ISSN 0020-7683.

[29] V.-D. Nguyen, E. Béchet, C. Geuzaine, and L. Noels. Imposing periodic boundary condition on arbitrary meshes by polynomial interpolation. *Computational Materials Science*, 55(0):390 – 406, 2012. ISSN 0927-0256.

[30] F.J.P. Reis and F.M. Andrade Pires. A mortar based approach for the enforcement of periodic boundary conditions on arbitrarily generated meshes. *Computer Methods in Applied Mechanics and Engineering*, 274(0):168 – 191, 2014. ISSN 0045-7825.

[31] Der-Tsai Lee and Bruce J Schachter. Two algorithms for constructing a delaunay triangulation. *International Journal of Computer & Information Sciences*, 9(3): 219–242, 1980.

[32] IM Gitman, H. Askes, and LJ Sluys. Representative volume: Existence and size determination. *Engineering fracture mechanics*, 74(16):2518–2534, 2007.

[33] Thomas H Cormen, Charles E Leiserson, Ronald L Rivest, Clifford Stein, et al. *Introduction to algorithms*, volume 2. MIT press Cambridge, 2001.

[34] Jean-Paul Tremblay and Paul G. Sorenson. *An Introduction to Data Structures with Applications (2Nd Ed.)*. McGraw-Hill, Inc., New York, NY, USA, 1984.

[35] George T Heineman, Gary Pollice, and Stanley Selkow. *Algorithms in a Nutshell*. " O'Reilly Media, Inc.", 2008.

[36] Gene H Golub and Charles F Van Loan. *Matrix computations*, volume 3. JHU Press, 2012.

[37] Y. Saad and M. Schultz. Gmres: A generalized minimal residual algorithm for solving nonsymmetric linear systems. *SIAM Journal on Scientific and Statistical Computing*, 7(3):856–869, 1986.

[38] Kenjiro Terada, Muneo Hori, Takashi Kyoya, and Noboru Kikuchi. Simulation of the multi-scale convergence in computational homogenization approaches. *International Journal of Solids and Structures*, 37(16):2285 – 2311, 2000.

[39] T. Kanit, S. Forest, I. Galliet, V. Mounoury, and D. Jeulin. Determination of the size of the representative volume element for random composites: statistical and numerical approach. *International Journal of Solids and Structures*, 40(13–14):3647 – 3679, 2003. ISSN 0020-7683.

[40] Toufik Kanit, Franck N'Guyen, Samuel Forest, Dominique Jeulin, Matt Reed, and Scott Singleton. Apparent and effective physical properties of heterogeneous materials: Representativity of samples of two materials from food industry. *Computer Methods in Applied Mechanics and Engineering*, 195(33–36):3960 – 3982, 2006. ISSN 0045-7825.

[41] X. Teng. Numerical prediction of slant fracture with continuum damage mechanics. *Engineering Fracture Mechanics, New Jersey*, 2008.

[42] TI Zohdi. Computational optimization of the vortex manufacturing of advanced materials. *Computer methods in applied mechanics and engineering*, 190(46):6231–6256, 2001.

[43] D. Trias, J. Costa, JA Mayugo, and JE Hurtado. Random models versus periodic models for fibre reinforced composites. *Computational materials science*, 38(2): 316–324, 2006.

[44] A Wongsto and S Li. Micromechanical fe analysis of ud fibre-reinforced composites with fibres distributed at random over the transverse cross-section. *Composites Part A: Applied Science and Manufacturing*, 36(9):1246–1266, 2005.

[45] S. Häfner, S. Eckardt, T. Luther, and C. Könke. Mesoscale modeling of concrete: Geometry and numerics. *Computers & structures*, 84(7):450–461, 2006.

[46] AR Melro, PP Camanho, and ST Pinho. Generation of random distribution of fibres in long-fibre reinforced composites. *Composites Science and Technology*, 68 (9):2092–2102, 2008.

[47] YT Feng, K. Han, and DRJ Owen. Filling domains with disks: an advancing front approach. *International Journal for Numerical Methods in Engineering*, 56 (5):699–713, 2002.

[48] S. Torquato and F.H. Stillinger. Jammed hard-particle packings: From kepler to bernal and beyond. *Reviews of Modern Physics*, 82(3):2633, 2010.

[49] J.D Bernal. A geometrical approach to the structure of liquids. *Nature*, (183): 141–147, 1959.

[50] VA Buryachenko, NJ Pagano, RY Kim, and JE Spowart. Quantitative description and numerical simulation of random microstructures of composites and their effective elastic moduli. *International journal of solids and structures*, 40(1):47–72, 2003.

[51] D.W. Cooper. Random-sequential-packing simulations in three dimensions for spheres. *Physical Review A*, 38(1):522, 1988.

[52] C.H. Bennett. Serially deposited amorphous aggregates of hard spheres. *Journal of applied physics*, 43(6):2727–2734, 1972.

[53] DS Boudreaux and JM Gregor. Structure simulation of transition metal-metalloid glasss. *Journal of Applied Physics*, 48(1):152–158, 1977.

[54] C. Wellmann, C. Lillie, and P. Wriggers. Homogenization of granular material modeled by a three-dimensional discrete element method. *Computers and Geotechnics*, 35(3):394–405, 2008.

[55] WS Jodrey and EM Tory. Computer simulation of close random packing of equal spheres. *Physical review A*, 32(4):2347, 1985.

[56] K. Han, YT Feng, and DRJ Owen. Sphere packing with a geometric based compression algorithm. *Powder Technology*, 155(1):33–41, 2005.

[57] A.A. Gusev, P.J. Hine, and I.M. Ward. Fiber packing and elastic properties of a transversely random unidirectional glass/epoxy composite. *Composites science and Technology*, 60(4):535–541, 2000.

[58] K.L. Scrivener, A.K. Crumbie, and P. Laugesen. The interfacial transition zone (itz) between cement paste and aggregate in concrete. *Interface Science*, 12(4): 411–421, 2004.

[59] D. Trias. Determination of the critical size of a statistical representative volume element (srve) for carbon reinforced polymers. *Acta Materialia*, 54(13):3471 – 3484, 2006.

[60] W.J. Drugan and J.R. Willis. A micromechanics-based nonlocal constitutive equation and estimates of representative volume element size for elastic composites. *Journal of the Mechanics and Physics of Solids*, 44(4):497 – 524, 1996. ISSN 0022-5096.

[61] Martin Ostoja-Starzewski. Scale effects in materials with random distributions of needles and cracks. *Mechanics of Materials*, 31(12):883 – 893, 1999. ISSN 0167-6636.

[62] Z.-Y. Ren and Q.-S. Zheng. Effects of grain sizes, shapes, and distribution on minimum sizes of representative volume elements of cubic polycrystals. *Mechanics of Materials*, 36(12):1217 – 1229, 2004.

[63] Z.-Y Ren and Q.-S Zheng. A quantitative study of minimum sizes of representative volume elements of cubic polycrystals—numerical experiments. *Journal of the Mechanics and Physics of Solids*, 50(4):881 – 893, 2002. ISSN 0022-5096.

[64] J. Zeman and M.Sejnoha. Numerical evaluation of effective elastic properties of graphite fiber tow impregnated by polymer matrix. *Journal of the Mechanics and Physics of Solids*, 49(1):69 – 90, 2001. ISSN 0022-5096.

[65] Andrei A. Gusev. Representative volume element size for elastic composites: A numerical study. *Journal of the Mechanics and Physics of Solids*, 45(9):1449 – 1459, 1997. ISSN 0022-5096.

[66] Christian Miehe. Computational micro-to-macro transitions for discretized microstructures of heterogeneous materials at finite strains based on the minimization of averaged incremental energy. *Computer Methods in Applied Mechanics and Engineering*, 192(5):559–591, 2003.

[67] B Widom. Random sequential addition of hard spheres to a volume. *The Journal of Chemical Physics*, 44:3888, 1966.

[68] PD Soden, MJ Hinton, and AS Kaddour. Lamina properties, lay-up configurations and loading conditions for a range of fibre-reinforced composite laminates. *Composites Science and Technology*, 58(7):1011–1022, 1998.

[69] Zvi Hashin and S Shtrikman. A variational approach to the theory of the elastic behaviour of multiphase materials. *Journal of the Mechanics and Physics of Solids*, 11(2):127–140, 1963.

[70] JC Halpin and JL Kardos. The halpin-tsai equations: a review. *Polymer Engineering & Science*, 16(5):344–352, 1976.

[71] Jean Dickinson Gibbons and Subhabrata Chakraborti. *Nonparametric statistical inference*, volume 168. CRC press, 2003.

[72] Nicolas Moës, John Dolbow, and Ted Belytschko. A finite element method for crack growth without remeshing. *International Journal for Numerical Methods in Engineering*, 46(1):131–150, 1999. ISSN 1097-0207.

[73] DA Cendón, JC Gálvez, M Elices, and J Planas. Modelling the fracture of concrete under mixed loading. *International Journal of Fracture*, 103(3):293–310, 2000.

[74] R. H. J. Peerlings, W. A. M. Brekelmans, R. de Borst, and M. G. D. Geers. Gradient-enhanced damage modelling of high-cycle fatigue. *International Journal for Numerical Methods in Engineering*, 49(12):1547–1569, 2000. ISSN 1097-0207.

[75] Peter Grassl and Milan Jirásek. Plastic model with non-local damage applied to concrete. *International Journal for Numerical and Analytical Methods in Geomechanics*, 30(1):71–90, 2006. ISSN 1096-9853.

[76] Zdeněk P. Bažant. Size effect. *International Journal of Solids and Structures*, 37 (1–2):69 – 80, 2000. ISSN 0020-7683.

[77] LM Kachanov. Time of the rupture process under creep conditions. *Isv. Akad. Nauk. SSR. Otd Tekh. Nauk*, 8:26–31, 1958.

[78] JL Chaboche. Description thermodynamique et phénoménologique de la viscoplasticité cyclique avec endommagement (publication no. 1978-3). 92320 chatillon. *France: Office National dEtudes et de Recherches Aérospatiales*, 1978.

[79] Jean Lemaitre. A continuous damage mechanics model for ductile fracture. *Journal of Engineering Materials and Technology*, 107(1):83–89, 1985.

[80] Alix Cauvin and Rene B. Testa. Damage mechanics : basic variables in continuum theories. *International Journal of Solids and Structures*, 36(5):747 – 761, 1999. ISSN 0020-7683.

[81] Pierre Ladeveze. On an anisotropic damage theory. *Proc. CNRS Int. Coll*, 351: 355–363, 1983.

[82] P Ladeveze and J Lemaitre. Damage effective stress in quasi unilateral conditions. In *16th International congress of theoretical and applied mechanics, Lyngby, Denmark*, 1984.

[83] Jean Lemaitre, Rodrigue Desmorat, and Maxime Sauzay. Anisotropic damage law of evolution. *European Journal of Mechanics - A/Solids*, 19(2):187 – 208, 2000. ISSN 0997-7538.

[84] Zdeněk P Bažant and Byung H Oh. Crack band theory for fracture of concrete. *Matériaux et construction*, 16(3):155–177, 1983.

[85] Zdenek P Bazant. Nonlocal damage theory based on micromechanics of crack interactions. *Journal of engineering mechanics*, 120(3):593–617, 1994.

[86] RHJ PEERLINGS R DE and JHP DE VREE. Gradient enhanced damage for quasi-brittle materials. *International Journal for numerical methods in engineering*, 39: 3391–3403, 1996.

[87] M.G.D. Geers, V.G. Kouznetsova, and W.A.M. Brekelmans. Multi-scale computational homogenization: Trends and challenges. *Journal of Computational and Applied Mathematics*, 234(7):2175 – 2182, 2010. ISSN 0377-0427. Fourth International Conference on Advanced {COmputational} Methods in {ENgineering} (ACOMEN 2008).

[88] M. Jirásek and S. Marfia. Non-local damage model based on displacement averaging. *International Journal for Numerical Methods in Engineering*, 63(1):77–102, 2005. ISSN 1097-0207.

[89] FKF Radtke, A Simone, M Stroeven, LJ Sluys, E Schlangen, and G De Schutter. Multiscale framework to model fiber reinforced cementitious composite and study its microstructure. In *Proc. Rilem Symp., CONMOD'08*, pages 551–558, 2008.

[90] Carlos González and Javier LLorca. Mechanical behavior of unidirectional fiber-reinforced polymers under transverse compression: Microscopic mechanisms and modeling. *Composites Science and Technology*, 67(13):2795 – 2806, 2007. ISSN 0266-3538.

[91] D Aragonés. *Fracture micromechanisms in C/epoxy composites under transverse compression*. PhD thesis, Master thesis, Universidad Politécnica de Madrid, 2007.

[92] User ABAQUS. Theory manual, 2002.

[93] Ted Diehl. Modeling surface-bonded structures with abaqus cohesive elements: beam-type solutions. In *ABAQUS User's Conference*, 2005.

[94] Pedro P Camanho and Carlos G Dávila. Mixed-mode decohesion finite elements for the simulation of delamination in composite materials. *NASA-Technical paper*, 211737(1):33, 2002.

[95] P. Ponte Castañeda and E. Tiberio. A second-order homogenization method in finite elasticity and applications to black-filled elastomers. *Journal of the Mechanics and Physics of Solids*, 48(6–7):1389 – 1411, 2000. ISSN 0022-5096.

[96] V.G. Kouznetsova, M.G.D. Geers, and W.A.M. Brekelmans. Multi-scale second-order computational homogenization of multi-phase materials: a nested finite element solution strategy. *Computer Methods in Applied Mechanics and Engineering*, 193(48–51):5525 – 5550, 2004. ISSN 0045-7825. Advances in Computational Plasticity.